Spring 2016

Experimental And Theoretical Analyses Of The Structural, Electronic And Magnetic Properties Of Novel Inverted Core-Shell a-CR2O3@a-Mxcr2-Xo3-Y (M=Co, Ni, Mn, Fe) Nanoparticles

Mohammad Delower Hossain

EXPERIMENTAL AND THEORETICAL ANALYSES OF THE STRUCTURAL, ELECTRONIC AND MAGNETIC PROPERTIES OF NOVEL INVERTED CORE-SHELL α-Cr_2O_3@α-$M_xCr_{2-x}O_{3-y}$ (M=Co, Ni, Mn, Fe) NANOPARTICLES

A Masters Thesis

Presented to

The Graduate College of

Missouri State University

In Partial Fulfillment

Of the Requirements for the Degree of Master of Science, Materials Science

By

Mohammad Delower Hossain

May 2016

EXPERIMENTAL AND THEORETICAL ANALYSES OF THE STRUCTURAL, ELECTRONIC AND MAGNETIC PROPERTIES OF NOVEL INVERTED CORE-SHELL α-Cr_2O_3@α-$M_xCr_{2-x}O_{3-y}$ (M=Co, Ni, Mn, Fe) NANOPARTICLES

Physics Astronomy and Materials Science

Missouri State University, May 2016

Master of Science

Mohammad Delower Hossain

ABSTRACT

I used hydrothermal nano-phase epitaxy technique to synthesize well-ordered α-Cr_2O_3@α-$M_xCr_{2-x}O_3$ (M = Co, Ni, Mn, Fe) inverted core-shell nanoparticles (NPs). This resulted in the formation of novel α-$M_xCr_{2-x}O_3$ shells having ferromagnetic/ferrimagnetic (FM/FiM) spin ordering and an antiferromagnetic (AFM) α-Cr_2O_3 core structure. The combined results from Xray diffraction (XRD) and high resolution transmission electron microscoy (HRTEM) provide evidence of the presence of the corundum phase both in the shell and in the core regions. HRTEM results also show a sharp interface exhibiting epitaxial atomic registry of shell atoms over highly ordered core atoms whereas TEM-Energy dispersive spectroscopy analyses show that the M atoms reside in the shell regions. The Xray photoelectron spectroscopy (XPS) analyses of the NPs indicate the M transition metal is in +2 oxidation state. Magnetic measurements show well-developed hysteresis loops: the field cooled hysteresis loops reveal horizontal shifts in the applied field axis and vertical shifts in the magnetization axis, relative to the zero-field cooled hysteresis loops. This provides direct evidence for the exchange bias effect between the AFM α-Cr_2O_3 core and the FM/FiM α-$M_xCr_{2-x}O_3$ shell. My first principles density functional theory calculations shows that the incorporation of Ni^{2+} in α-Cr_2O_3 results in localized FM ordering in the structure.

KEYWORDS: hydrothermal, epitaxy, nanoparticle, transition metal, ferromagnetic, antiferromagnetic, hysteresis, exchange bias.

This abstract is approved as to form and content

_____

Robert A Mayanovic, PhD
Chairperson, Advisory Committee
Missouri State University

EXPERIMENTAL AND THEORETICAL ANALYSES OF STRUCTURAL, ELECTRONIC AND MAGNETIC PROPERTIES OF NOVEL INVERTED CORE-SHELL α-Cr_2O_3@α-$M_xCr_{2-x}O_{3-y}$ (M=Co, Ni, Mn, Fe) NANOPARTICLES

By

Mohammad Delower Hossain

A Masters Thesis
Submitted to the Graduate College
Of Missouri State University
In Partial Fulfillment of the Requirements
For the Degree of Master of Science, Materials Science

May 2016

Approved:

_____
Robert A. Mayanovic, PhD

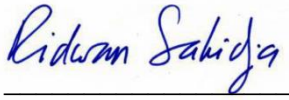

_____
Ridwan Sakidja, PhD

_____
Fei Wang, PhD

_____
Julie Masterson, PhD: Dean, Graduate College

ACKNOWLEDGEMENTS

I am grateful to my research advisor Dr. Robert A. Mayanovic for guiding me throughout the research also I am thankful to my research co-advisor Dr. Ridwan Sakidja for constant help and support. I thank Dr. Kartik Ghosh –faculty PAMS, Dr. Sonal Dey, former postdoc and Rezwanur Rahman, Sean Anderson former graduate student in the PAMS Department, for their help and support regarding different instrument and software.

I thank Rishi Patel and Aleksander Jankovic at Jordan Valley Innovation Center (JVIC) for assistance with XPS measurements, and Dr. Mourad Benamara at the University of Arkansas Institute for Nanoscience and Engineering, for assistance with TEM measurements. I am thankful to PAMS Department and Graduate College for all the economic support.

TABLE OF CONTENTS

LIST OF TABLES

LIST OF FIGURES

OVERVIEW

The last several decades magnetic nanoparticles (NPs) found lots of interest from the research community due to their application prospective in wide area of science and technology. Availability of many different synthesis process such as sol-gel, co-precipitation and hydrothermal process of nanoparticle synthesis provide the opportunity to grow wide variety of NPs with different size and shapes. Combination of the different synthesis process including the nanoscale dimension of the particles imparts interesting optical, electronic and magnetic properties in the NPs which finds it application in magnetic random access memory, spintronic devices, quantum computing[1], biomedicine[2,3]. Finite size effect for magnetic NPs often develop superparamagnetism (SP) which limits the applicability of the NPs in the recording media or drug delivery system. Thus consideration from the application point of view developing ferromagnetic (FM), antiferromagnetic (AFM) or both property in the NPs provides greater flexibility in operation. Also it is highly desirable to extract multifunctionality from single materials which may show combination of desirable magnetic and electronic properties. One technique to develop multifunctionality in the NPs is to grow core shell (CS) structure in the NPs which may have different property with respect to core and shell. This composite materials may develop unique property which is a combination of the property in the core and shell of the NPs. This core-shell structure may also confer higher degree of tunability depending on the operation condition such as temperature and environmental aspect of operation, including but not limited to particle size and shape, core and shell size,

roughness of the interface etc. may largely impact the NPs performance in the desired application system.

An attractive composition in the CS structure is the formation of FM core and AFM shell or vice versa. This types of system develops a unique interaction known as exchange interaction at the interface which termed as the exchange biasing (EB) effect between the core and shell. This EB effect first discovered by Meiklejohn and Bean in the Co particles, when they observed the field cooled (FC) hysteresis loops shifted with respect to the zero field cooled (ZFC) hysteresis loops[4,5]. This phenomenon described by the exchange interaction of the spins at the interface between the AFM CoO shell and FM Co core. Although most of the exchange biasing system development has been done on the thin films as it provides greater amount of control of the films and interface characteristics, including wider range of combination that forms the exchange coupled arrangement and above all its suitability for probable application in the devices. In recent times the development of variety of techniques to produce nanoparticles and lithographic technique to develop nanostructures shed light on the exchange bias system at nanoscale. In addition exchange interaction at FM-AFM interface may induce permanent magnetic characteristics in the nanostructures by increasing the coercivity, eliminating the superparamagnetic limitation due to the size effect and above all proximity effect may help to build room temperature FM/AFM characteristics.

The exchange bias phenomenology may reveal in the coupled FM-AFM system by horizontal loop shift in the field axis, increase in coercivity, vertical loop shift in the magnetization axis of FC hysteresis curve with respect to the ZFC curve. Another well-known characteristics is the development of unidirectional anisotropy compared to the

uniaxial anisotropy observed in the FM materials. Figure 0.1 (a) and (b) shows effect of the exchange biasing effect in the hysteresis loop and 0.1 (c) shows the spin arrangement in the FM and AFM region in the different temperature range. During the field cooling procedure at $T<T_N$ AFM spins at the FM-AFM interface align themselves parallel to the FM spin when temperature reaches below T_N and a coupled state reached between the interface AFM and FM spins.

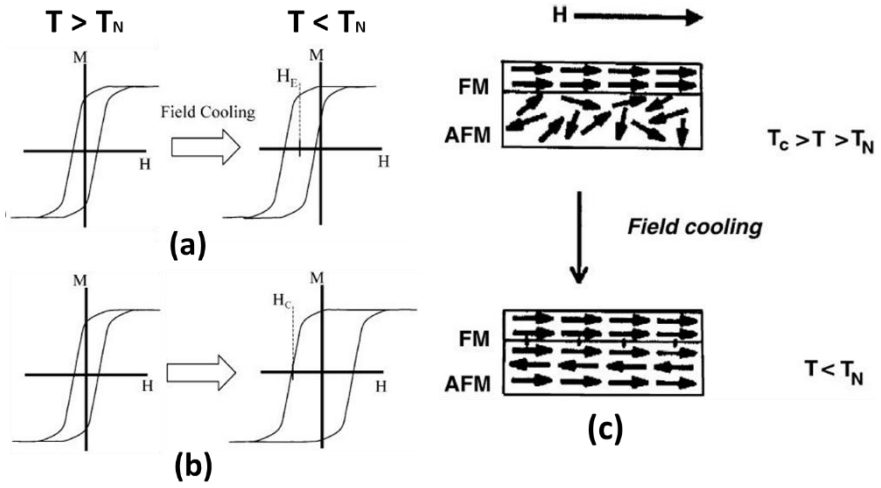

Figure 0.1: Effect of the FM-AFM exchange coupling or the exchange biasing effect (a) horizontal loop shift (b) enhancement of coercivity and (c) spin arrangement in the FM and AFM region in different temperature.[6]

This coupling effect at the interface impose an additional force on the FM spins which has to be overcomed by the external field. Depending on the anisotropy strength of AFM spins two different situation may arise (i) if AFM anisotropy is large then the horizontal shift of the hysteresis loops observed (ii) for small anisotropy value, enhancement of the coercivity will result. Many of the thin films and NPs system may show both of them due to the presence of defect in the structure which ultimately affect the anisotropy strength of the materials. The mechanism of this horizontal loop shift for

the coupled state of the spin at the interface between the FM-AFM regions explained in the Fig. 0.2. At the interface after the field cooling both the FM and AFM spins align themselves parallel to each other [Fig. 0.2(a)]. Reversing the magnetic field to generate the whole hysteresis loop will force the FM spins to rotate to follow the field direction. In case of large anisotropy value of the AFM spins, the AFM spins will not follow the field direction and this will exert some extra force/torque on the interface coupled spins in the FM region, trying to keep the spins in their original direction [Fig. 0.2 (b)].

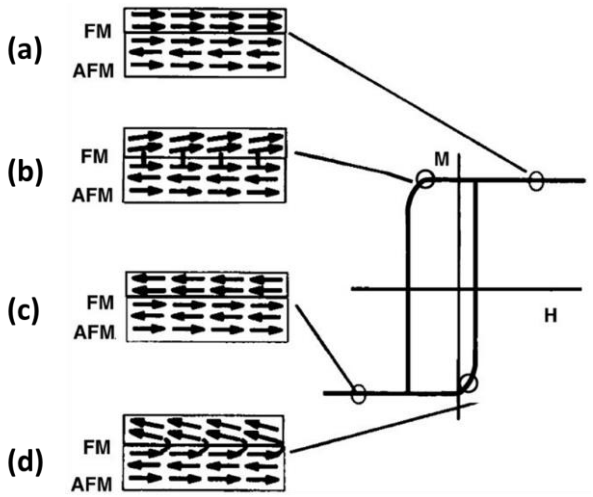

Figure 0.2: Spin arrangement at the interface between FM-AFM region at different stage of the FC hysteresis loop[6].

This will required additional field in the negative field axis to move those pinned FM spin in the other direction. But when the field is reversed back to positive value it requires less force to align the FM spins as this direction of alignment energetically more favorable because the AFM spins exert torque in the same direction of applied magnetic field. The net result is the shift of the hysteresis loops in the FC condition. For small anisotropy value of the AFM spins enhancement of coercivity of the sample observed due

to the rotation of the AFM spins in the field direction. Increasing the temperature to a value close to the T_N of the sample will transform the observed sample from the large anisotropy value of the AFM spin to low anisotropy of AFM spins which will follow the second model described above. The amount of the coupling also depends on the particle size, shell thickness, training effect, temperature and nature of the interface coupling etc. As for the thin film system exchange biasing (EB) effect depends on the thickness of the FM and AFM layers for the NPs, it is the core size and thickness of the shell in typical CS NPs determines the extend of the EB field H_{eb}. Dependence of H_{eb} on the particle size reported by Gangopadhyay et al.[7,8] in their study of the oxide passivated Co particles, also similar kind of phenomenon observed for the oxide passivated Fe particles with diameters of 6-15 nm[9,10] and Fe@ γFe_2O_3[9] particles. For typical CS NPs where the core is FM and shell is AFM there are certain dependence of H_{eb} on the shell thickness. The AFM shell should maintain a certain minimum thickness for observing EB effect in the sample, the anisotropy energy per unit area in the AFM shell should be greater than the interfacial exchange energy so that the EB effect can take place. Thus H_{eb} should increase with shell thickness but after a certain critical thickness H_{eb} will be independent of the thickness of the shell. Both the H_{eb} and the coercive field H_c for the CS NPs and thin films system depends on the temperature. As with increasing temperature the AFM or FIM magnetic order degrades, thus the EB should be vanished at the ordering temperature (T_N) of the sample. Although for most experimental system EB disappear at the temperature below the T_N which is known as the blocking temperature T_B.

In general EB effect in NPs can be divided into the category of NPs embedded in AFM matrices and typical CS NPs. In the CS structured NPs formation majority of this

system has been synthesized based on the principle of partial oxidation of the nanoparticles which will result a distinct phase on top of the core, in addition chemically assisted co-precipitation method dominates this types distinct phase formation in the NPs. This new phase formation results in two different magnetic structure in the NPs the core which is FM and oxidized shell which is AFM and CS region also different structurally. Some combinations of CS structure formation has been tried by researchers throughout several decades are Co@CoO[4], NiCo@NiCoO[11], Co@CoN[12], Fe_3O_4@FeO[13,14], Fe@Fe_2O_3[15], Ni@NiO[16,17], CrO_2@Cr_2O_3[18] etc. Most of these CS NPs growing technique use the chemical surface treatment to grow the CS structure. One of the major limitation is the number of different combination is restricted by the same types of transition metals and their corresponding oxides system are required. Thus different combination of CS is not possible and also due to a complete different phase formation highly disordered interface results in this chemical assisted process including the danger of higher oxidation may produce a small size core and ultimately the CS NPs will be paramagnetic.

In my thesis I have developed a novel hydrothermal nanophase epitaxy (HNE) method to grow CS nanoparticles. This HNE method provides wide range of flexibility to grow different CS structure which is not limited by the specific choice of elements, in addition compared to the other CS structure this HNE method produce highly ordered single phase structure which gives very smooth interface between the core and shell. This smooth interface may produce greater degree of coupling between the two distinct magnetic regions which will result unique magnetic properties from this CS NPs. Also this HNE method eliminate limitation of typical CS NPs techniques which produce a FM core and AFM shell. This novel method gives the opportunity to produce an inverted CS

NPs system by breaking the concept of typical CS structure by producing an AFM core and FM/FIM shell which may show greater degree of FM/FIM characteristics along with AFM property of the original core phase. My method will be helpful for inducing multifunctionality in the NPs with greater degree of tunability. For my thesis I worked on the antiferromagnetic Cr_2O_3 system. Corundum-phased Cr_2O_3 (α-Cr_2O_3) is a wide band gap p-type semiconductor[19] with a band gap of 3.2 eV.[20–22] This highly important transition metal oxide has variety of applications in electronic and optoelectronic devices, catalysis[23], transparent conducting oxides[24], sensors[25], and for coating materials[26,27]. In addition, utilizing the antiferromagnetic property of α-Cr_2O_3 provides the opportunity for synthesis of nanostructured magnetic thin films and magnetic nanoparticles with potential applications in magnetic random access memory and spintronic devices. The working principle of spintronic devices is based on using both the charge and spin degrees of freedom of electrons, which requires multi-functionality from a single material. Success has been attained in developing ferromagnetism in semiconductor materials to produce dilute magnetic semiconductors by doping with transition and rare earth metal into various metal oxides such as SnO_2[28], ZnO[29], ZnS[30], CeO_2[11]. The underlying mechanism of inducing magnetic properties, such as ferromagnetism, in these non-magnetic metal oxides upon introduction of magnetic-moment-bearing dopant, has been attributed to various mechanisms, such as the oxygen vacancy formation, cation vacancies, double exchange, super exchange, and bound magnetic polarons. Theoretical calculations have been made in order to design-in the optical and magnetic properties of different oxide materials system by considering doping with various impurities[31–36]. Maldonado et. el.[34] in their theoretical study of Ca doped α-Cr_2O_3 shows the modification of the electronic

band gap structure and ferromagnetic behavior of the doped system; Wang et. el.[33] found that first-row transition metal doped TiO_2 system exhibits extensive modification of the band gaps and stable structure formation of the doped structure; ab initio calculations made by Li et. el[31] showed band gap reduction of early transition metals (Sc, Y, La, Zr, Hf, V, Nb, and Ta) doped TiO_2 systems. Ab initio calculations have also been made on non-metallic N,F co-substitution[37] in the host α-Cr_2O_3 which showed modification of the magnetic properties of the material.

Using my developed HNE method I have successfully synthesized transition metal doped well-ordered inverted CS α-Cr_2O_3@α-$M_xCr_{2-x}O_{3-y}$ (M=Co, Ni, Mn, Fe) NPs. In addition to experimental characterization of the NPs this thesis also includes density functional theory (DFT) based theoretical calculation to find out the origin of FM/FIM characteristics of this CS α-Cr_2O_3@α-$M_xCr_{2-x}O_{3-y}$ NPs. This theoretical calculation will also shed lights on the types of interaction between the doped elements and the matrix Cr atoms and based on this I propose a tentative exchange mechanism in the transition metal doped Cr_2O_3 system.

In this thesis, Chapter One will describe the results from α-Cr_2O_3/α-$Co_{0.43}Cr_{1.57}O_{2.9}$ core-shell NPs, Chapter Two will describe both experimental and theoretical study of α-Cr_2O_3/α-$Ni_{0.58}Cr_{1.42}O_{2.88}$ core-shell NPs, and Chapter Three will be on the overview of the different core shell NPs.

NOVEL HIGHLY-ORDERED AND Co(II)-CONTAINING α-Cr_2O_3/α-$Co_{0.43}Cr_{1.57}O_{2.9}$ CORE-SHELL NANOPARTICLES

Abstract

Core-shell nanoparticles have potential for a wide range of applications due to their tunability of magnetic, catalytic, electronic, optical and other physicochemical properties. A frequent drawback to practical applications in magnetic core-shell nanoparticles and nanocrystals is an extensive, disordered and compositionally distinct interface that occurs due to the dissimilarity of structural/compositional phases of the core and shell. We have developed a new hydrothermal nanophase epitaxy technique to synthesize well-ordered core-shell nanoparticles. Here I report on synthesis and physical characterization of novel well-ordered α-Cr_2O_3/α-$Co_{0.43}Cr_{1.57}O_{2.9}$ inverted core-shell nanoparticles (CSNs). My experimental results provide evidence for the continuity of the corundum structure beginning from the core and extending completely into the shell of the CSNs. The HR-TEM results show a sharp interface exhibiting epitaxial atomic registry of shell atoms over highly ordered core atoms. The XPS and Co K-edge XANES analyses indicate that the cobalt incorporated in the shell of the CSNs is in the +2 oxidation state. My XRD, XPS and EXAFS results are consistent with oxygen vacancy formation in order to maintain charge neutrality upon substitution of the Co^{2+} ion for the Cr^{3+} ion in the novel-phase α-$Co_{0.43}Cr_{1.57}O_{2.9}$ shell. The hydrothermal nanophase epitaxy technique is highly promising for synthesis of highly-ordered nanomaterials having enhanced magnetic, catalytic and other physicochemical properties.

Core-shell nanoparticles and nanocrystals are currently of considerable interest because their physicochemical properties are tunable by varying the core vs shell size, chemical composition, interface characteristics, and atomic-scale structure. This tunability has resulted in the ability to target a wide range of applications of core-shell nanostructures including in optics, catalysis, medicine, and energy storage.[1–4] Magnetic core-shell nanoparticles are of particular interest because of their potential applications in magnetic random access memory, spintronic devices, cell separation, tissue engineering, drug delivery, MRI targeted-cell imaging, and hyperthermia.[5–8] The increasing complexity of core-shell nanoparticles/nanocrystals (e.g. shape, type, arrangement, etc.), which is owed in strong measure to the tremendous advances in chemical synthesis methodologies being developed in scientific and industrial communities, has led not only to a high degree of control in the nature of targeted properties but also in the capability to tailor multifunctionality, such as having a combination of magnetic and catalytic properties.

Core-shell nanoparticles (CSNs) having distinct magnetic phases (in the core vs the shell regions) interacting via the exchange bias effect are presently extensively studied due to their potential industrial and medical applications.[5–8] The exchange bias effect results from the exchange anisotropy at the interface between the coupled magnetic phases of the core and shell. For example, conventional metal/metal oxide core-shell structures, such as Co-CoO,[9,10] Ni-NiO,[11–13] FeO-Fe_3O_4,[14] and MnO-Mn_3O_4,[15] are relatively easily prepared by oxidation of metal or further oxidation of metal oxide nanoparticles. An important structural aspect of CSNs is that aside from a few exceptional cases, the structural phases of the core and shell are distinct. The difference

in structure of the core vs shell phases typically results in considerable structural disorder, defect formation (e.g., vacancies), amorphization and roughness at the interface between the core and shell. The disorder, defects, roughness and extent of the interface relative to the sizes of the core and shell can have a strong but as yet not fully understood effect on the nature and extent of the exchange bias in CSNs. Disordered interfaces are thought to result in strong spin anisotropy or spin-glass type regions in CSNs. Monte Carlo simulations show that the presence of vacancies[16] and roughness[17] at the interface degrades the exchange bias whereas other calculations[18] show that the magnitude of the exchange bias field is strongly coupled to the degree of interface roughness in ferromagnetic (FM)-antiferromagnetic (AFM) core-shell nanoparticles. Progress in this area of nanoscience is complicated by the lack of atomic-scale control on the level of defects, roughness and disorder at the interface of two-phase core-shell nanoparticles and nanocrystals.

I have devised a novel hydrothermal nanophase epitaxy (HNE) technique for synthesis of crystalline CSNs having well-ordered interfaces. By mimicking natural processes of mineral zoning formation under hydrothermal conditions,[19] we are able to incorporate transition elements (M), such as Co(II), into a highly structurally ordered Cr_2O_3 – based shell, to form α-Cr_2O_3/α-$M_xCr_{2-x}O_y$ inverted CSNs. The inverted CSNs, having an AFM core and a FM or ferrimagnetic (FiM) shell, are of interest in part because of the reported magnetic proximity effect[20] and direct dependence of the exchange bias on shell thickness[21] in such systems. The advantage of my method is the production of CSNs having highly uniform structure throughout with minimal core-to-shell interface strain and roughness effects. Because the HNE process occurs at non-

equilibrium conditions in an aqueous environment, my synthesis offers a benign chemical route that results in the production of novel alloyed nanoparticle shells. The synthesis of such nanophases enables for the production of core-shell nanostructures having substantially enhanced physical (e.g., magnetic, optical) and chemical properties. Such nanomaterials may be optimally suited for tailored, multifunctional applications (e.g., magnetic and photocatalytic). In this work, I report the first synthesis of a novel highly-ordered α-$Co_{0.45}Cr_{1.55}O_{2.9}$ nanophase shell overgrown on the α-Cr_2O_3 core of my CSNs, using my HNE technique. The Co(II) divalent ion was chosen for epitaxial growth of the α-$Co_{0.43}Cr_{1.57}O_{2.9}$ shell over the α-Cr_2O_3 core in order to: (1) synthesize highly-ordered CSNs showing potential for exhibiting the exchange bias effect, and (2) to purposefully create oxygen vacancies that might enhance the magnetic, catalytic and other physicochemical properties of the nano-structures. I discuss investigations of the structural, compositional, morphological and metal-oxygen binding properties of α-Cr_2O_3/α-$Co_{0.43}Cr_{1.57}O_{2.9}$ CSNs. I show that the nanoparticles exhibit desirable magnetic properties as evidenced in the exchange bias effect occurring between the AFM α-Cr_2O_3 core and FM/FiM α-$Co_{0.43}Cr_{1.57}O_{2.9}$ shell.

Results and Discussion

In Figure 1.1 I show high resolution TEM (HR-TEM) analysis of a select α-Cr_2O_3/α-$Co_xCr_{2-x}O_y$ nanoparticle. The TEM results show that the CSNs are in fact quasi-spherical or nanocrystalline in terms of their morphology (see SI for additional TEM images). Distinct core and shell region are clearly visible in Figure 1.1 (a). For this typical nanoparticle, the shell region extends up to 6 nm.

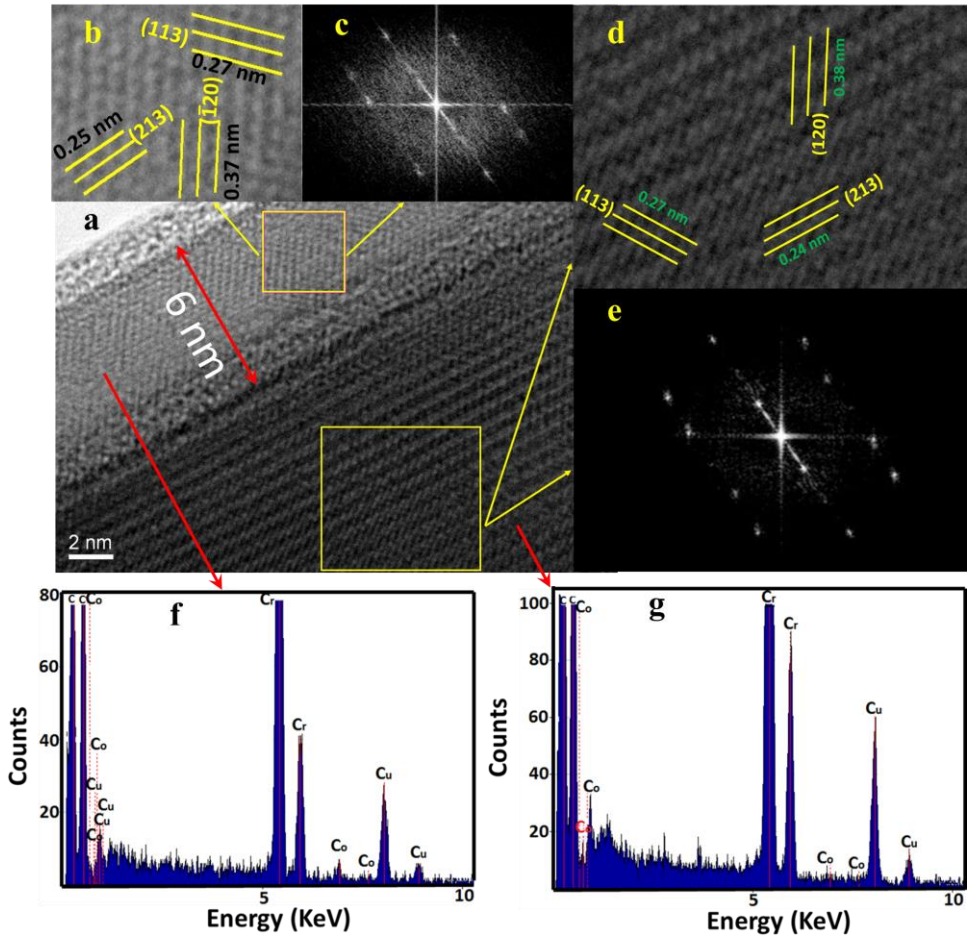

Figure 1.1 (a) An HR-TEM image of a single α-Cr_2O_3/α-$Co_xCr_{2-x}O_y$ nanoparticle that clearly shows the core (lower and towards the right) and shell (upper and towards the left); (b) A few selected lattice planes (labeled); (c) the FFT of the region of the shell shown in the outline in (a); (d) A few select lattice planes (labeled) and (e) the FFT of the region of the core shown in the outline in (a); the HR-TEM-EDX of the shell (f) and core (g) regions. The Cu Kα intensity in the EDX spectrum is due to the copper grid.

As shown in Figure 1.1 and additional HR-TEM images in the SI, the nanoparticles are crystalline throughout the core and shell region. Except for an abrupt break at the interface, the same atomic planes are continuous from the core to the shell (see Figure 1.1). A more detailed examination (see SI, Figure S1.5) shows this to be the case. The growth of the shell by the HNE method ensures a sharp, ordered interface between core and shell. The close similarity of the FFT's shown in Figures 1.1 (c) and (e)

of the core and shell, respectively, provides evidence of the continuity of the atomic planes throughout the nanoparticles. Figures 1.1 (b) and (d) show enlarged images of select regions of the core and shell regions, respectively, and a few of the atomic planes of the nanoparticle. The atomic plane distances (i.e., d-spacings) in the shell region for the same types of planes are slightly expanded compared to the interplanar spacing in the core region of the nanoparticles (NPs). Figures 1.1 (f) and (g) show the HR-TEM-EDX analysis of the core and shell regions of the individual nanoparticle. The EDX data show a higher percentage of Co present in the shell region of the nanoparticles whereas the core region is highly dominated by Cr. Our group previous *in situ* XAS studies of Ni and Co precipitation/incorporation on the surface and near surface region of Fe_3O_4 spinel nanoparticles in high P-T and low pH aqueous fluids suggest that the hydrothermal process involves partial dissolution of the NPs and co-deposition of the substitutional (i.e., Ni, Co) and host (Fe) cations during the epitaxial growth of surface layers.[22,23] It is likely that there is some inter-diffusion of host Cr and substitutional Co across the core/shell interface during the growth of the shell region. However, given that the temperature (~200 °C) of synthesis of the core-shell NPs is relatively low, I do not expect this to be very pronounced.

The lattice parameters of the core and shell portions, and the volume weighted mean size[24] of the nanoparticles, were determined from Rietveld refinement of the XRD data. The fit of the XRD data measured from the α-Cr_2O_3/α-$Co_xCr_{2-x}O_y$ CSNs is shown in Figure 1.2. The tabulated results from the structural refinement analyses of the XRD measured from the α-Cr_2O_3/α-$Co_xCr_{2-x}O_y$ CSNs are shown in the SI; the fit of the XRD data measured from the α-Cr_2O_3 NPs (prior to HNE) is shown in Figure S1.6. The sizes

of the α-Cr_2O_3 NPs were estimated to be 39(2) nm across from the XRD and TEM analysis (see SI). Figure 1.1 clearly shows the extent of an approximately 6 nm thick outer shell on a select α-Cr_2O_3/α-$Co_xCr_{2-x}O_y$ CSN. The final size of the α-Cr_2O_3/α-$Co_xCr_{2-x}O_y$ NPs was estimated to be 52(4) nm based on TEM analysis and Rietveld refinement of the XRD data. TEM-EDX data confirm (Figure 1.1 f and g) that the outer shell is rich in Co although both the core and the shell possess the same corundum structure.

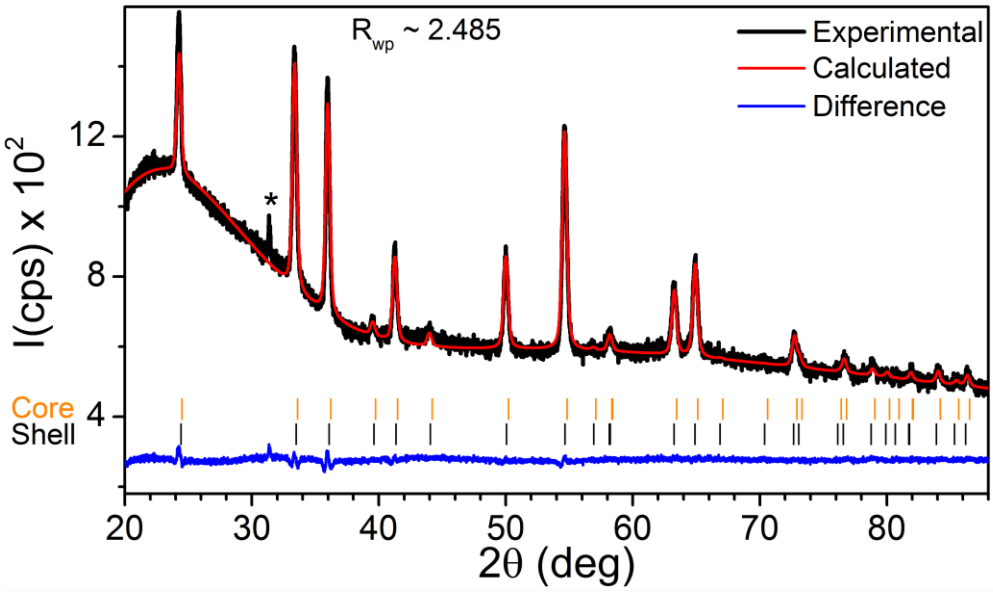

Figure 1.2. Plot of the XRD data and the Rietveld refinement of the structure of the core-shell α-Cr_2O_3/α-$Co_xCr_{2-x}O_y$ NPs. The core is comprised solely of Cr_2O_3 and the shell consist of $Co_xCr_{2-x}O_y$ ($x = 0.4$, $y = 2.9$ by refinement). Both the core and shell part conform to a corundum structure (space group #167). The '*' indicates an impurity peak.

The corundum unit cell of the shell region is slightly expanded compared to that of the core region due to replacement of some of the Cr^{3+} ions by the larger (ionic radius) Co^{2+} ions in the shell.

The k^3-weighted isolated EXAFS oscillations ($k^3 \bullet \chi(k)$) data, the Fourier transforms (FT) of the k^3-weighted Co *K*-edge χ data, along with the k^3-weighted inverse Fourier transform ($k^3 \bullet \tilde{\chi}(k)$) of the FT data and the fits to each of these data, are shown in Figure 1.3. The results for the structural parameters obtained from the fit of the Co K-edge EXAFS data are shown in Table 1.1.

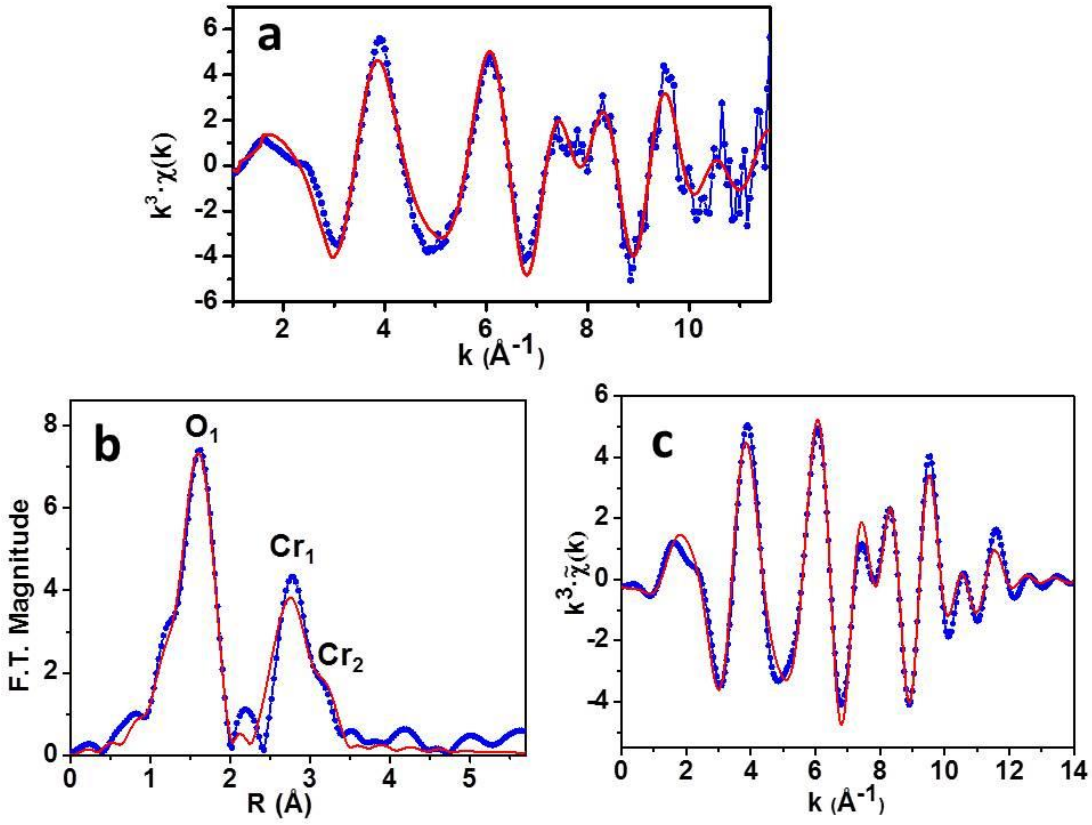

Figure 1.3. (a) The isolated k^3 weighted χ-data (blue line + solid circles) obtained from the XAS averaged spectrum measured at the Co-K edge from the core-shell α-Cr_2O_3/α-$Co_xCr_{2-x}O_y$ NPs and the fit to the data (red line); (b) the Fourier transform (FT) of the isolated χ-data (blue line + solid circles) shown in (a) and the fit (red line) to the data; (c) the inverse Fourier transform of the isolated χ-data (blue line + solid circles) and the fit (red line) to the data.

The fitting parameter errors shown in Table 1.1 are the statistical uncertainties as determined using IFEFFIT. The structural fitting parameters N, R, and σ^2 were determined using the calculated single scattering paths. The single scattering paths originate from the target Co atom and are projected to the surrounding O or Cr atoms. The EXAFS fitting results are consistent with Co undergoing substitution for Cr in solid solution leading to the formation of the $Co_xCr_{2-x}O_y$ phase with corundum structure, within the shell of the nanoparticles. This is most evident in the first (O_1), second (Cr_1) and third (Cr_2) shell distances (R) surrounding the Co central atom. The first, second and third shell distances are expanded by 0.5, 9 and 1%, respectively, surrounding Co relative to those surrounding Cr in the corundum structure (space group # 167; $R\bar{3}c$) of α-Cr_2O_3. The discrepancy in the second shell distance is, in significant measure, likely due to a path overlap contribution due to an intermediate shell of O atoms between the second and third shell Cr atoms surrounding Co in the corundum structure. Nevertheless, the overall expansion of the first, second, and third shell distances is consistent with my structural results obtained from the Rietveld refinement of the XRD data measured from the nanoparticles.

Table 1.1. Summary of structural results obtained from fitting of the Co K-edge EXAFS measured from the α-Cr_2O_3/α-$Co_xCr_{2-x}O_y$ core-shell nanoparticles.

Neighbor	Coordination number (N)	Distance to neighbor shell, R (Å)	σ^2 (Å^{-2})
O_1	5.8(6)	2.07(1)	0.0076(8)
Cr_1	4.7(6)	3.16(1)	0.009(2)
Cr_2	3.2(4)	3.47(3)	0.012(3)

The effective N_1, N_2 and N_3 coordination numbers for the first, second and third shells are 6 (3 O atoms at slightly shorter and 3 O atoms at slightly longer distance in the corundum structure), 4 (counting the Cr that is at a slightly shorter distance than 3 Cr nearby) and 3; respectively. I note that the Co-O distance of 2.07 Å compares very well with the Co-O near-neighbor distance in octahedral coordination measured in Co doped iron spinel NPs as determined using Co K-edge XAS data.[25] There are three O from the intermediate shell to the second and third Cr shells, but scattering from Cr is expected to dominate the EXAFS signal. The three oxygens from the intermediate (to second and third Cr shells) most likely contribute to the somewhat larger N_2 value of 4.7. The somewhat larger σ^2 values are indicative of a slightly disordered local structural environment surrounding Co in the shell region, which is consistent with size mismatch between the Co^{2+} and Cr^{3+} ions along with the epitaxial-growth induced strain imposed upon the lattice structure of the shell.

The close match between the calculated (using FEFF9) and experimentally measured XANES shown in Figure 1.4a is consistent with my XRD and EXAFS structural results and provides further evidence that the structural environment surrounding Co in the shell region of the nanoparticles is a corundum phase. All of the features beyond the pre-edge peak, which is situated ~ 10-12 eV below the inflection point of the sharp rise in the K-edge, are reasonably well matched by the calculated curve. The inset of Figure 1.4a shows the pre-edge peak after background subtraction. The pre-edge feature is primarily due to dipole-allowed transitions of 1s-electrons on the Co^{2+} ions to unoccupied mixed or hybridized 3d (Co) and p (Co, O) states. The pre-edge feature also has a considerably lesser contribution due to quadrupole-allowed Co 1s→3d

electronic transitions, which is evident as a weak shoulder on the high energy side of the overall peak shape. A doublet-shaped low-intensity peak observed in the pre-edge region is an indication of the crystal field (or molecular orbital) splitting of the Co 3d orbital sub-bands in an octahedrally distorted structure (i.e., distorted O_h symmetry) in the immediate vicinity of the Co site. Fitting of the background-subtracted pre-edge feature using Gaussian peak shapes yields 7709.8 eV for the dipole-allowed (A_1) and a 7711.6 eV value for the quadrupole-allowed (A_2) transition energies, respectively. These values are consistent with the A_1 and A_2 values of 7709.0 and 7711.7 eV, respectively, that we measured for Co^{2+} in octahedral site symmetry in $CoFe_2O_4$.[26]

The angular momentum projected density of states (*l*-DOS) calculation, which is shown in Figure 1.4b, was made using the same parameters that were used for calculation of the XANES. The *l*-DOS calculation shows that the pre-edge feature (labeled A) is dominated by d-DOS but also has substantial p-DOS and s-DOS contributions. This is consistent with transition of 1s electrons to half-filled 3d-(s,p) hybridized or mixed states that result from (distorted) octahedral crystal field splitting effects. After the pre-edge feature region, there is very little contribution from the d-DOS and contribution from both the s-DOS and p-DOS predominate. The *l*-DOS calculation shows that the shoulder feature (at ~7718 eV) in the XANES is dominated by contribution from the s-DOS and has a substantial contribution from the p-DOS (labeled B in Figure 1.4b). In addition, my *l*-DOS calculations show that the white line (C) and the shoulder features (D and E) of the XANES are dominated by the p-DOS but may in addition have some d-DOS character. This is indicative of dipole-allowed 1s to empty quasi-bound, continuum Co 4p-like state electronic transitions.

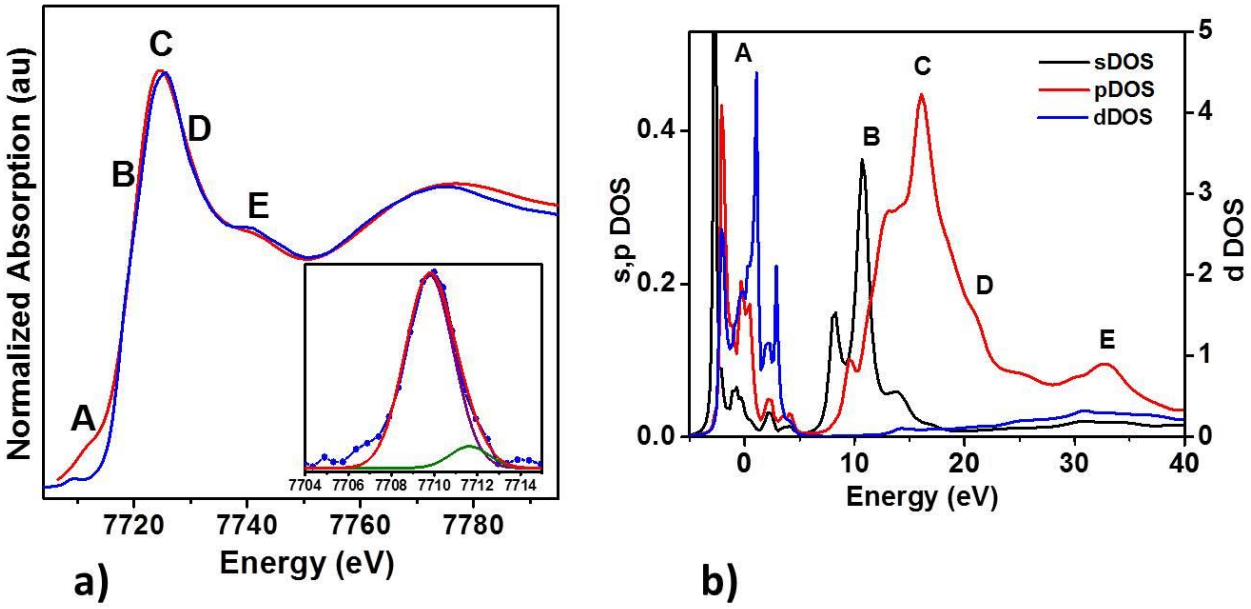

Figure 1.4. (a) The Co K-edge XANES measured from the α-Cr_2O_3/α-$Co_xCr_{2-x}O_y$ CSNs (blue line) and the simulated curve generated using the ab initio code FEFF9 (red line); the inset shows the overall pre-edge peak (blue line-data points), after background subtraction, and the two Gaussian peak shapes (green and purple lines; red line shows the overall fit) used to fit the pre-edge peak; (b) The angular momentum projected density of states (*l*-DOS) calculated using FEFF9.

The XPS survey scan (see SI) of my α-Cr_2O_3/α-$Co_xCr_{2-x}O_y$ CSNs shows that Cr, O and Co peaks are present, including a contribution from C 1s, which results from the carbon tape used to hold the sample in the chamber. The atomic percentages of the elements were determined from analysis of the Cr $2p_{3/2}$, O 1s, Co $2p_{3/2}$ peaks in the survey scan (see SI for tabulation of results). Figure 1.5 shows the high resolution XPS spectra of the Cr $2p_{3/2}$**,** Co $2p_{3/2}$ and O 1s peaks. Peak fitting of the Cr $2p_{3/2}$ peak was made by taking into account

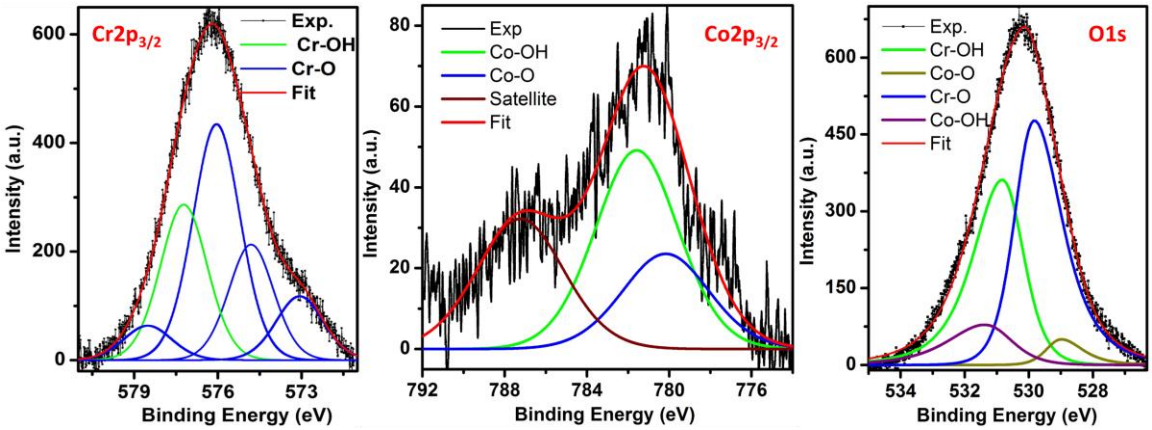

Figure 1.5. High resolution XPS spectra measured from the α-Cr_2O_3/α-$Co_xCr_{2-x}O_y$ CSNs (black line) and fits (colored lines) to the data for Cr $2p_{3/2}$ (left panel), Co $2p_{3/2}$ (middle panel), and O 1s (right panel).

the multiplet splitting which occurs due to the coupling between the unpaired electrons in the core with the unpaired electrons in the outer shell of the Cr^{3+} ion.[27] The peak at 577.22 eV is due to the presence of Cr-OH bonding in the nanoparticles whereas the remaining peaks that contribute to the Cr $2p_{3/2}$ overall peak are due to multiplet splitting. The Co $2p_{3/2}$ high resolution peak was deconvoluted into 3 peaks. The contribution from the sub-peak at 780.16 is due to Co-O bonding, which is indicative of the +2 oxidation state of the Co. There is a substantial satellite contribution in the Co $2p_{3/2}$ XPS feature whereas the remaining contributions arise from the bonding of the Co with OH radicals (at 781.51 eV). The O 1s peak was deconvoluted into 4 peaks. The dominant contributions stem from Cr-O and Cr-OH bonding whereas smaller contributions are observed from Co-O and Co-OH bonding in the sample. My detailed XPS data analysis results are tabulated in the SI.

My structural analysis using XRD, XAS (EXAFS and XANES), and HR-TEM indicates that the Co-incorporated shell of the α-Cr_2O_3/α-$Co_xCr_{2-x}O_y$ inverted CSNs has the corundum structure. The HR-TEM analysis shows that the core-shell interface of the

NPs is relatively sharp and that the shell is in atomic (i.e., epitaxial) registry with the core. Both the XANES and XPS results are consistent with the +2 oxidation state of Co in the NPs. The +2 oxidation state of Co in the NPs is consistent with a high-spin state = 3/2 due to the (distorted) octahedral crystal-field d-orbital splitting effects. My results are in complete agreement with substitutional solubility of Co(II) within the α-$Co_xCr_{2-x}O_y$ shell of the nanoparticles. Based on the XPS elemental analysis, I estimate that the x value (i.e., atomic fraction) of Co in the shell is 0.43 (see SI). In addition, based on my XRD and XPS results, I estimate that the α-$Co_xCr_{2-x}O_y$ shell of the NPs is slightly oxygen deficient due to charge compensation upon substitution of the Co^{2+} for Cr^{3+} ion; thus, the stoichiometric formula for the shell is $Co_{0.43}Cr_{1.57}O_{2.9}$ (see SI for calculation details). My EXAFS result for N_1 (5.8) first-shell oxygen coordination number of Co is also consistent with a slight oxygen substoichiometry in the shell region. To my knowledge, this is the first report of a successful synthesis of a corundum-structured, Co(II)-containing α-$Co_xCr_{2-x}O_y$ either in bulk or nanophase form. Bodade *et al.*[28] reported synthesis of Co-doped Cr_2O_3 NPs but provide no direct evidence for Co incorporation, Co oxidation state or the structure of the NPs. The synthesis of CSNs via the HNE method is a very exciting prospect for creation of novel magnetic nano-materials as it affords the opportunity to synthesize new nano-phases and nearly ideal inverted CSNs.

My XRD and EXAFS results show that, on the average, the lattice parameters for the α-$Co_{0.43}Cr_{1.57}O_{2.9}$ shell are slightly larger than for the α-Cr_2O_3 core of my nanoparticles. The Shannon ionic radius of Co^{2+} (0.745 Å: high spin state) is larger than that of Cr^{3+} ion (0.615 Å).[29] The results from the fitting of the XRD data show

approximately 0.3 % elongation in the lattice parameters (i.e., ~ 1% volume expansion) for the α-$Co_{0.43}Cr_{1.57}O_{2.9}$ shell vs those for the α-Cr_2O_3 core of the nanoparticles (see SI). I note that the average Co-O first shell distance measured from EXAFS is 2.07(1) Å, which is slightly longer than the same value obtained from Rietveld refinement of the XRD data (2.01(1) Å). This discrepancy is attributed to the fact that EXAFS probes the local structure (surrounding Co) whereas XRD probes the extended structure of condensed matter. Based on purely ionic bonding principles, I should expect approximately a 6-7 % expansion of the lattice parameters of the corundum-phase shell region. However, the effective radius of the cobalt ion may be shorter than the value predicted purely on ionic bonding principles because of a covalent contribution to the Co-O bonding in the α-$Co_{0.43}Cr_{1.57}O_{2.9}$ shell. Thus, my analysis indicates that some degree of covalent character in the Co-O bonding may be present in the α-$Co_{0.43}Cr_{1.57}O_{2.9}$ shell. Indeed, my *ab initio* modeling of α-Cr_2O_3/α-$Ni_xCr_{2-x}O_y$ CSNs shows that Ni-O bonding has a significant covalent contribution in the α-$Ni_{0.57}Cr_{1.43}O_3$ shell region.[30]

One of the outstanding issues in conventional (inverted or otherwise) CSNs is roughness of the core-shell interface, due to the dissimilarity of the core and shell structural phases. The interface roughness can result in a substantial spin anisotropy that can adversely affect the degree of exchange bias between the core and shell of the NPs.[18] The interface roughness coupled with elemental diffusion can be so substantial as to warrant modeling of magnetic core-shell nanoparticles with an intermediate shell reflecting the interface layer: This was well evidenced by Juhin et al.[8] in the case of γ–Fe_2O_3/Mn_3O_4 CSNs having a 3 nm-radius core, a 3 nm thick intermediate interface layer and a Mn_3O_4 shell with 0 – 2 nm thickness. My HNE technique avoids the disorder

effects imposed by the mismatch of dissimilar core vs shell structural phases that is common in other synthesis methods, thereby producing a much sharper, well-defined core-shell interface which should have a strong impact on the spatial extent of the interface-induced spin anisotropy. This should result in a greater control of design and, potentially, more enhanced exchange bias effect between the AFM core and the FM or FiM shell in inverted CSNs synthesized using my HNE technique. In addition, such nanoparticles having well-defined, sharp core-shell interfaces will be much easier to model and thereby obtain a much clearer understanding of the role of the interface in impacting upon the exchange bias effect in inverted CSNs.

My objective in the design of the inverted CSNs was to incorporate a charge deficient cation that substitutes for the Cr^{3+} ion in order to synthesize a shell with a nominally significant number of oxygen vacancies. My EXAFS, XRD and XPS results are consistent with nominal oxygen vacancy formation surrounding the Co sites in the $Co_{0.43}Cr_{1.57}O_{2.9}$ shell. The formation of oxygen vacancies is consistent with charge compensation due to substitution of divalent Co(II) for the trivalent Cr(III) ion in the α-$Co_{0.43}Cr_{1.57}O_{2.9}$ shell. The oxygen-vacancy induced F-center exchange has been shown to result in FM coupling of cation spins in undoped CeO_2 nanocrystalline films[35] and in Fe^{3+}-doped CeO_2 nanoparticles[36]. The F-center exchange coupling occurs by interaction between the oxygen vacancy and nearby cation spins.[33] An electron becomes trapped in the vicinity of the oxygen vacancy, which thereby acts as an F-center. The orbital of the F-center trapped electron (having antiparallel spin alignment) overlaps with the d-orbitals of neighboring (Co or Cr) cation, forming a bound magnetic polaron[32,34,35] which results in the long-range F-center exchange FM coupling of neighboring spins. This should

result in Co-Co FM, and, potentially Co-Cr FM coupling in the α-$Co_{0.43}Cr_{1.57}O_{2.9}$ shell of my inverted core-shell α-Cr_2O_3/α-$Co_{0.43}Cr_{1.57}O_{2.9}$ NPs. Indeed, my preliminary magnetization measurements show that there is FM or FiM coupling in the α-$Co_{0.45}Cr_{1.55}O_{2.9}$ shell and that there is a small shift between the zero field cooled (ZFC) and field cooled (FC) hysteresis, indicating that there is an exchange bias effect between the shell and core of the nanoparticles (see SI). Magnetic studies of my α-Cr_2O_3/α-$Co_{0.43}Cr_{1.57}O_{2.9}$ inverted CSNs are currently underway and will be reported in a separate article. In addition, the considerable surface anisotropy combined with distortional anisotropy induced by lattice distortion due to Co(II)-Cr(III) ionic size mismatch may provide for an overall canting of spins, thereby providing a contribution to the overall FM or FiM character in the α-$Co_{0.43}Cr_{1.57}O_{2.9}$ shell of my inverted CSNs. My on-going magnetic and computational investigations are designed to resolve the nature of magnetism and the extent of the exchange bias core-shell interaction in my inverted CSNs. In addition to potentially significantly impacting upon the magnetic properties, the formation of oxygen vacancies (particularly on the surface) may offer enhanced catalytic (i.e., photocatalysis) and gas sensing properties of my core-shell nanoparticles.

Conclusion

I have successfully synthesized a novel α-$Co_{0.43}Cr_{1.57}O_{2.9}$ nano-phase shell having the corundum structure over α-Cr_2O_3 nanoparticles, to form α-Cr_2O_3/α-$Co_{0.43}Cr_{1.57}O_{2.9}$ inverted core-shell nanoparticles, using my hydrothermal nanophase epitaxy technique. HR-TEM analysis indicates that the α-Cr_2O_3 core is on the average ~ 40 nm across with a ~ 6 nm thick α-$Co_{0.43}Cr_{1.57}O_{2.9}$ shell of the core-shell nanoparticles. Structural analysis

using XRD, XAS and HR-TEM indicates that the corundum structure of the nanoparticle is continuous from core to the shell with a slight expansion (~ 1%) of the unit cell volume of the α-$Co_{0.43}Cr_{1.57}O_{2.9}$ shell, in comparison to that of the α-Cr_2O_3 core. Combined result from XAS and XPS provide evidence of oxygen vacancy formation to maintain the charge neutrality in the shell region of the nanoparticles and the +2 oxidation state of substitutional Co (for Cr) in the α-$Co_{0.43}Cr_{1.57}O_{2.9}$ shell. Both the oxygen vacancy formation and the +2 oxidation state of Co, which is consistent with a high-spin state = 3/2 due to octahedral crystal-field d-orbital splitting, may contribute toward the establishment of ferro/ferrimagnetic characteristics of the shell region. The evidence presented in this work shows that the core-shell interface is well ordered and sharp, which may enhance the core-shell exchange bias effect between the antiferromagnetic core and ferro/ferrimagnetic shell. The hydrothermal nanophase epitaxy technique has been demonstrated as a highly promising benign route for synthesis of novel nanophases having sharp interfaces and well-ordered core-shell structure. The structural and compositional control inherent in the hydrothermal nanophase epitaxy technique offers opportunity to produce core-shell nanoparticles having enhanced magnetic, catalytic and other physicochemical properties.

Experimental Methods

Nanoparticle synthesis. The Cr_2O_3 nanoparticles (NPs) used in this study were synthesized following the procedure outlined in Farzaneh et al.[36] A 0.2 m solution of commercially available $Cr(NO_3)_3.9H_2O$ (Sigma-Aldrich) was prepared and then mixed with an organic surfactant Triethanolamine (TEOA) in 1:2 molar ratio. The solution was

magnetically stirred for approximately 1 hour and then placed under microwave irradiation for 5 minutes. Then, the solution was placed on top of a bar magnet and a dark-green color precipitate collected at the bottom after approximately 6 hours. This precipitate was separated from the solution and then dried in air. Next, the precipitate was calcined in air by heating at a rate of 10 °C/min to 575 °C, keeping at 575 °C for 2 hours, and finally cooling down to room temperature at 10 °C/min. The sample turned into a green-colored fine powder at the conclusion of the calcination process. Characterization was made by X-ray diffraction (XRD), Scanning Electron Microscopy (SEM) and Transmission Electron Microscopy (TEM) techniques.

Commercially available $CoCl_2$ (Online Science Mall) was dissolved in deionized water (deoxygenated by passing N_2 gas for 15 minutes) to prepare a 0.05 m aqueous solution (pH = 6.1) of $CoCl_2$. Cr_2O_3 NPs were added at a quantity of 0.09 g to 10 ml of the $CoCl_2$ solution. The solution was sonicated for approximately 15 minutes immediately after preparation and also before loading into our lab high-temperature Hastelloy C-276 hydrothermal reactor,[37] in order to perform the hydrothermal nanophase epitaxy. The nanoparticle/aqueous-solution mixture was heated to ~205 °C and held at that temperature for approximately 17 hours before cooling to room temperature, in order to grow the α-$Co_xCr_{2-x}O_y$ shell on the α-Cr_2O_3 NPs. After the hydrothermal nanophase epitaxy, the nanoparticles were rinsed using DI water and a centrifuge and dried on a glass plate in air at 25 °C.

Transmission electron microscopy. TEM images of the Cr_2O_3 and Cr_2O_3-$Co_xCr_{2-x}O_y$ inverted core-shell NPs were collected at the GeoForschungZentrum using a TECNAI G2 F20 X-Twin microscope. The field emission gun of the HR-TEM was

operated at 200 keV. High-resolution lattice fringe images were acquired with a Gatan imaging filter (GIF Tridiem) as energy filtered images applying a 20 eV window to the zero-loss peak. Diffraction patterns were calculated from the high-resolution lattice fringe images using Fast Fourier Transform (FFT) from the Digital Micrograph inside the ImageJ software packages.

X-ray diffraction. Room temperature X-ray diffraction (XRD) measurements ($\theta - 2\theta$ scan) were made on the as prepared Cr_2O_3 NPs and the core-shell α-Cr_2O_3/α-$Co_xCr_{2-x}O_y$ NPs with a powder diffractometer (Bruker D8 Discover) using Cu Kα radiation from a sealed tube operating at 40 kV and 30 mA. A Gobel mirror and a 0.6 mm slit were used in the incident side of the x-ray beam followed by a 0.6 mm slit on the side of the diffracted beam. Structural parameters were extracted from the XRD patterns using the Bruker TOPAS full-pattern refinement program.[38–40] The zero error and incident beam profile of the instrument were determined using a modified Thompson-Cox-Hastings pseudo-Voigt peak function (TCHZ)[41] from a NIST 674b standard reference material (CeO_2). The peak asymmetry due to axial divergence of the beam was modelled using the NIST 674b CeO_2 standard based on work by Finger et al.[42] The zero error of the instrument, parameters of the TCHZ peak function describing the incident beam profile, and axial divergence of the beam were fixed during the subsequent structural refinement of the samples. The background function for the XRD pattern was modelled using a Chebychev Polynomial of 5-th order as well as a *1/X* background function.[38] The amorphous like background of the XRD data from α-Cr_2O_3/α-$Co_xCr_{2-x}O_y$ NPs came from the glass substrate used to hold the particles and was modelled using a broad Voigt

function. A non-linear least square fitting method was performed to minimize the value of "R-weighted pattern" (R_{wp}) during Rietveld refinement.

X-ray diffraction data analysis. Symmetry mode Rietveld refinement[43–45] was made on both the as prepared Cr_2O_3 NPs and the core-shell α-Cr_2O_3/α-$Co_xCr_{2-x}O_y$ NPs with a corundum structure (space group #167 or $R\bar{3}c$) based on ICSD # 261801 as the starting structure. The lattice parameters of the corundum unit cell, z-position of the Cr atom, x-positon of the O atom and the temperature factors for both Cr and O were refined for the α-Cr_2O_3 NPs. The structural parameters of the core part of the core-shell α-Cr_2O_3/α-$Co_xCr_{2-x}O_y$ NPs were constrained to the value determined from the refinement of the structure of the α-Cr_2O_3 NPs. For the structural refinement of the shell region, Cr and Co atoms with partial site occupancies were used to occupy the cation sites in the corundum structure. The partial site occupancies of the Co, Cr and O (to account for oxygen vacancy formation) atoms were refined along with the lattice parameters, z-position of the Co and Cr atoms, x-position of the O atom with the respective temperature factors constrained to the value obtained for the Cr_2O_3 NPs. Additional experimental details are given in the SI.

XAS measurements. Co *K*-edge XAS measurements were performed on the α-Cr_2O_3/α-$Co_xCr_{2-x}O_y$ inverted core-shell NPs at the PNC/XSD beam line 20-BM-B at the Advanced Photon Source (APS). The spectra were measured in fluorescence mode using 13-element Ge solid-state detector. The APS synchrotron was operated at an energy of 7.0 GeV with a maximum fill current of 100 mA. (324 bunch). The incident x-ray beam flux at the 20-BM-B beam line was ~$2x10^9$ photons/second as measured using an N_2-filled transmission chamber before the sample. The Si(111) double-crystal

monochromator was detuned by 20% 300 eV above the Co edge and a Rh-coated harmonic rejection mirror was also used. Cobalt *K*-edge calibration was accomplished using cobalt metal foil. The overall spectrum that was used in the analyses was averaged from 60 individual scans.

EXAFS data analysis. Reduction of the XAS spectrum was carried out using ATHENA1.2 software.[46] The nonlinear least squares fitting of the χ data, which are the isolated extended x-ray absorption fine structure (EXAFS) oscillations, was made using IFEFFIT0.9.[47] The k^3-weighted χ data were Fourier transformed in the 3.0 to 13.0 $Å^{-1}$ k-space range. The Fourier-tranformed (FT) χ data were fit in R-space, in the 1.3 – 3.5 Å range using theoretical XAS curves generated with FEFF9.[48] An orthorhombic corundum-type structure (space group # 167 or $R\bar{3}c$) model consisting of 58 atoms was used in the theoretical XAS calculation. The structure model consists of the Co atom at the center with Cr and O atoms occupying the remaining sites. In reality, there are additional Co in the outer shells surrounding the central Co atom in the α-Cr_2O_3/α-$Co_xCr_{2-x}O_y$ NPs. However, Co-Co scattering was not explicitly taken into account, by use of a separate scattering path, in order to simplify the analysis. Three single scattering Co-A (A = O, Cr) paths, generated using FEFF9, were used to fit the Co K-edge χ data. The fitting parameters include the coordination number (N), the radial distance (R), the mean square relative displacement (MSRD: σ^2) of the XAS Debye-Waller factor, and ΔE_0, for each path. ΔE_0 is defined as the difference between the calculated Fermi level and the absorption edge position as determined by the main peak in the first derivative of the absorption. An amplitude normalization factor $S_0^2 = 0.7$ was used in the calculation of the

coordination number N of each path. The goodness of fit parameter (R_{fit}) as implemented in IFFEFIT was 0.034.

XANES data analysis. After processing, the XANES were isolated from the XAS spectra and normalized with respect to the individual step height values. The ab initio XANES calculations were made using FEFF9.[24] The atomic cluster model utilized in the calculations consists of a central Co atom surrounded by Cr, Co and O atoms simulating an α-$Co_{0.5}Cr_{1.5}O_3$ corundum structure of 58 atoms. The Co *K*-edge XANES and the associated angular momentum projected density of states (*l*-DOS) calculations were made simultaneously. The self-consistent field (SCF) potential calculations utilized Hedin-Lundqvist[49] potentials and were made in full multiple scattering mode. A dispersion value of 0.2 eV was used in the calculations to simulate the effects of instrument and core-hole lifetime broadening. The discontinuities between adjacent regions of the muffin-tin potentials were reduced by a slight overlap via an AFOLP value of 1.09. A mean square relative disorder parameter of the Debye-Waller factor of 0.016 $Å^{-1}$ was used in the calculations.

X-ray photoelectron Spectroscopy. Compositional analysis of the sample was made using x-ray photoelectron spectroscopy (XPS). Twin crystal monochromatic Al K-alpha with a characteristic energy of 1486.6 eV was used as a source of x-rays. The Ag $3d_{5/2}$ (FWHM=0.36 eV) peak with a characteristic energy of 368.26 eV was used for calibration of the source and analyzer. The XPS data were collected using a Thermo Scientific Alpha 110 hemispherical analyzer with pass energy of 25 eV. The CasaXPS 2.3.16 software was used for analysis and peak fitting of the XPS spectra. The high resolution scans, including the survey scan, were calibrated with respect to the C 1s peak

with a fixed value of 284.8 eV. A Shirley background within the CasaXPS software was used in the fitting of the XPS peaks in the survey scan in the high resolution spectra. A Gaussian-Lorentzian product GL(30) function was used for relatively symmetric line shapes whereas a Lorentzian functional form convoluted with a Gaussian LA(a,b,n) function was used in the fitting of asymmetric line shapes of the high resolution peaks.

Associated Content

Supporting information (SI). Estimation of the Co concentration in α-Cr_2O_3/α-$Co_xCr_{2-x}O_y$ Core-Shell NPs, SEM image showing quasi-spherical morphology of the NPs, SEM-EDX, multiple TEM images and HR-TEM analysis of the core and the shell region of the NPs, Rietveld refinement of the structure of the α-Cr_2O_3 NPs, XPS survey scan and summary of the peak fitting results, and magnetic hysteresis measurements.

Acknowledgments

S.D. and R.M. acknowledge partial support from EFree, an Energy Frontier Research Center funded by the US Department of Energy, Office of Science, Office of Basic Energy Sciences under Award Number DE-SC0001057. The PNC/XOR facilities at the APS, and research at these facilities, are supported by DOE–BES, a Major Resources Support (MRS) grant from NSERC, the University of Washington, Simon Fraser University and the Advanced Photon Source. Use of the Advanced Photon Source is also supported by DOE–BES, under contract DE-AC02-06CH11357. I thank Alexander Jankovic and the JVIC center at MSU for assistance with the XPS measurements on mysamples.

Abbreviations

CS Core-shell; NP Nanoparticle; FM Ferromagnetic; AFM Antiferromagnetic; FiM Ferromagnetic; HNE Hydrothermal Nanophase Epitaxy; FFT Fast Fourier Transformation; FT Fourier Transformation.

References

(1) Borys, N. J.; Walter, M. J.; Huang, J.; Talapin, D. V.; Lupton, J. M. The Role of Particle Morphology in Interfacial Energy Transfer in CdSe/CdS Heterostructure Nanocrystals. *Science* **2010**, *330*, 1371–1374.

(2) Byers, C. P.; Zhang, H.; Swearer, D. F.; Yorulmaz, M.; Hoener, B. S.; Huang, D.; Hoggard, A.; Chang, W.-S.; Mulvaney, P.; Ringe, E.; *et al.* From Tunable Core-Shell Nanoparticles to Plasmonic Drawbridges: Active Control of Nanoparticle Optical Properties. *Sci. Adv.* **2015**, *1*, e1500988.

(3) Gawande, M. B.; Goswami, A.; Asefa, T.; Guo, H.; Biradar, A. V.; Peng, D.-L.; Zboril, R.; Varma, R. S. Core–shell Nanoparticles: Synthesis and Applications in Catalysis and Electrocatalysis. *Chem. Soc. Rev.* **2015**, *44*, 7540–7590.

(4) Song, S.; Wang, X.; Zhang, H. CeO2-Encapsulated Noble Metal Nanocatalysts: Enhanced Activity and Stability for Catalytic Application. *NPG Asia Mater.* **2015**, *7*, e179.

(5) Wang, J.; Zeng, X. C. Core–Shell Magnetic Nanoclusters. In *Nanoscale Magnetic Materials and Applications*; Liu, J. P.; Fullerton, E.; Gutfleisch, O.; Sellmyer, D. J., Eds.; Springer US, 2009; pp. 35–65.

(6) Silva, A.; Silva-Freitas, rica; Carvalho, J.; Pontes, T.; Arajo-Neto, R.; Silva, K.; Carrio, A.; Egito, E. Magnetic Particles in Biotechnology: From Drug Targeting to Tissue Engineering. In *Advances in Applied Biotechnology*; Petre, M., Ed.; InTech, 2012.

(7) López-Ortega, A.; Estrader, M.; Salazar-Alvarez, G.; Roca, A. G.; Nogués, J. Applications of Exchange Coupled Bi-Magnetic Hard/soft and Soft/hard Magnetic Core/shell Nanoparticles. *Phys. Rep.* **2015**, *553*, 1–32.

(8) Juhin, A.; López-Ortega, A.; Sikora, M.; Carvallo, C.; Estrader, M.; Estradé, S.; Peiró, F.; Baró, M. D.; Sainctavit, P.; Glatzel, P. Direct Evidence for an

Interdiffused Intermediate Layer in Bi-Magnetic Core–shell Nanoparticles. *Nanoscale* **2014**, *6*, 11911–11920.

(9) Inderhees, S. E.; Borchers, J. A.; Green, K. S.; Kim, M. S.; Sun, K.; Strycker, G. L.; Aronson, M. C. Manipulating the Magnetic Structure of Co core/CoO Shell Nanoparticles: Implications for Controlling the Exchange Bias. *Phys. Rev. Lett.* **2008**, *101*, 117202.

(10) Wiedwald, U. Interface Magnetism in Co/CoO Core-Shell Nanoparticles and Their Transformation to Pure Metallic Nanoparticles, Universität Duisburg-Essen, Fakultät für Physik, 2004.

(11) D'Addato, S.; Spadaro, M. C.; Luches, P.; Grillo, V.; Frabboni, S.; Valeri, S.; Ferretti, A. M.; Capetti, E.; Ponti, A. Controlled Growth of Ni/NiO Core–shell Nanoparticles: Structure, Morphology and Tuning of Magnetic Properties. *Appl. Surf. Sci.* **2014**, *306*, 2–6.

(12) Seto, T.; Akinaga, H.; Takano, F.; Koga, K.; Orii, T.; Hirasawa, M. Magnetic Properties of Monodispersed Ni/NiO Core-Shell Nanoparticles. *J. Phys. Chem. B* **2005**, *109*, 13403–13405.

(13) Singh, M. K.; Agarwal, A.; Swarnkar, R. K.; Gopal, R.; Kotnala, R. K. Magnetic Properties of Ni/NiO Core–Shell Nanoparticles Synthesized by Nanosecond Laser Irradiance of Water Suspended Ni Particles. *Sci. Adv. Mater.* **2012**, *4*, 532–536.

(14) Khurshid, H.; Chandra, S.; Li, W.; Phan, M. H.; Hadjipanayis, G. C.; Mukherjee, P.; Srikanth, H. Synthesis and Magnetic Properties of Core/shell FeO/Fe_3O_4 Nano-Octopods. *J. Appl. Phys.* **2013**, *113*, 17B508.

(15) Berkowitz, A. E.; Rodriguez, G. F.; Hong, J. I.; An, K.; Hyeon, T.; Agarwal, N.; Smith, D. J.; Fullerton, E. E. Antiferromagnetic MnO Nanoparticles with Ferrimagnetic Mn_3O_4 Shells: Doubly Inverted Core-Shell System. *Phys. Rev. B* **2008**, *77*, 024403.

(16) Mao, Z.; Zhan, X.; Chen, X. Defect-Tuning Exchange Bias of Ferromagnet/antiferromagnet Core/shell Nanoparticles by Numerical Study. *J. Phys. Condens. Matter* **2012**, *24*, 276002.

(17) Dimitriadis, V.; Kechrakos, D.; Chubykalo-Fesenko, O.; Tsiantos, V. Shape-Dependent Exchange Bias Effect in Magnetic Nanoparticles with Core-Shell Morphology. *Phys. Rev. B* **2015**, *92*, 064420.

(18) Evans, R. F. L.; Bate, D.; Chantrell, R. W.; Yanes, R.; Chubykalo-Fesenko, O. Influence of Interfacial Roughness on Exchange Bias in Core-Shell Nanoparticles. *Phys. Rev. B* **2011**, *84*, 092404.

(19) Jamtveit, B. Crystal Growth and Intracrystalline Zonation Patterns in Hydrothermal Environments. In *Growth, Dissolution and Pattern Formation in Geosystems*; Jamtveit, B.; Meakin, P., Eds.; Springer Netherlands, 1999; pp. 65–84.

(20) Golosovsky, I. V.; Salazar-Alvarez, G.; López-Ortega, A.; González, M. A.; Sort, J.; Estrader, M.; Suriñach, S.; Baró, M. D.; Nogués, J. Magnetic Proximity Effect Features in Antiferromagnetic/Ferrimagnetic Core-Shell Nanoparticles. *Phys. Rev. Lett.* **2009**, *102*, 247201.

(21) Vasilakaki, M.; Trohidou, K. N.; Nogués, J. Enhanced Magnetic Properties in Antiferromagnetic-Core/Ferrimagnetic-Shell Nanoparticles. *Sci. Rep.* **2015**, *5*, 9609.

(22) Mayanovic, R. A.; Yan, H.; Anderson, A. J.; Meredith, P. R.; Bassett, W. A. In Situ X-Ray Absorption Spectroscopic Study of the Adsorption of Ni2+ on Fe3O4 Nanoparticles in Supercritical Aqueous Fluids. *J. Phys. Chem. C* **2012**, *116*, 2218–2225.

(23) Yan, H.; Mayanovic, R. A.; Demster, J. W.; Anderson, A. J. In Situ Monitoring of the Adsorption of Co2+ on the Surface of Fe3O4 Nanoparticles in High-Temperature Aqueous Fluids. *J. Supercrit. Fluids* **2013**, *81*, 175–182.

(24) Balzar, D.; Audebrand, N.; Daymond, M. R.; Fitch, A.; Hewat, A.; Langford, J. I.; Le Bail, A.; Louër, D.; Masson, O.; McCowan, C. N. Size-Strain Line-Broadening Analysis of the Ceria Round-Robin Sample. *J. Appl. Crystallogr.* **2004**, *37*, 911–924.

(25) Carta, D.; Casula, M. F.; Falqui, A.; Loche, D.; Mountjoy, G.; Sangregorio, C.; Corrias, A. A Structural and Magnetic Investigation of the Inversion Degree in Ferrite Nanocrystals MFe_2O_4 (M= Mn, Co, Ni). *J. Phys. Chem. C* **2009**, *113*, 8606–8615.

(26) Yan, H.; Mayanovic, R. A.; Demster, J.; Anderson, A. J. In Situ XANES Study of Co2+ Ion Adsorption on Fe3O4 Nanoparticles in Supercritical Aqueous Fluids. In *Symposium A – Material Challenges in Current and Future Nuclear Technologies*; MRS Online Proceedings Library; 2012; Vol. 1383.

(27) Ünveren, E.; Kemnitz, E.; Hutton, S.; Lippitz, A.; Unger, W. E. S. Analysis of Highly Resolved X-ray Photoelectron Cr 2p Spectra Obtained with a Cr_2O_3 Powder Sample Prepared with Adhesive Tape. *Surf. Interface Anal.* **2004**, *36*, 92–95.

(28) Bodade, A. B.; Rohokale, P. G.; Padole, P. R. Electrical and Gas Sensing Properties of Chemically Modified Nanocrystalline Cr_2O_3 Based H_2S Sensor. *Nano Trends: J. Nanotech. Appl.* **2011**, *11*, 18–21.

(29) Shannon, R. t. Revised Effective Ionic Radii and Systematic Studies of Interatomic Distances in Halides and Chalcogenides. *Acta Crystallogr. A* **1976**, *32*, 751–767.

(30) Hossain, M. D.; Dey, S.; Mayanovic, R. A.; Sakidja, R.; Benamara, M. The Exchange Bias Effect in Novel Inverted Core-Shell Cr2O3-NixCr2-xO3 Nanoparticles. *unpublished*.

(31) Fernandes, V.; Mossanek, R. J. O.; Schio, P.; Klein, J. J.; De Oliveira, A. J. A.; Ortiz, W. A.; Mattoso, N.; Varalda, J.; Schreiner, W. H.; Abbate, M. Dilute-Defect Magnetism: Origin of Magnetism in Nanocrystalline CeO_2. *Phys. Rev. B* **2009**, *80*, 035202.

(32) Phokha, S.; Pinitsoontorn, S.; Maensiri, S. Structure and Magnetic Properties of Monodisperse Fe^{3+}-Doped CeO_2 Nanospheres. *Nano-Micro Lett.* **2013**, *5*, 223–233.

(33) Chandra, S.; Khurshid, H.; Li, W.; Hadjipanayis, G. C.; Phan, M. H.; Srikanth, H. Spin Dynamics and Criteria for Onset of Exchange Bias in Superspin Glass Fe/γ-Fe_2O_3 Core-Shell Nanoparticles. *Phys. Rev. B* **2012**, *86*, 014426.

(34) Kumar, S.; Kim, Y. J.; Koo, B. H.; Lee, C. G. Structural and Magnetic Properties of Ni Doped CeO_2 Nanoparticles. *J. Nanosci. Nanotechnol.* **2010**, *10*, 7204–7207.

(35) Durst, A. C.; Bhatt, R. N.; Wolff, P. A. Bound Magnetic Polaron Interactions in Insulating Doped Diluted Magnetic Semiconductors. *Phys. Rev. B* **2002**, *65*, 235205.

(36) Farzaneh, F. Synthesis and Characterization of Cr_2O_3 Nanoparticles with Triethanolamine in Water under Microwave Irradiation. *J. Sci. Islam. Repub. Iran* **2011**, *22*, 329–333.

(37) McCart, P. A.; Farris, L.; Mayanovic, R. A.; Yan, H. Investigations of TiO2 Nanoparticles Surface-Doped with Eu in Aqueous Fluids to High P-T Conditions. In *Symposium DDD – Extreme Environments—A Route to Novel Materials*; MRS Online Proceedings Library Archive; 2013; Vol. 1582.

(38) *TOPAS V4: General Profile and Structure Analysis Software for Powder Diffraction Data.- User's Manual*; Bruker AXS, Karlsruhe, Germany, 2008.

(39) Cheary, R. W.; Coelho, A. A Fundamental Parameters Approach to X-Ray Line-Profile Fitting. *J. Appl. Crystallogr.* **1992**, *25*, 109–121.

(40) Coelho, A. A. Indexing of Powder Diffraction Patterns by Iterative Use of Singular Value Decomposition. *J. Appl. Crystallogr.* **2003**, *36*, 86–95.

(41) Thompson, P.; Cox, D. E.; Hastings, J. B. Rietveld Refinement of Debye-Scherrer Synchrotron X-Ray Data from Al_2O_3. *J. Appl. Crystallogr.* **1987**, *20*, 79–83.

(42) Finger, L. W.; Cox, D. E.; Jephcoat, A. P. A Correction for Powder Diffraction Peak Asymmetry due to Axial Divergence. *J. Appl. Crystallogr.* **1994**, *27*, 892–900.

(43) Campbell, B. J.; Evans, J. S. O.; Perselli, F.; Stokes, H. T. Rietveld Refinement of Structural Distortion-Mode Amplitudes. *Ed. Newsl. No 8* **2007**, 81.

(44) Campbell, B. J.; Stokes, H. T.; Tanner, D. E.; Hatch, D. M. ISODISPLACE: A Web-Based Tool for Exploring Structural Distortions. *J. Appl. Crystallogr.* **2006**, *39*, 607–614.

(45) Dinnebier, R.; Müller, M. Modern Rietveld Refinement, a Practical Guide. *Mod. Diffr. Methods* **2012**, 27–60.

(46) Ravel, B.; Newville, M. ATHENA , ARTEMIS , HEPHAESTUS : Data Analysis for X-Ray Absorption Spectroscopy Using IFEFFIT. *J. Synchrotron Radiat.* **2005**, *12*, 537–541.

(47) Newville, M. IFEFFIT : Interactive XAFS Analysis and FEFF Fitting. *J. Synchrotron Radiat.* **2001**, *8*, 322–324.

(48) Rehr, J. J.; Kas, J. J.; Prange, M. P.; Sorini, A. P.; Takimoto, Y.; Vila, F. Ab Initio Theory and Calculations of X-Ray Spectra. *Comptes Rendus Phys.* **2009**, *10*, 548–559.

(49) Hedin, L.; Lundqvist, B. I. Explicit Local Exchange-Correlation Potentials. *J. Phys. C Solid State Phys.* **1971**, *4*, 2064.

Supplementary information

Estimate of Co concentration in α-Cr_2O_3/α-$Co_xCr_{2-x}O_y$ core-shell NPs. The size of our α-Cr_2O_3/α-$Co_xCr_{2-x}O_y$ nanoparticles was found to be ~52 nm with a shell size of about 6 nm from the TEM and XRD measurements. Given that the core shell nanoparticles have the following approximate dimensions as illustrated in Figure S1.1: R = 26 nm, r_2 = 20 nm (6 nm shell), and $r_1 \approx$ 16 nm, where I approximate ~10 nm sampling depth for XPS.

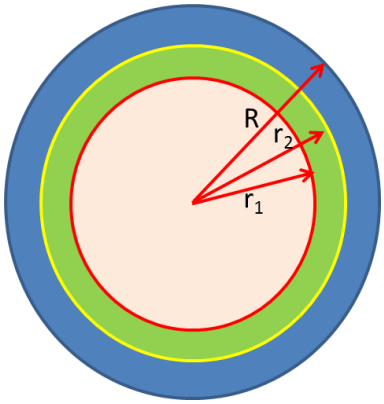

Figure S1.1. A simple schematic of a α-Cr_2O_3/α-$Co_xCr_{2-x}O_y$ core-shell nanoparticle; r_1 indicates the radius defining the XPS sampling volume, r_2 the radius defining the core and R that of the entire nanoparticle.

Let the fraction of the volume of the shell vs the XPS sampling volume be represented by z = (volume of shell)/(sampling volume) ≈ 0.7. From the XPS survey scan, the atomic percentage of the elements were found to be as follows: Co:Cr:(O+OH) = 5:28:67. If I exclude the contribution from OH^-, for stoichiometric chromate phase turns out to have Co:Cr:O = 5:28:49.5. Normalization of the contribution from the three elements gives ratios of Co:Cr:O = 6:34:60.

Using the following expression to find the concentration x in sampling volume:

$(1-z)\bullet[Cr_2O_3] + z\bullet[Co_xCr_{2-x}O_3]$

We can write,

$0.06[Co] + 0.34[Cr] + 0.6[O] = 0.3\bullet\{0.4[Cr] + 0.6[O]\} + 0.7\bullet\{y[Co] + (0.4-y)[Cr] + 0.6[O]\}$

Which yields, $0.06[Co] + 0.34[Cr] = 0.4[Cr] + 0.7\bullet y([Co]-[Cr])$, so that y = 0.086. Thus, since by stoichiometry $x = 5\bullet y = 0.43$, we get $Co_{0.43}Cr_{1.57}O_{2.9}$ for the alloyed phase in the shell.

Scanning electron microscopy. The scanning electron microscopy (SEM) imaging and energy-dispersive x-ray spectroscopy (EDX) measurements were made on the untreated Cr_2O_3 NPs using an FEI Quanta 200, operating at 20 kV. The powder Cr_2O_3 NPs were spread on a conducting carbon tape under the SEM. Due to charging effects on the oxide surface, some of the nanoparticles tend to aggregate into bigger clumps as shown in Figure S1.2. Although not very conclusive, a uniform size distribution of the particles can be observed in the SEM images. EDX analysis, shown in Figure S1.2, confirms the elemental composition of the sample as Cr and O. A small contribution from the carbon in the conductive tape can also be observed in the EDS data.

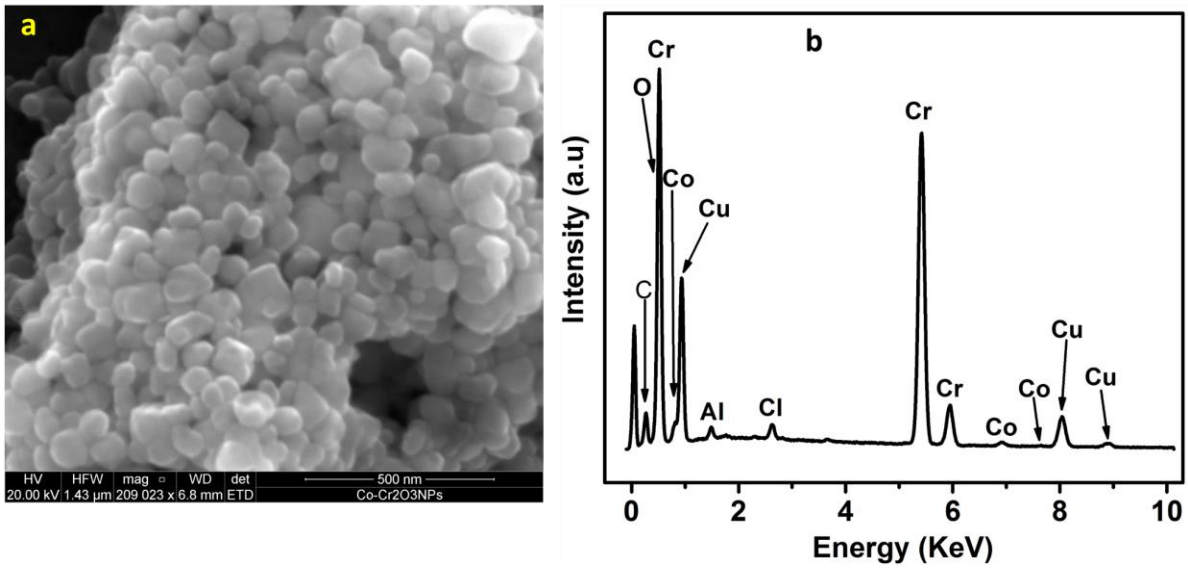

Figure S 1.2. (a) An SEM image and (b) SEM-EDX data of the α-Cr_2O_3/α-$Co_{0.43}Cr_{1.57}O_{2.9}$ core-shell nanoparticles (CSNs).

Transmission electron microscopy.

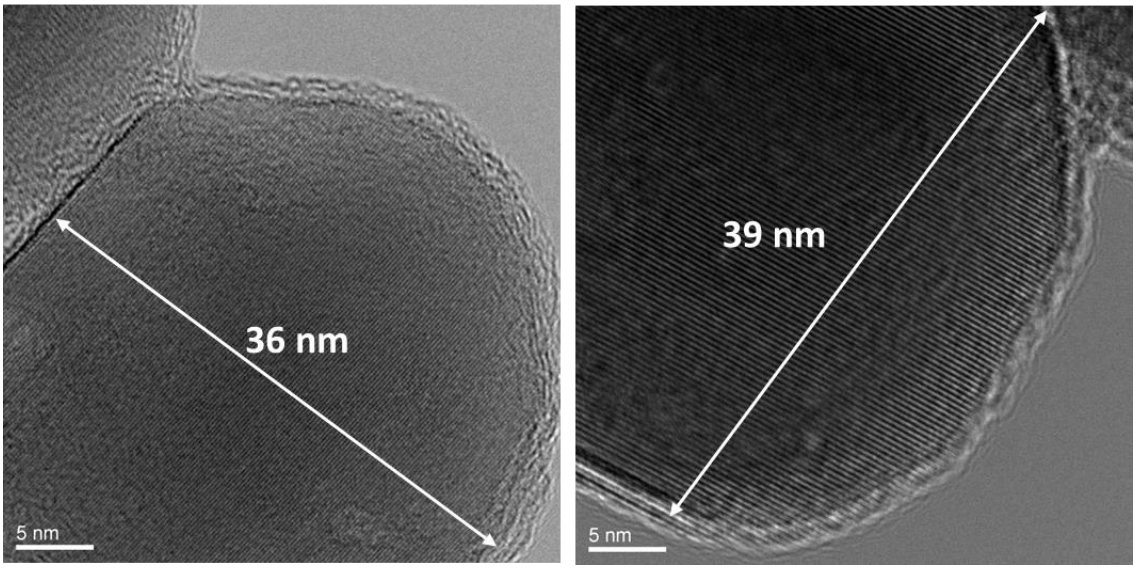

Figure S 1.3. HR-TEM images of individual α-Cr_2O_3 NPs. The approximate diameters of the nanoparticles are indicated in the images.

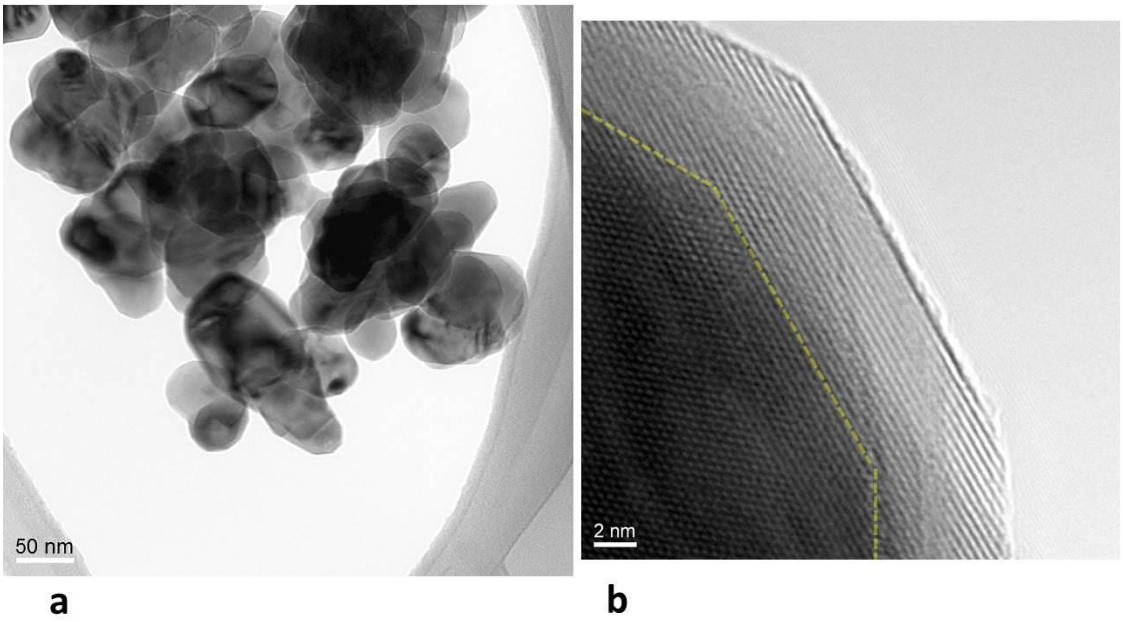

Figure S1.4. a) A HR-TEM image of agglomerated α-Cr_2O_3/α-$Co_{0.43}Cr_{1.57}O_{2.9}$ CSNs and b) a HR-TEM image of an individual α-Cr_2O_3/α-$Co_{0.43}Cr_{1.57}O_{2.9}$ CSN separate from one shown in Figure 1. The approximate dimensions of the nanoparticles (NPs) are indicated in the image in a). The agglomeration of the NPs results from the magnetic interactions between the individual nanoparticles. The yellow dashed line in b) indicates the location of the interface between the core (darker region) and shell (lighter, peripheral) region of the NP.

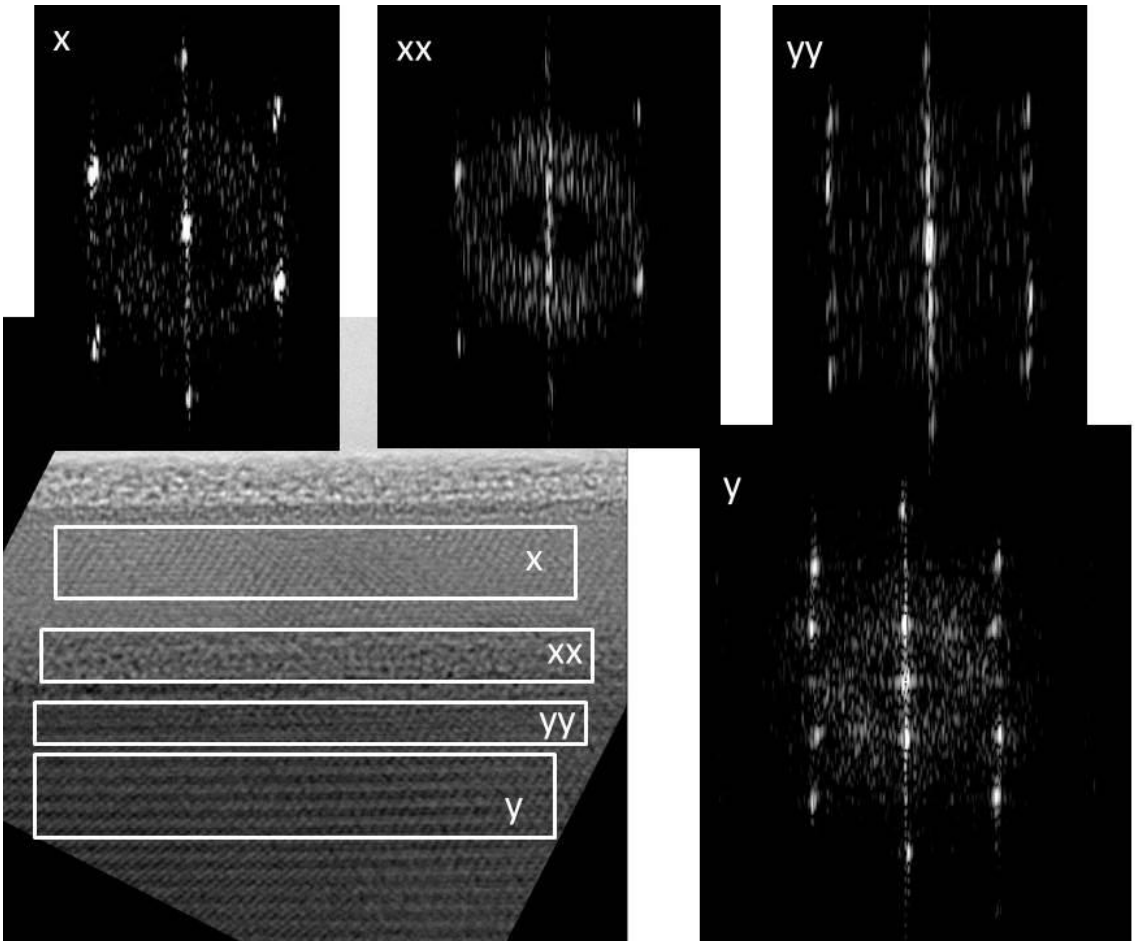

Figure S1.5. An HR-TEM image of a single α-Cr_2O_3/α-$Co_{0.43}Cr_{1.57}O_{2.9}$ core-shell nanoparticle shown in Figure 1.1 but rotated and the FFT's of the respective regions shown in the outlines on the image; region y is well in the core whereas yy is in the core and near the interface; region x is well in the shell whereas xx is in the shell but near the interface. The FFT's of the various regions indicate that core-shell nanoparticle is crystalline throughout.

X-ray diffraction.

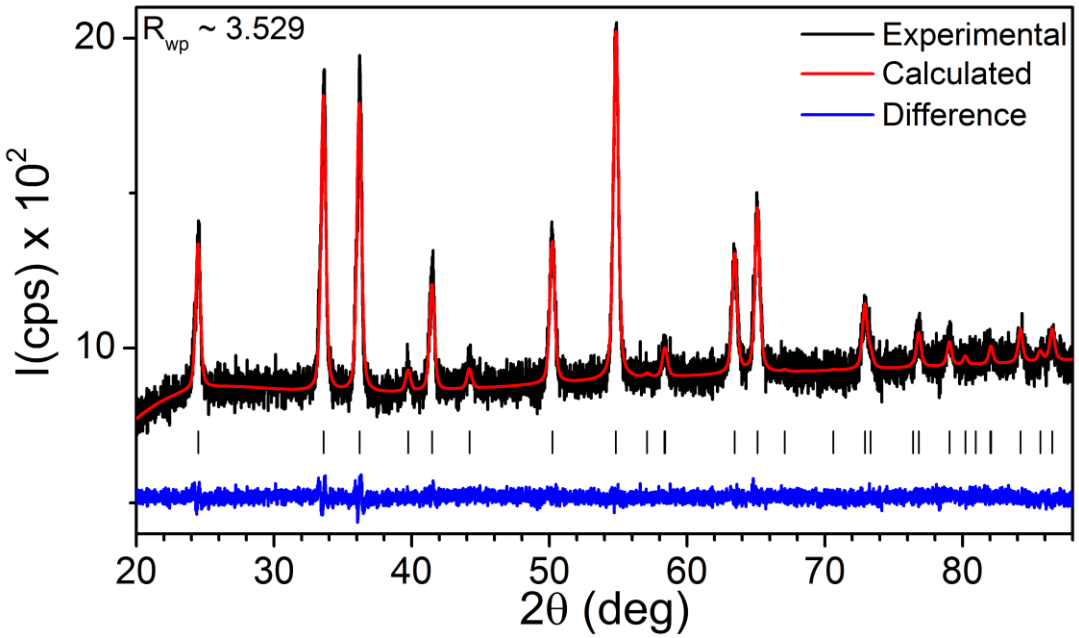

Figure S1.6. Plot of XRD data and the Rietveld refinement of the structure of the α-Cr_2O_3 NPs prior to HNE treatment. The structure conforms well to a corundum structure (space group #167: $R\bar{3}c$).

Table S1.1. Summary of structural results obtained from Rietveld refinement for α-Cr_2O_3/α-$Co_{0.43}Cr_{1.57}O_{2.9}$ inverted CSNs.

Core: α-Cr_2O_3 NPs (SG #167: $R\bar{3}c$); a = b = 4.959(2) Å; c = 13.598(7) Å ; V = 289.6(2) Å^3; core size = 39(2) nm					
Atoms	x	y	z	Site occupancy	B (Å^2)
Cr	0	0	0.347(2)	1.0	2.9
O	0.306(1)	0	1/4	1.0	1.1
Shell: α-$Co_xCr_{2-x}O_y$ (x=0.4; y=2.9) (SG #167: $R\bar{3}c$); a = b = 4.974(3) Å; c = 13.639(7) Å ; V = 292.2(4) Å^3; core-shell size = 52(4) nm					
Co	0	0	0.347(31)	0.20	2.9
Cr	0	0	0.347(31)	0.80	2.9
O	0.306(1)	0	1/4	0.97	1.1

X-ray photoemission spectroscopy.

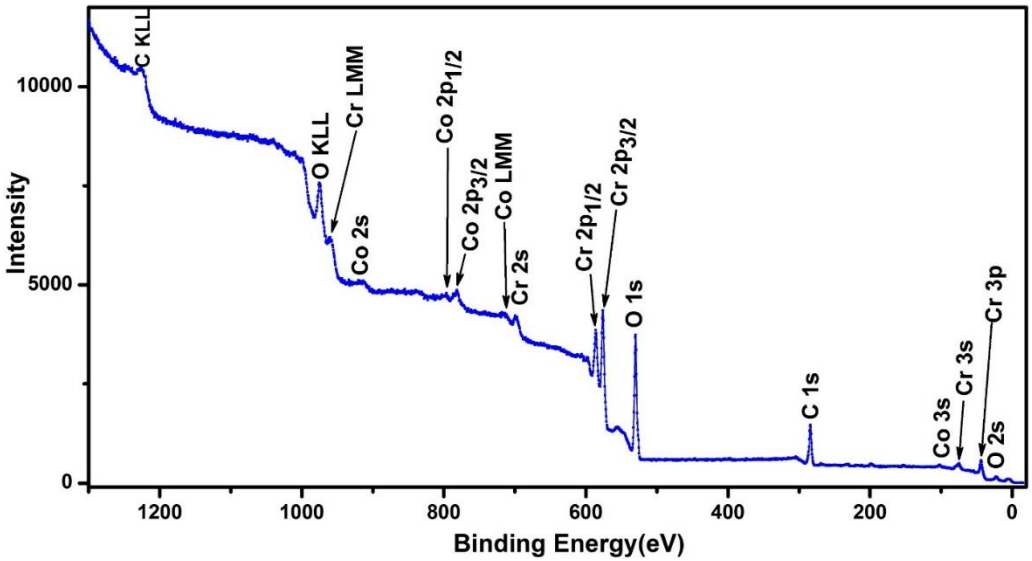

Figure S1.7. An XPS survey scan of the core-shell α-Cr_2O_3/α-$Co_xCr_{2-x}O_y$ NPs.

Table-S1.2. Summary of the XPS survey scan measured from the α-Cr_2O_3/α-$Co_xCr_{2-x}O_y$ inverted core-shell NPs. For elemental quantification, the $Cr2p_{3/2}$, O1s and $Co2p_{3/2}$ were analyzed using a Shirley background in their respective regions.

Name	Position	FWHM	Area	Atomic%
$Cr2p_{3/2}$	576.76	3.88	17399.13	27.64
O1s	530.76	3.315	10662.16	67.65
$Co2p_{3/2}$	782.26	8.541	4864.78	4.71

Table-S1.3. Summary of fitting results of the high-resolution XPS spectra measured from the α-Cr_2O_3/α-$Co_{0.43}Cr_{1.57}O_{2.9}$ inverted CSNs. GL(30) represents Gaussian-Lorentzian product formula where the percentage of Lorentzian peak shape is indicated in the parenthesis; LA(a,b,c) represents asymmetric line-shapes (controlled using the a,b and c parameters) based on the Lorentzian functional form convoluted with a Gaussian. The standard deviation of peak areas calculated from 400 individual spectra was generated by Monte Carlo simulation-assisted peak analyses utilized within the CasaXPS software.

$Cr2p_{3/2}$		Position	FWHM	Line Shape	Area	%Area	St. Dev
Cr-O	Peak-1	573.06	2	GL(30)	254.91	10.65	0.029
	Peak-2	574.81	1.9	GL(30)	438.70	18.32	0.0263
	Peak-3	576.04	2	GL(30)	941.89	39.34	0.0488
	Peak-4	578.51	2	GL(30)	139.67	5.83	0.0478
Cr-OH		577.22	2	GL(30)	619.09	25.86	0.0380
O1s							
Co-O		529.16	1	LA(4.2,2,12)	70	3.35	0.02
Cr-O		529.84	1.55	LA(4.2,2,12)	988	48	0.01
Cr-OH		530.70	1.55	LA(2,4.2,12)	790	38.28	0.047
Co-OH		531.60	2.2	GL(30)	217.33	10.55	0.014
$Co2p_{3/2}$							
Co-O		780.16	5	GL(30)	127.62	22.97	0.16
Co-OH		781.58	4.75	GL(30)	253.54	45.63	0.17
Satellite		787.24	5	GL(30)	174.52	31.41	0.089

Magnetic measurements. The magnetic hysteresis measurements, both in zero field cooled (ZFC) and field cooled (FC) mode, were made using a Quantum Design SQUID **MPMS/XL** magnetometer from a temperature range of 5K-300K and in a field of ± 50 kOe. A nanoparticle sample weighing 30 mg was loaded inside a softgel capsule

and subsequently placed inside the magnetometer for magnetic measurements. For the FC measurements, the field cooling was made using a field of 15000 Oe upon cooling from 330 K to 5 K. Both the FC and ZFC magnetization vs field measurements were made at 5 K.

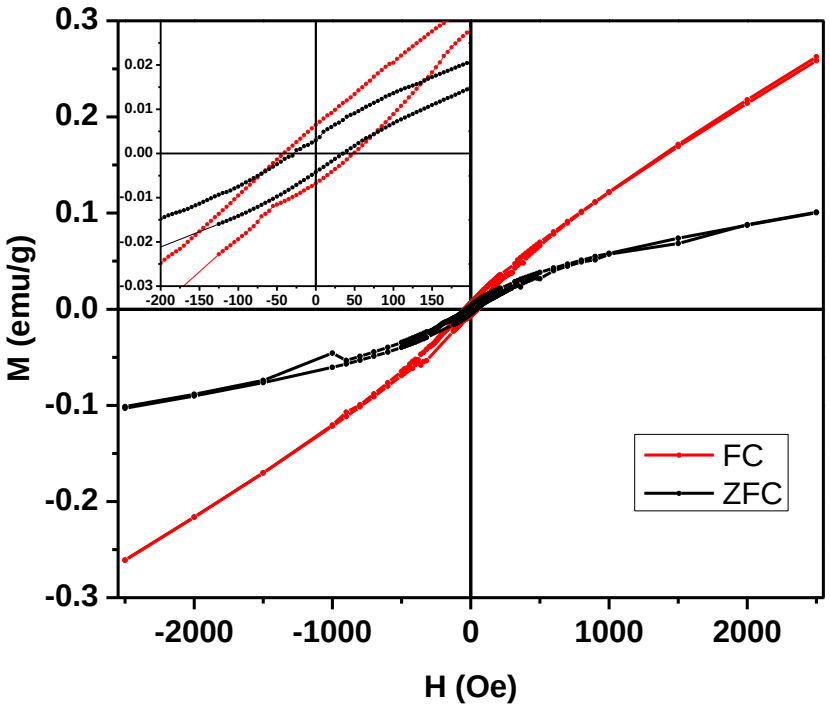

Figure S1.8. Zero field cooled (ZFC) and field cooled (FC) hysteresis loops, i.e., magnetization vs applied magnetic field H, measured from the core-shell α-Cr_2O_3/α-$Co_xCr_{2-x}O_y$ NPs. The inset shows the hysteresis loop shift for the FC vs ZFC measurements.

UNIQUE CHROMIA-BASED CORE-SHELL NANOPARTICLES: SYNTHESIS, CHARACTERIZATION AND FIRST-PRINCIPLES CALCULATIONS

Abstract

Novel chromia based core-shell nanoparticles have been synthesized using hydrothermal nanophase epitaxy (HNE) technique. The highly-uniform structured α-Cr_2O_3@α-$Ni_{0.58}Cr_{1.42}O_{2.88}$ inverted core-shell nanoparticles exhibit epitaxial growth across a sharp interface having minimal strain and roughness. The HNE technique allows for synthesis of a unique corundum-structured nickel(II)-chromium-oxide ($Ni_{0.58}Cr_{1.42}O_{2.88}$) nanophase shell covering the α-Cr_2O_3 core of the nanoparticles. XPS analysis confirms the +2 oxidation state of Ni in the core-shell nanoparticles. Magnetic measurements reveal a coercivity shift of 100 Oe between the zero field and field cooled hysteresis loops, indicating a substantial exchange bias effect between the antiferromagnetic α-Cr_2O_3 core and the ferromagnetic α-$Ni_{0.58}Cr_{1.42}O_{2.88}$ shell. My first principles calculations show that Ni(II) substitution for Cr(III) and formation of the α-$Ni_{0.58}Cr_{1.42}O_{2.88}$ nanophase results in an overall equilibrium spin configuration having net ferromagnetic ordering within the shell of the nanoparticles. My study demonstrates that the HNE technique is useful for synthesis of unique, highly ordered core-shell nanoparticles having enhanced magnetic properties.

Text

A high degree of tunability of the magnetic and catalytic properties of nanomaterials for anticipated technological applications is still a major challenge. Due to

their composite nature, core-shell nanoparticles (CSNs) show considerable promise for active control of their physicochemical properties through the adjustment of core and shell size, morphology, chemical content, and structure at the atomic scale. In addition, their composite nature often adds multifunctionality to CSNs, leading to a wide variety of potential applications, including in energy storage and harvesting, hetero- and photocatalysis, magnetic devices, photonics, and biomedicine.[1–6] In particular, magnetic core-shell nanoparticles are currently attracting considerable attention because their enhanced magnetic properties are highly promising for potential applications in magnetic random access memory and spintronic devices, cell separation, tissue engineering, drug delivery, MRI targeted-cell imaging, and hyperthermia.[7-9] Conventional magnetic CSNs have a ferromagnetic (FM) core and an antiferromagnetic (AFM) or ferrimagnetic (FiM) shell whereas inverted core-shell nanoparticles have an AFM core and an FM or FiM shell. The distinct magnetic phases in the core vs the shell regions interact via the exchange bias effect.[10–12] The exchange bias is owed to the exchange anisotropy at the interface between the coupled magnetic phases of the core and shell. The inverted CSNs are particularly promising because their magnetic properties are more easily controlled, by having well-ordered AFM cores, resulting in magnetic structures having large coercivities, tunable blocking temperatures and other enhanced magnetic effects.[13,14] Inverted CSNs are typically composed of the core and shell having distinct structural phases. The structural phase difference of the core vs shell usually results in considerable structural disorder, defect formation (e.g., cation and/or anion vacancies), amorphization and roughness at the interface between the core and shell. The disorder, defects, roughness and extent of the interface can have a strong but as yet not fully understood

effect on the nature and extent of the exchange bias in CSNs. Disordered interfaces are thought to result in strong spin anisotropy or spin-glass type regions in core-shell NPs. Monte Carlo simulations show that the presence of vacancies[15] and roughness[16] at the interface degrades the exchange bias whereas other calculations[17] show that the magnitude of the exchange bias field is strongly coupled to the degree of interface roughness in FM-AFM core-shell nanoparticles. Progress in this area of nanoscience is complicated by the lack of atomic-scale control on the level of defects, roughness and disorder at the interface of two-phase CSNs.

I have recently developed a novel nature-inspired hydrothermal nanophase epitaxy (HNE) method for synthesis of highly ordered AFM core and a FM/FiM shell Cr_2O_3 – based CSNs.[18] By imitating mineral zonation that occurs naturally under hydrothermal conditions,[19] we are able to grow an epitaxial highly structurally ordered α-$M_xCr_{2-x}O_{3-y}$ shell (M: Co, Fe, Ni) covering a α-Cr_2O_3 nanocrystalline core to form α-Cr_2O_3@α-$M_xCr_{2-x}O_{3-y}$ inverted CSNs. In this work, I describe my synthesis, experimental characterization and first principles calculations used to investigate α-Cr_2O_3@α-$Ni_{0.58}Cr_{1.42}O_{2.88}$ inverted CSNs. The HNE synthesis results in the formation of α-Cr_2O_3@α-$Ni_{0.58}Cr_{1.42}O_{2.88}$ CSNs having a sharp, well-ordered core/shell interface, creating an ideal nano-scale environment for spin exchange bias effects, as evidenced in magnetization measurements. Furthermore, this is a first report of a unique α-$Ni(II)_xCr_{2-x}O_{3-y}$ (nano)phase. My SQUID magnetometry measurements show a substantial exchange bias effect between the AFM core and FM shell of the CSNs. The substitution of divalent Ni(II) for trivalent Cr(III) results in a nanomaterial having purposely introduced oxygen vacancies in the shell region of the CSNs. My first principles calculations confirm that

the α-$Ni_{0.58}Cr_{1.42}O_{2.88}$ shell nanophase is ferromagnetic and that intentional substitution of Ni^{2+} instead of Ni^{3+} results in stronger magnetic properties of the CSNs. This is important for development of nanomaterials having enhanced magnetic, catalytic and other physicochemical properties that are targeted for multifunctionality, such as for energy and magnetic device applications.

The Cr_2O_3 nanoparticles (NPs) used in this study were synthesized following the procedure outlined in Farzaneh et al.[20] Commercially available $Cr(NO_3)_3 \cdot 9H_2O$ (Sigma-Aldrich) powder was used for making a 0.2 M aqueous solution of chromium nitrate which then mixed with an organic surfactant Triethanolamine (TEOA) in 1:2 molar ratio. HPLC water was deoxygenated by passing dry nitrogen gas through it while maintaining the temperature at ~60 °C. The solution was magnetically stirred for 1 hour and irradiated in a microwave oven for 5 minutes. Subsequently, the solution was left on top of a magnet for ~6 hours whereupon a dark-green colored precipitate formed at the bottom of the beaker. The precipitate was separated from the solution and then dried in air. Next, the precipitate was calcined in air by heating at a rate of 10 °C/min to 575 °C, maintained at 575 °C for 2 hours, and finally cooled to room temperature at 10 °C/min. The sample turned into a green-colored fine powder at the conclusion of the calcination process. For shell overgrowth and CSN synthesis, a 0.05M solution (pH = 6.5) was first prepared from commercially available $NiCl_2$ by using deoxygenated HPLC water. Next 0.2997g of Cr_2O_3 nanoparticles (NPs) were added to the solution and sonicated for ~20 minutes and then loaded into a Teflon-insert autoclave. The nanoparticle/$NiCl_2$ solution was hydrothermally treated for ~13 hours at a temperature of 210 °C. Subsequently, the solution was transferred to a beaker and placed on top of a magnet for an extended period

of time to allow for the NPs to be fully precipitated out of solution. After air drying, the nanoparticle sample was calcined at 500 °C for ~2 hours: the heating and cooling rate were set at 10 °C/min. The magnetic measurements were made using a SQUID magnetometer from Quantum Design (MPMS/XL) used from a temperature range of 5K-330K and in a field of ±5 kOe. A quantity of 40 mg of sample was placed in a gelatin capsule, which was positioned within the SQUID and inside the low temperature vessel of the instrument for the magnetic measurements. The field cooling for the magnetic hysteresis curve measurements, which were made at 5 K, was accomplished starting from 330 K to below the Néel temperature of the sample in a field of (20 kOe). In the case of field cooled (FC) magnetization measurements vs temperature, the sample was cooled in a field of 500 Oe starting from 330 K.

The first principles calculations were made using the Local Spin Density approximation method[21] (LSDA) implemented in Quantum Espresso.[22] A rhombohedral primitive unit cell[23] with a space group $R\bar{3}cH$ (ICSD 173470) was used in the initial self-consistent field calculation of Cr_2O_3. To find the equilibrium ground state and the corresponding magnetic configuration of α-Cr_2O_3, the FM, AFM and nonmagnetic (NM) systems were considered. The +-+- alignment along the z-axis AFM spin configuration (out of several possibilities, such as ++--, +--+, etc.) calculation converged to the lowest energy. The Monkhorst-Pack scheme[24] based on the 4x4x4 k-point grid was employed for Brillouin-zone integral calculations. The cutoff energies for the plane wave and augmentation charge were 30 and 300 eV, respectively, and energy convergence was achieved with a value of 0.0979610 μeV by setting the atomic energy convergence to $1x10^{-8}$ eV. Density of states (DOS) and the projected density of states (PDOS) for the

relaxed structure were obtained by using the tetrahedron method with an 8x8x8 k-point grid mesh. For spin polarization calculations, LSDA+U, where U is the coulomb repulsion parameter, and local exchange interaction (J) were used in order to obtain results more consistent with experimentally derived values. The values of the U and J were adopted from Shi et al., who made first principles calculations of the magnetic properties of chromia.[25] For calculations of the Ni substituted α-Cr_2O_3 structures (α-$NiCr_3O_6$ 1x1x1 and α-$Ni_2Cr_6O_{12}$ 1x1x2 supercell), the U and J values were adopted from Cococcioni et. el.[26] and Perdew-Zunger[27], where exchange-correlational, norm conserving pseudopotentials were used for all the atoms. The α-$Ni_xCr_{2-x}O_3$ structures were initially relaxed for energy minimization and the relaxed structural parameters were used in subsequent calculations. The relaxed structural parameters were obtained until all the forces were less than $1x10^{-3}$ eV/a.u. As for chromia, all spin configurations (i.e., ++--, +--+, etc.) were tested in the calculations in order to find convergence to the lowest energy configuration. Electron localization function[28,29] images were generated by using the visualization software Vesta.[30]

Transmission electron microscopy (TEM) analysis (see SI) shows that the majority of the nanoparticles (NPs) manifest in quasi-spherical or nanocrystalline shape with an average particle size of ~57(3) nm. This is in very good agreement with a nanoparticle size of 58(2) determined using the Scherrer equation and (integral breadth method) Rietveld refinement of XRD data (see SI). The HRTEM image presented in Fig. 2.1a clearly shows the core-shell structure of the α-Cr_2O_3@α-$Ni_xCr_{2-x}O_3$ nanoparticle.

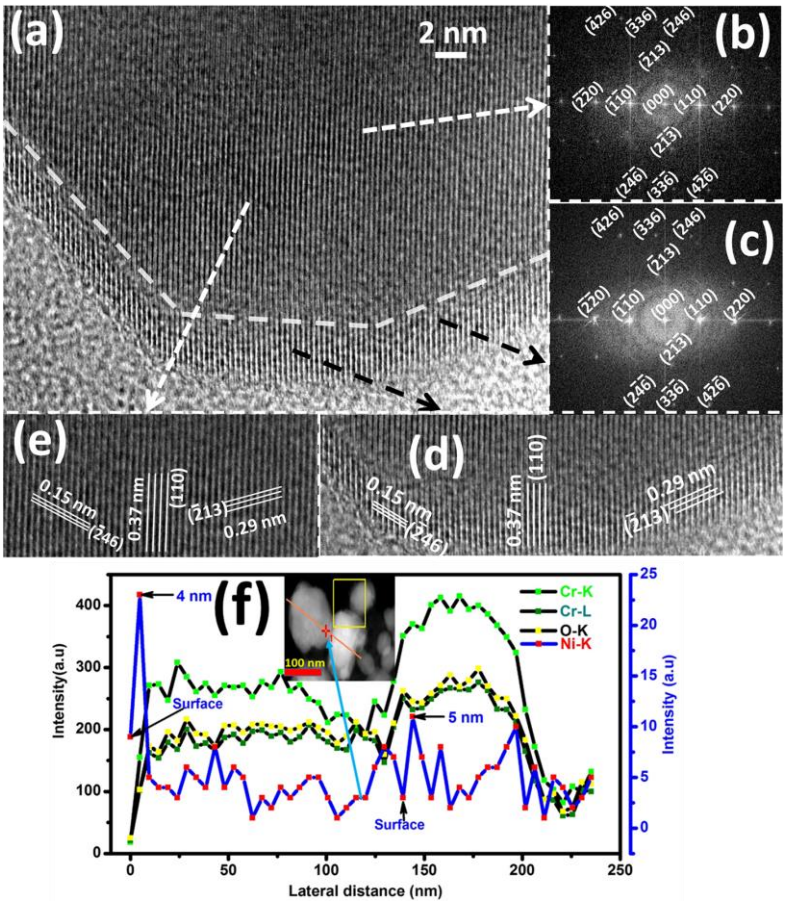

Fig: 2.1 a) An HRTEM image showing the core-shell structure of a α-Cr_2O_3@α-$Ni_{0.58}Cr_{1.42}O_{2.88}$ nanoparticle; b) FFT of core and the c) FFT of shell of the CSN; several atomic planes and corresponding d-spacings between the planes in the d) shell the same atomic planes (as in Core) and corresponding d-spacings between the planes in the e) core; f) TEM-EDX elemental line profile of two side-by-side nanoparticles.

A slight discontinuity (potentially due to oxygen and/or cation vacancies) and change in contrast is observed approximately 5 nm from the surface, delineating the shell from the core region of the CSN. The FFTs generated from the core and shell part of the nanoparticle (Figs. 2.1 b and c) are highly similar, indicating continuity in the crystal planes across the interface between the two regions. Similar atomic planes and the corresponding d spacing of those planes in the core and shell shown in Fig 2.1.d and e, the indexing of the atomic planes are fully consistent with the corundum structure having

$R\bar{3}c$ (ICSD#173470) space group symmetry. Line profile analysis (Fig. 2.1f) shows that whereas the Cr and O are uniformly distributed, the Ni distribution is dominant in the surface (i.e., shell) regions, at up to ~5 nm inside of the nanoparticles. The TEM results are consistent with the Rietveld refinement analysis of the XRD data, which shows that the CSNs are rhombohedral having the $R\bar{3}c$ space group. Elemental analyses made from XPS and from Rietveld refinement of the XRD data indicate that the nanophase of the shell has an approximate stoichiometry formula given by $Ni_{0.58}Cr_{1.42}O_{2.88}$. Analysis of the Ni $2p_{3/2}$ peak, i.e., from the Ni-O bonding component at 854.30 eV, shows that Ni is in the +2 oxidation state in the α-Cr_2O_3@α-$Ni_{0.58}Cr_{1.42}O_{2.88}$ CSNs; the contribution at 855.30 eV corresponds to Ni-OH bonding (see SI). My results indicate that Ni(II) is incorporated substitutionally for Cr(III) in the CSNs. A small substoichiometry with respect to oxygen content is expected, in order to maintain charge balance upon substitution of Ni^{2+} for the Cr^{3+} ion in the shell region of the CSNs.

Fig 2.2a shows zero field cooled (ZFC) and field cooled (FC) magnetic hysteresis measurements measured in a magnetic field ranging from ±5 kOe. The FC or ZFC hysteresis curves do not reach saturation at up to ± 50 KOe (not shown here). In case of the FC measurements, the magnetization (M) vs applied field (H) curve is vertically shifted in the magnetization axis and the entire hysteresis loop is shifted (shown in inset) in the negative field direction due to the exchange bias between the shell and the core of the nanoparticles. This is consistent with the hysteresis loop behavior exhibited by inverted CSNs. The value of the exchange bias field, as defined using $H_{EB} = |(H^+ + H^-)/2$[31–33], where H^+ and H^- are the coercive fields for ascending and descending curves, respectively, is 96 Oe.

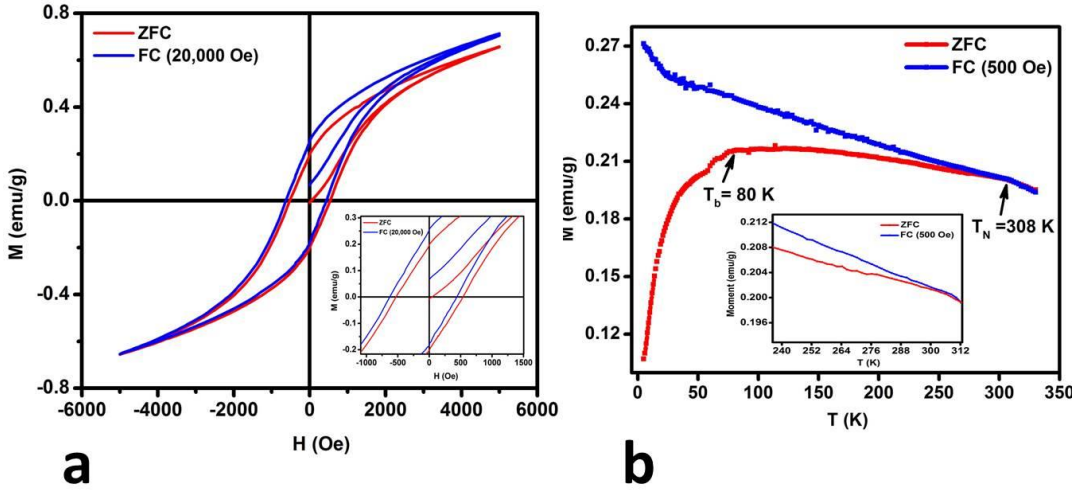

Fig. 2.2 a) Magnetization hysteresis curves measured from α-Cr_2O_3@α-$Ni_{0.58}Cr_{1.42}O_{2.88}$ CSNs at 5 K in the zero field cooled (ZFC) and field cooled (FC) at 20 KOe. The inset shows the shift between the FC and ZFC curves due to the exchange bias effect in the region of the hysteresis loops near zero applied field. b) The ZFC and FC magnetization as a function of temperature measured from α-Cr_2O_3@α-$Ni_{0.58}Cr_{1.42}O_{2.88}$ CSNs at 500 Oe. The inset on the left shows the region of the graph close to the bifurcation temperature (311 K).

This is consistent with an FM character of the shell and an AFM character of the core of the NPs.[14] The relatively large value of coercivity ($H_C = |(H^+ - H^-)|/2$ = 533 Oe) is consistent for both the ZFC and FC hysteresis loops. Fig. 2.2b) shows the magnetization with respect to temperature measured from 5 to 330 K in the ZFC and FC condition in a field of 500 Oe. The ZFC and FC curves start to deviate from one another at a bifurcation temperature of 311 K. The ZFC curve shows a maximum at a temperature of 81K which is defined as the blocking temperature T_b of the sample. The Néel temperature (T_N) of the AFM α-Cr_2O_3 core of nanoparticles is found to be 308 K, as determined from the kink in that region of the ZFC curve. This value is slightly higher than the reported value of 302 K for Cr_2O_3 nanoparticles (with dia. 50-70 nm)[34] and same as the value of 308 K reported for bulk Cr_2O_3[34]. The Curie temperature (T_C) of the shell region of the CSNs as

determined from the ZFC magnetization curve vs temperature is ~64 K (see Fig. 2.2). The fact that T_C value is considerably lower than the T_N value indicates that CSNs are doubly inverted. This provides for interesting magnetic properties, such as persistence of magnetization above T_C, which has been attributed to the magnetic proximity effect in CSNs,[13] where the AFM core influences the ordering of the FM shell through exchange interactions. However, it should be noted that the magnetic proximity effect in inverted CSNs has not yet been fully verified.

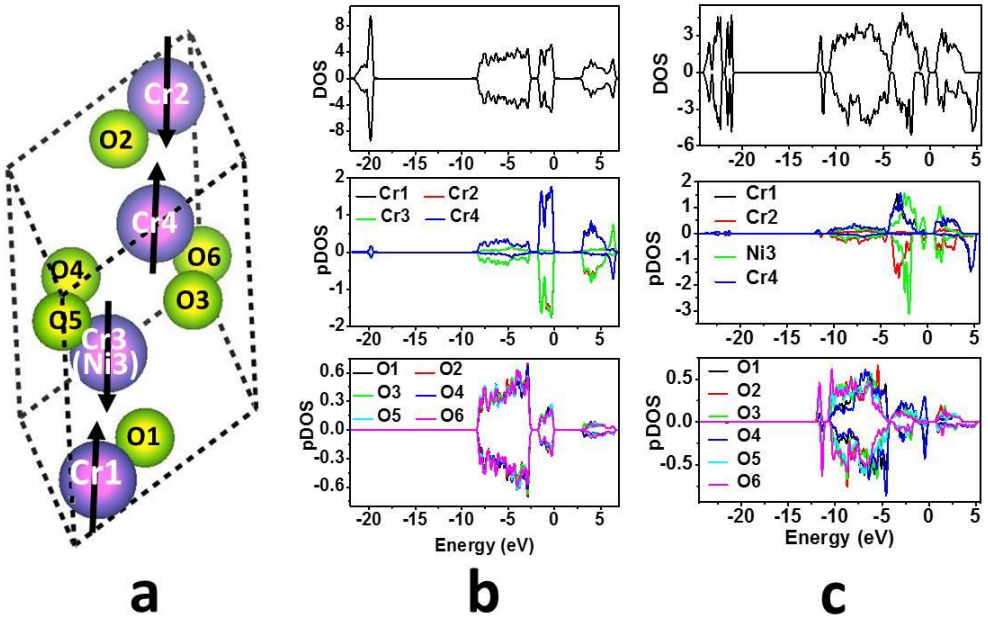

Figure 2.3. a) The primitive rhombohedral unit 1x1x1 cell used in the ab initio calculations for chromia (α-Cr_2O_3) and for Ni-substituted chromia (α-$NiCr_3O_6$); the atomic positions are labeled. The density of states (DOS) and partial DOS (pDOS) calculated from first principles for b) chromia and c) for Ni(II)-substituted chromia.

I have made first principles calculations in order to shed further light onto the electronic and magnetic properties of unique α-$Ni(II)_xCr_{2-x}O_3$ nano-compound. DFT-based calculations were carried out on Ni^{3+} and Ni^{2+} substitutional ions in a cell, in order

to establish the effect of Ni(II) oxidation state on the magnetic properties of a α-$Ni_{0.5}Cr_{1.5}O_3$ compound. The calculation of the Ni(II)-substituted chromia was carried out by introducing a uniform background charge (equivalent to that on one electron) in the cell prior to optimization of the structure. The band gap energy for the Ni(III)-substituted chromia (α-Ni(III)Cr_3O_6) phase was determined from my first principles calculations to be 1.91 eV for up spin state and 2.4 eV for down spin state, as defined by the gap between Cr1/Ni3 t_{2g} sub-band contribution to the overall valence band (VB) and O 2p levels in the conduction band (CB).[35] This is a significantly smaller energy gap value than my calculated value of 3.15 eV for α-Cr_2O_3, which is in good agreement with the experimentally determined values (3.2 to 3.4).[36–38] Mu et al. in their theoretical calculation shows the effect of Ni(III&II) substitution (8%) on the band gap and EEL formation, my calculation with similar amount (8%) of substitution give the same types of DOS characteristics.[39] In Fig. 2.3 I show the partial DOS (pDOS) calculated for Ni(II)-substituted chromia (α-Ni(II)Cr_3O_6). The calculated band gap of 1.9 eV and 2.43 eV for up spin and down spin state respectively of α-Ni(II)Cr_3O_6 is similar to the Ni(III)-substituted chromia. The band gap narrowing in α-Ni(III&II)Cr_3O_6 is predominantly attributed to Ni3 and Cr1 3d t_{2g} (see Fig. 2.3) contributions to the pDOS, which shift the top of the valence band ~1.2 eV higher in energy relative to the value in α-Cr_2O_3 in the up spin state and 0.7 eV in down spin state. UV-Vis absorption measurements yield an optical band gap of 2.5(1) eV for the α-Cr_2O_3@α-$Ni_{0.58}Cr_{1.42}O_{2.88}$ CSNs (see SI). This value is in good agreement with my LSDA+U calculations showing that the band gap between the minority upper valence band and lower conduction band DOS is 2.4 eV. In addition, there is a significant impurity-like level 3d e_g contribution predominantly from

Ni3 with minor contributions from Cr2 to a DOS projection in the middle region of the gap. The impurity energy levels (IELs), which stem from hybridization of predominantly delocalized Ni 3d states with O 2p states, are predicted to result in acceptor- (from the VB maximum to the IELs) and donor-like (from the IELs to the CB minimum) optical transitions. (Mu et al. From my self-consistent field calculations I find that the magnetic moment of each Cr in α-Cr_2O_3 is 3.11 μ_B, which is in good agreement with the experimental value of 2.76 μ_B[40] and theoretical value of 3 μ_B. Similar calculations yield a net magnetic moment of 2.96 μ_B for α-Ni(II)Cr_3O_6 and 2.01 μ_B for α-Ni(III)Cr_3O_6: The individual magnetic moments were found to be +0.12 μ_B for Ni(II)3 and -0.58 μ_B for Ni(III) substitutional ions in nickel-chromia (see Table S2.3 in SI for individual magnetic moment values). The marked reduction in the magnetic moment of Ni, in comparison to previously determined theoretical values 1.64 μ_B in metallic nickel particles[24,41] and 1.9 μ_B in $Mn_xNi_{1-x}O$[25,42], is attributed to strong hybridization (within the valence band) of the Ni 3d levels and O 2p levels of the surrounding oxygen atoms. Formally, in the high spin state (in octahedral coordination), Ni^{2+} has 6 paired electrons in the 3d t_{2g} levels and 2 unpaired electrons in the 3d e_g levels. In my case, the electrons in the Ni^{2+} 3d e_g levels near the top of the VB are paired, as evidenced in the cancelation of the spin-up and spin-down Ni3 e_g-contributions to the pDOS (see Fig. 2.3). My calculations show that the overall magnetic moment results predominantly from the majority spin (3d t_{2g}) state contribution due to Cr1, whereas the moments due to Cr2 and Cr4 cancel one another. Thus, the equilibrium magnetic structure that emerges from my calculations for α-Ni(II)Cr_3O_6 is one in which Ni and Cr ions are ferromagnetically ordered within alternating (0001) honeycomb buckled planes in the corundum lattice: The intervening

(0001) planes have the standard AFM ordering of Cr spins. Alternatively, my calculations predict that the α-Ni(III)Cr_3O_6 compound has smaller down spin Ni^{3+} and larger up spin Cr resulting in FiM ordering within alternating (0001) honeycomb buckled planes in the corundum lattice. Thus, according to my calculations, for identical sizes of core vs shell, α-Cr_2O_3@α-$Ni_{0.5}Cr_{1.5}O_3$ CSNs having Ni^{2+} should exhibit more substantial magnetization effects (e.g., coercivity) than for ones having Ni^{3+} ions.

I have carried out a Bader charge analysis of α-Cr_2O_3 and α-$NiCr_3O_6$ using a grid based algorithm to determine the charge on each individual atom in the crystalline lattice.[43,44] The charge is found to be -1.7e and +2.54e on each O and Cr, respectively, in α-Cr_2O_3 (e ≈ 1.6 x 10^{-19} C). We observe a significant disparity of charge between Ni and Cr (+0.95e and +2.50 to +2.55e, respectively), and a reduction in charge of individual oxygens by 0.24 to 0.32e compared to the values in α-Cr_2O_3, in α-Ni(III)Cr_3O_6 (see Table S2.4 in SI). In α-Ni(II)Cr_3O_6, Ni has a charge of +0.55e, and each of the Cr ions maintain a charge of approximately +2.5e whereas the charge of individual oxygens is reduced less (by 0.08 to 0.27e) compared to O values in α-Cr_2O_3 (see Table S2.4 in SI). The reduction of charge of substituted Ni^{3+} to +0.95e and Ni^{2+} to +0.55e, in α-Ni(III)Cr_3O_6 and α-Ni(II)Cr_3O_6, respectively, is consistent with the significant contributions from Ni 3d and O 2p states at the top of the VB and in the middle of the band gap. This implies that Ni incorporation in the structure results in an increase of covalent nature in the (Ni-O and Cr-O) chemical bonding in α-$NiCr_3O_6$ in case of either Ni^{3+} or Ni^{2+} substitution. I have also used the electron localization function (ELF) analysis,[28,29] which gives a direct spatial distribution of electrons surrounding the core or nucleus of the individual atoms, to provide information on bond character in α-$NiCr_3O_6$.

Fig. 2.4 shows the ELF plot for the α-Cr_2O_3 (Fig. 2.4b) and of the α-Ni(II)Cr_3O_6 (Fig. 2.4c) structures. As shown in the ELF plot in Fig 2.4, the extent of covalent bonding between Cr and surrounding O's in the α-Cr_2O_3 structure is less than for Ni – O and Cr – O in α-Ni(II)Cr_3O_6. The electron densities of the Cr and O atoms have nominal overlap and commensurate (partial) Cr – O covalent bonding in α-Cr_2O_3 but significantly greater Ni – O (e.g., O1 and O4) and Cr – O overlap (e.g., O3 and O5) and more substantial covalent bonding in α-Ni(II)Cr_3O_6. The increased covalency of the Ni – O bond compared to that of the Cr – O bond is consistent with greater degree of charge depletion and reduced magnetic moment on the substitutional Ni(II) ion in α-Ni(II)Cr_3O_6.

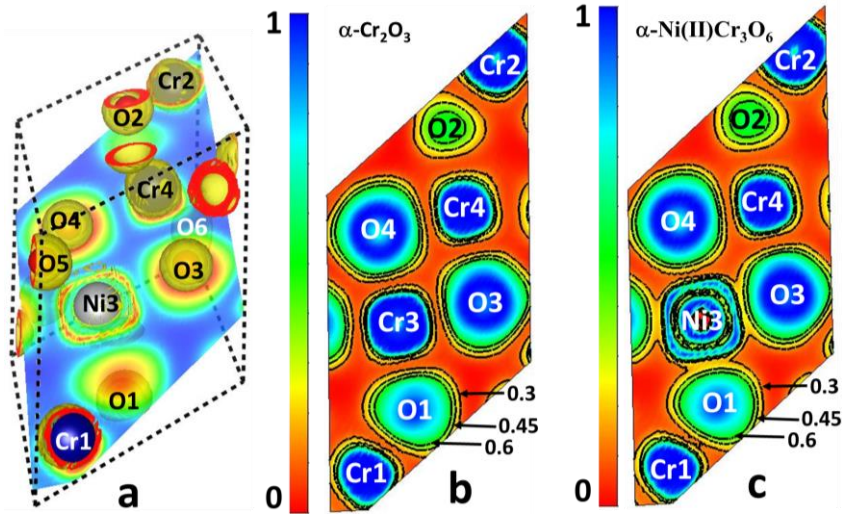

Figure 2.4. a) A three dimensional electron localization function (ELF) plot superimposed over the location of the atoms within the 1x1x1 primitive rhombohedral unit cell of the α-Ni(II)Cr_3O_6 structure. ELF contour diagram plots projected over the $(12\bar{1})$ plane (shown in a) for (b) α-Cr_2O_3 and (c) for α-Ni(II)Cr_3O_6 : the 0.30, 0.45, and 0.6 isosurface contours are indicated in the diagrams.

In order to test different site occupancies of substitutional Ni^{2+} in a nickel-chromia compound, first principles calculations have been carried out on a 20 atom 1x1x2 supercell α-$Ni(II)_2Cr_6O_{12}$ structure (i.e. a doubling of the Ni(II)-substituted

primitive unit cell). Several variations of starting positions and spin orientations for the two Ni atoms (with uniform background charge) were attempted, in order to determine the equilibrium spin structure, energy and overall magnetic moment of the α-$Ni(II)_2Cr_6O_{12}$ structure (see SI section for additional details). The most interesting of these occur for "side-by-side", i.e., all Ni^{2+} ions in the buckled honeycomb plane, and farthest-removed (0001) plane occupation (i.e., equivalent to 1 and 4 sites in the 1x1x1 cell) by individual Ni^{2+} ions. In either case, the equilibrium spin configuration coincides with net FM ordering and a net magnetization moment of -5.92 μ_B in the 1x1x2 cell. Thus, my calculations demonstrate that Ni^{2+} substitution for Cr^{3+} results in an overall FM spin configuration within a corundum structured α-$Ni_{0.58}Cr_{1.42}O_{2.88}$ shell of CSNs. Others have invoked surface and/or interface spin disorder effects[12] (e.g., spin glass layers) and the F-center exchange coupling (FCE)[45], which occurs by interaction of Ni^{2+}-V_O-Ni^{2+}, where V_O is the oxygen vacancy, as required mechanisms that result in FM/FiM ordering in the shell and are responsible for the exchange coupling of inverted CSNs. my calculations demonstrate that FM ordering in CSNs is not predicated upon surface/interface spin disorder and the FCE. Nevertheless, surface/interface spin disorder and FCE may provide additional sources of ferromagnetism in CSNs.

My first principles calculations indicate that α-$Ni(II)Cr_3O_6$ is thermodynamically stable. This enables synthesis of nanomaterials having enhanced physical and chemical properties that should be well suited for tailored, multifunctional applications (e.g., magnetic, photocatalysis, heterogenous catalysis, gas sensing, etc.). Whereas the magnetic CSNs synthesized in the past typically suffer from having a disordered and rough core-shell interface, my nanoparticles avoid this issue due to the hydrothermal

overgrowth mechanism used to synthesize the shell on the core of established nanoparticles. As TEM results show, the transition from core to the shell region of the nanoparticles is sharp and structurally continuous with minimal disorder. The sharp and continuous nature of the core-shell interface of the α-Cr_2O_3@α-$Ni_{0.58}Cr_{1.42}O_{2.88}$ CSNs impacts strongly upon the interface anisotropy and the exchange bias effect. As a result, the FM shell and the AFM core have a pronounced influence on one another in the spin ordering of individual CSNs, as shown in magnetic measurements.

Conclusions

I have successfully synthesized novel α-Cr_2O_3@α-$Ni_{0.58}Cr_{1.42}O_{2.88}$ inverted core-shell nanoparticles using my hydrothermal nanophase epitaxy (HNE) method**.** HR-TEM and XPS analysis of the core-shell nanoparticles indicates on the average a ~23.5 nm radius α-Cr_2O_3 core and ~ 5 nm thick α-$Ni_{0.58}Cr_{1.42}O_{2.88}$ shell; the XPS shows that Ni is in the 2+ state within the shell. HR-TEM and XRD analyses indicate that the corundum structure of the nanoparticle is continuous (i.e., epitaxial registry) from core to the shell and a relatively sharp, uniform interface between the two. My first principles calculations and magnetic measurements show that overall equilibrium FM spin configuration of the shell below the blocking temperature of the CSNs. Furthermore, my calculations show that the cation-oxygen bonding environment in the immediate vicinity of the substituted Ni has increased covalency and that the modification of the electronic density of states upon Ni^{2+} substitution is sufficient to give rise to FM ordering in the α-$Ni_{0.58}Cr_{1.42}O_{2.88}$ shell. The SQUID magnetometry measurements confirm the doubly inverted (i.e., $T_C < T_N$) nature of core-shell nanoparticles having enhanced magnetic properties (e.g., large

coercivity of 533 Oe and an exchange bias of 96 Oe). My HNE method should be useful for synthesis of target-specific nanomaterials having enhanced properties (e.g., superconducting, electronic, optical, etc. properties) due to selective structural characteristics that are otherwise not achievable.

Acknowledgments

S.D. and R.M. acknowledge partial support from EFree, an Energy Frontier Research Center funded by the US Department of Energy, Office of Science, Office of Basic Energy Sciences under Award Number DE-SC0001057. I thank Alexander Jankovic of the JVIC center at MSU for making the XPS measurements on our samples.

References

(1) Byers, C. P.; Zhang, H.; Swearer, D. F.; Yorulmaz, M.; Hoener, B. S.; Huang, D.; Hoggard, A.; Chang, W.-S.; Mulvaney, P.; Ringe, E.; Halas, N. J.; Nordlander, P.; Link, S.; Landes, C. F. From Tunable Core-Shell Nanoparticles to Plasmonic Drawbridges: Active Control of Nanoparticle Optical Properties. *Sci. Adv.* **2015**, *1* (11), e1500988.

(2) Estrader, M.; López-Ortega, A.; Estradé, S.; Golosovsky, I. V.; Salazar-Alvarez, G.; Vasilakaki, M.; Trohidou, K. N.; Varela, M.; Stanley, D. C.; Sinko, M.; Pechan, M. J.; Keavney, D. J.; Peiró, F.; Suriñach, S.; Baró, M. D.; Nogués, J. Robust Antiferromagnetic Coupling in Hard-Soft Bi-Magnetic Core/shell Nanoparticles. *Nat. Commun.* **2013**, *4*, 2960.

(3) Gawande, M. B.; Goswami, A.; Asefa, T.; Guo, H.; Biradar, A. V.; Peng, D.-L.; Zboril, R.; Varma, R. S. Core–shell Nanoparticles: Synthesis and Applications in Catalysis and Electrocatalysis. *Chem. Soc. Rev.* **2015**, *44* (21), 7540–7590.

(4) Lee, J.-H.; Jang, J.; Choi, J.; Moon, S. H.; Noh, S.; Kim, J.; Kim, J.-G.; Kim, I.-S.; Park, K. I.; Cheon, J. Exchange-Coupled Magnetic Nanoparticles for Efficient Heat Induction. *Nat. Nanotechnol.* **2011**, *6* (7), 418–422.

(5) Guidelli, E. J.; Baffa, O.; Clarke, D. R. Enhanced UV Emission From Silver/ZnO And Gold/ZnO Core-Shell Nanoparticles: Photoluminescence, Radioluminescence, And Optically Stimulated Luminescence. *Sci. Rep.* **2015**, *5*, 14004.

(6) Song, S.; Wang, X.; Zhang, H. CeO2-Encapsulated Noble Metal Nanocatalysts: Enhanced Activity and Stability for Catalytic Application. *NPG Asia Mater.* **2015**, *7* (5), e179.

(7) Wang, J.; Zeng, X. C. Core–Shell Magnetic Nanoclusters. In *Nanoscale Magnetic Materials and Applications*; Liu, J. P., Fullerton, E., Gutfleisch, O., Sellmyer, D. J., Eds.; Springer US, 2009; pp 35–65.

(8) Silva, A.; Silva-Freitas, rica; Carvalho, J.; Pontes, T.; Arajo-Neto, R.; Silva, K.; Carrio, A.; Egito, E. Magnetic Particles in Biotechnology: From Drug Targeting to Tissue Engineering. In *Advances in Applied Biotechnology*; Petre, M., Ed.; InTech, 2012.

(9) López-Ortega, A.; Estrader, M.; Salazar-Alvarez, G.; Roca, A. G.; Nogués, J. Applications of Exchange Coupled Bi-Magnetic Hard/soft and Soft/hard Magnetic Core/shell Nanoparticles. *Phys. Rep.* **2015**, *553*, 1–32.

(10) Meiklejohn, W. H.; Bean, C. P. New Magnetic Anisotropy. *Phys. Rev.* **1956**, *102* (5), 1413–1414.

(11) Meiklejohn, W. H.; Bean, C. P. New Magnetic Anisotropy. *Phys. Rev.* **1957**, *105* (3), 904–913.

(12) Nogués, J.; Sort, J.; Langlais, V.; Skumryev, V.; Suriñach, S.; Muñoz, J. S.; Baró, M. D. Exchange Bias in Nanostructures. *Phys. Rep.* **2005**, *422* (3), 65–117.

(13) Golosovsky, I. V.; Salazar-Alvarez, G.; López-Ortega, A.; González, M. A.; Sort, J.; Estrader, M.; Suriñach, S.; Baró, M. D.; Nogués, J. Magnetic Proximity Effect Features in Antiferromagnetic/Ferrimagnetic Core-Shell Nanoparticles. *Phys. Rev. Lett.* **2009**, *102* (24), 247201.

(14) Vasilakaki, M.; Trohidou, K. N.; Nogués, J. Enhanced Magnetic Properties in Antiferromagnetic-Core/Ferrimagnetic-Shell Nanoparticles. *Sci. Rep.* **2015**, *5*, 9609.

(15) Mao, Z.; Zhan, X.; Chen, X. Defect-Tuning Exchange Bias of Ferromagnet/antiferromagnet Core/shell Nanoparticles by Numerical Study. *J. Phys. Condens. Matter* **2012**, *24* (27), 276002.

(16) Dimitriadis, V.; Kechrakos, D.; Chubykalo-Fesenko, O.; Tsiantos, V. Shape-Dependent Exchange Bias Effect in Magnetic Nanoparticles with Core-Shell Morphology. *Phys. Rev. B* **2015**, *92* (6), 064420.

(17) Evans, R. F. L.; Bate, D.; Chantrell, R. W.; Yanes, R.; Chubykalo-Fesenko, O. Influence of Interfacial Roughness on Exchange Bias in Core-Shell Nanoparticles. *Phys. Rev. B* **2011**, *84* (9), 092404.

(18) Dey, S.; Hossain, M. D.; Mayanovic, R. A.; Wirth, R.; Gordon, R. Novel Highly-Ordered and Co(II)-Containing a-Cr2O3/a-Co0.43Cr1.57O2.9 Core-Shell Nanoparticles. *submitted*.

(19) Jamtveit, B. Crystal Growth and Intracrystalline Zonation Patterns in Hydrothermal Environments. In *Growth, Dissolution and Pattern Formation in Geosystems*; Jamtveit, B., Meakin, P., Eds.; Springer Netherlands, 1999; pp 65–84.

(20) Farzaneh, F. Synthesis and Characterization of Cr_2O_3 Nanoparticles with Triethanolamine in Water under Microwave Irradiation. *J. Sci. Islam. Repub. Iran* **2011**, *22* (4), 329–333.

(21) Liechtenstein, A. I.; Anisimov, V. I.; Zaanen, J. Density-Functional Theory and Strong Interactions: Orbital Ordering in Mott-Hubbard Insulators. *Phys. Rev. B* **1995**, *52* (8), R5467–R5470.

(22) Giannozzi, P.; Baroni, S.; Bonini, N.; Calandra, M.; Car, R.; Cavazzoni, C.; Davide Ceresoli; Chiarotti, G. L.; Cococcioni, M.; Dabo, I.; Corso, A. D.; Gironcoli, S. de; Fabris, S.; Fratesi, G.; Gebauer, R.; Gerstmann, U.; Gougoussis, C.; Anton Kokalj; Lazzeri, M.; Martin-Samos, L.; Marzari, N.; Mauri, F.; Mazzarello, R.; Stefano Paolini; Pasquarello, A.; Paulatto, L.; Sbraccia, C.; Scandolo, S.; Sclauzero, G.; Seitsonen, A. P.; Smogunov, A.; Umari, P.; Wentzcovitch, R. M. QUANTUM ESPRESSO: A Modular and Open-Source Software Project for Quantum Simulations of Materials. *J. Phys. Condens. Matter* **2009**, *21* (39), 395502.

(23) Sawada, H. Residual Electron Density Study of Chromium Sesquioxide by Crystal Structure and Scattering Factor Refinement. *Mater. Res. Bull.* **1994**, *29* (3), 239–245.

(24) Monkhorst, H. J.; Pack, J. D. Special Points for Brillouin-Zone Integrations. *Phys. Rev. B* **1976**, *13* (12), 5188–5192.

(25) Shi, S.; Wysocki, A. L.; Belashchenko, K. D. Magnetism of Chromia from First-Principles Calculations. *Phys. Rev. B* **2009**, *79* (10), 104404.

(26) Cococcioni, M.; de Gironcoli, S. Linear Response Approach to the Calculation of the Effective Interaction Parameters in the LDA+U Method. *Phys. Rev. B* **2005**, *71* (3), 035105.

(27) Perdew, J. P.; Zunger, A. Self-Interaction Correction to Density-Functional Approximations for Many-Electron Systems. *Phys. Rev. B* **1981**, *23* (10), 5048–5079.

(28) Silvi, B.; Savin, A. Classification of Chemical Bonds Based on Topological Analysis of Electron Localization Functions. *Nature* **1994**, *371* (6499), 683–686.

(29) A. D. Becke, K. E. J. E. Becke, A. D. & Edgecombe, K. E. A Simple Measure of Electron Localization in Atomic and Molecular Systems. J. Chem. Phys. 92, 5397-5403. *J. Chem. Phys.* **1990**, *92* (9), 5397–5403.

(30) Momma, K.; Izumi, F. *VESTA 3* for Three-Dimensional Visualization of Crystal, Volumetric and Morphology Data. *J. Appl. Crystallogr.* **2011**, *44* (6), 1272–1276.

(31) Khurshid, H.; Chandra, S.; Li, W.; Phan, M. H.; Hadjipanayis, G. C.; Mukherjee, P.; Srikanth, H. Synthesis and Magnetic Properties of Core/shell FeO/Fe_3O_4 Nano-Octopods. *J. Appl. Phys.* **2013**, *113* (17), 17B508.

(32) Khurshid, H.; Li, W.; Phan, M.-H.; Mukherjee, P.; Hadjipanayis, G. C.; Srikanth, H. Surface Spin Disorder and Exchange-Bias in Hollow Maghemite Nanoparticles. *Appl. Phys. Lett.* **2012**, *101* (2), 022403.

(33) Chandra, S.; Khurshid, H.; Li, W.; Hadjipanayis, G. C.; Phan, M. H.; Srikanth, H. Spin Dynamics and Criteria for Onset of Exchange Bias in Superspin Glass Fe/γ-Fe_2O_3 Core-Shell Nanoparticles. *Phys. Rev. B* **2012**, *86* (1), 014426.

(34) Tobia, D.; Winkler, E.; Zysler, R. D.; Granada, M.; Troiani, H. E. Size Dependence of the Magnetic Properties of Antiferromagnetic Cr_2O_3 Nanoparticles. *Phys. Rev. B* **2008**, *78* (10), 104412.

(35) Maldonado, F.; Novillo, C.; Stashans, A. Ab Initio Calculation of Chromium Oxide Containing Ti Dopant. *Chem. Phys.* **2012**, *393* (1), 148–152.

(36) Cao, H.; Qiu, X.; Liang, Y.; Zhao, M.; Zhu, Q. Sol-Gel Synthesis and Photoluminescence of P-Type Semiconductor Cr_2O_3 Nanowires. *Appl. Phys. Lett.* **2006**, *88* (24), 241112.

(37) M Julkarnain, J. H. Optical Properties of Thermally Evaporated Cr_2O_3 Thin Films. *Can. J. Chem. Eng. Amp Technol.* **2012**, *3* (4), 81–85.

(38) Abdullah, M. M.; Rajab, F. M.; Al-Abbas, S. M. Structural and Optical Characterization of Cr_2O_3 Nanostructures: Evaluation of Its Dielectric Properties. *AIP Adv.* **2014**, *4* (2), 027121.

(39) Mu, S.; Wysocki, A. L.; Belashchenko, K. D. Effect of Substitutional Doping on the N'eel Temperature of Cr_2O_3. *Phys. Rev. B* **2013**, *87* (5), 054435.

(40) Corliss, L. M.; Hastings, J. M.; Nathans, R.; Shirane, G. Magnetic Structure of Cr2O3. *J. Appl. Phys.* **1965**, *36*, 1099–1100.

(41) Kubo, R. Electronic Properties of Metallic Fine Particles. I. *J. Phys. Soc. Jpn.* 1962, *17* (6), 975–986.

(42) Cheetham, A. K.; Hope, D. A. O. Magnetic Ordering and Exchange Effects in the Antiferromagnetic Solid Solutions $Mn_xNi_{1-x}O$. *Phys. Rev. B* 1983, *27* (11), 6964–6967.

(43) Tang, W.; Sanville, E.; Henkelman, G. A Grid-Based Bader Analysis Algorithm without Lattice Bias. *J. Phys. Condens. Matter* **2009**, *21* (8), 084204.

(44) Sanville, E.; Kenny, S. D.; Smith, R.; Henkelman, G. Improved Grid-Based Algorithm for Bader Charge Allocation. *J. Comput. Chem.* **2007**, *28* (5), 899–908.

(45) Kumar, S.; Kim, Y. J.; Koo, B. H.; Lee, C. G. Structural and Magnetic Properties of Ni Doped CeO_2 Nanoparticles. *J. Nanosci. Nanotechnol.* **2010**, *10* (11), 7204–7207.

Supporting Information

Methods. Scanning electron microscopy. Scanning electron microscopy (SEM) imaging and energy-dispersive x-ray (EDX) spectroscopic analyses of the nanoparticles were made using an FEI Quanta 200 instrument operating at 30.0 kV. The sample was dispersed on conductive carbon tape and EDX analysis was performed on the sample using a field emission gun (FEG).

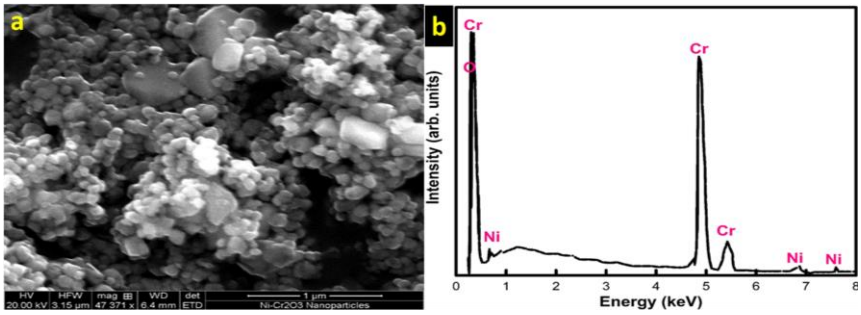

Fig. S2.1 (a) An SEM image showing that most of the nanoparticles are spherical in shape and are agglomerated. (b) SEM-EDX data confirms the presence of Ni, Cr and O in the nanoparticles.

Transmission electron microscopy. Transmission electron microscopy (TEM) samples were prepared by dispersing the Cr_2O_3-$Ni_xCr_{2-x}O_3$ nanoparticles in hexane followed by submerging the lacey carbon grid in the hexane-nanoparticle solution and subsequently drying the sample. TEM analysis was performed at the University of Arkansas Nano-Bio Materials Characterization Facility using a Titan 80-300 with the field emission gun operated at 300 keV. The simulated selected area electron diffraction (SAED) patterns were generated from the TEM images using the fast Fourier filtering (FFT) within the imageJ software.[1]

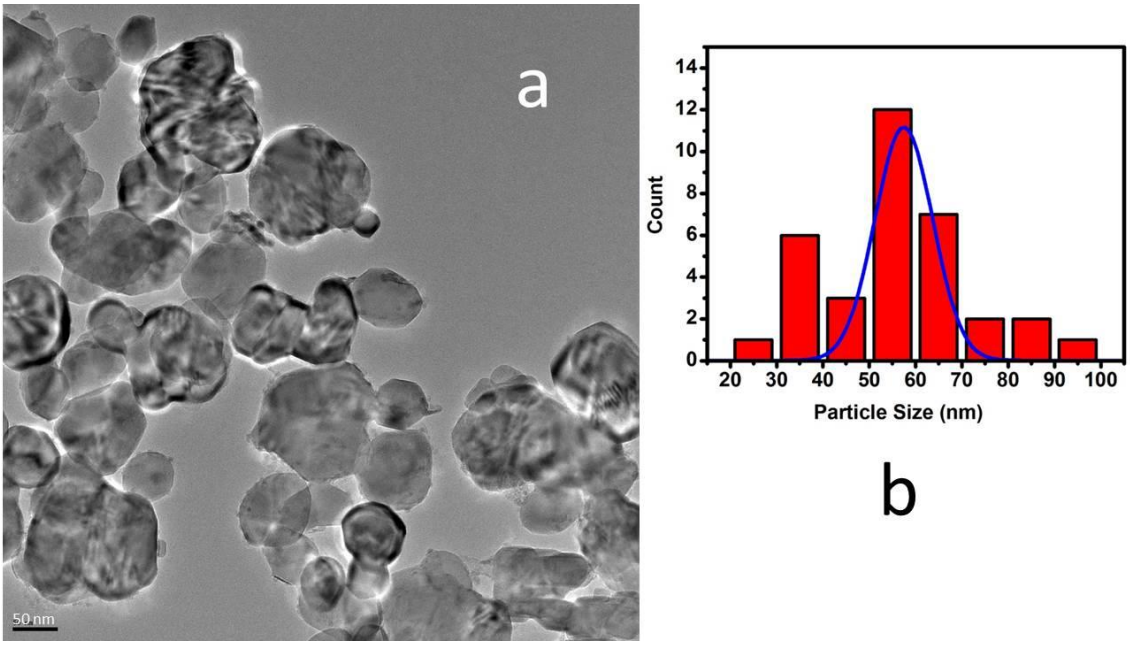

Fig. S2.2 a) TEM image of several CSNs used to estimate their mean size and b) a histogram plot of the size distribution of the CSNs and the Gaussian fit (blue line) to the distribution.

XRD measurements. The X-ray diffraction (XRD) analysis of the nanoparticles was made using the Bruker D8 Discover powder diffractometer having the characteristic x-ray radiation CuKα (λ = 1.54184 Å). The instrument was operated at 40 kV and 40 mA. A Gobel mirror and a 0.6 mm slit were used on the tube side of the set up with a 0.6 mm slit on the detector side of the diffracted beam. An overall spectrum was obtained from averaging of three individual spectra.

Rietveld refinement of the XRD data. Indexing (hkl) and symmetry-mode Rietveld refinement of the XRD pattern was made using the TOPAS 4.2 software.[2,3] The Rietveld refinement was accomplished using the corundum structure having the space group (ICSD#173470). Rietveld refinement was accomplished with a weight profile R-factor (R_{wp}) value of 2.66. In the refinement the Cr_2O_3 phase contributes 56% to the fit and the $Ni_{0.57}Cr_{1.43}O_{2.88}$ phase contributes 44% to the fit. Volume weighted mean particle size was determined to be 57(2) nm based on integral breadth method from the Rietveld refinement in TOPAS[4]. The amorphous like background in the XRD pattern is due to the glass substrate used to hold the CSN sample. The incident beam profile and peak asymmetry of the diffractometer were modeled using a modified Thompson-Cox-Hastings pseudo-Voigt peak function (TCHZ)[5] from a CeO_2 standard (NIST 674b) XRD data.[6] The lattice parameters of the corundum unit cell, z-position of the Cr atom, x-positon of the O atom and the temperature factors for both Cr and O were refined for the α-Cr_2O_3 NPs. Core and Shell part fitted by using the same constrained. For the shell region, Cr, Ni and O (to account for oxygen vacancy formation) atoms with partial site occupancies were used in the atomic sites within the refinement. Structural parameters from the refinement are given in the Table 2.1 shown below.

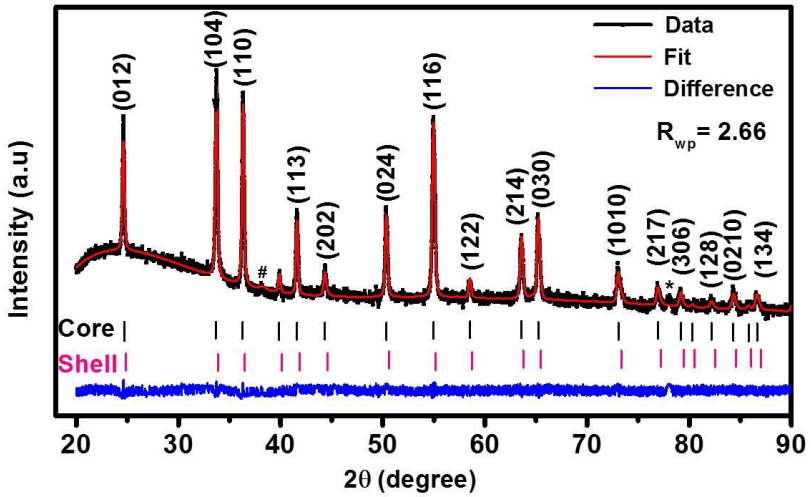

Fig. S2.3. XRD data (black line) measured from the α-Cr_2O_3/α-$Ni_{0.57}Cr_{1.43}O_{2.88}$ CSNs at ambient conditions and the Rietveld refinement of the data (red line). Minor amounts of a NiO phase (marked with #) and an unknown impurity phase (marked *) are present in the sample.

Table S2.1. Summary of structural results obtained from Rietveld refinement for α-Cr_2O_3/α-$Ni_{0.57}Cr_{1.43}O_{2.88}$ inverted CSNs.

Core: α-Cr_2O_3 NPs (SG #167: $R\bar{3}c$); a = b = 4.96139(86) Å; c = 13.6014(27) Å ; V = 289.95(12) Å^3;					
Atoms	x	y	z	Site occupancy	B (Å^2)
Cr	0	0	0.34629(49)	1.0	1.2
O	0.3093(34)	0	1/4	1.0	1.2
Shell: α-$Ni_{0.57}Cr_{1.43}O_{2.88}$ (SG #167: $R\bar{3}c$); a = b = 4.9549(16) Å; c = 13.5831(44) Å ; V = 288.80(20) Å^3; core-shell size = 58(42) nm					
Ni	0	0	0.348(65)	0.285	0.6
Cr	0	0	0.348(28)	0.965	2
O	0.3289(67)	0	1/4	0.285	0.6
Impurity phase: NiO (SG Fm-3m); a= 4.0838(43) Å					
Ni	0	0	0	1	0.414
O	1/2	1/2	1/2	1	0.61

X-Ray Photoemission Spectroscopy. Surface composition analysis of the sample was made using x-ray photoelectron spectroscopy (XPS). An Al K-alpha source with a characteristic energy of 1486.6 eV was used and the Ag $3d_{5/2}$ peaks were used for calibration of the source and analyzer. The CasaXPS 2.3.16 software was used for analysis and peak fitting of the XPS spectra**.** Shirley background types were used for XPS peak fitting within the CasaXPS software package. The Gaussian-Lorentzian product GL(30) functions were used in the fitting of the peak line shapes. Fig. S2.4 shows the high resolution XPS spectra of the O1s, $Cr2p_{3/2}$, $Ni2p_{3/2}$ peaks. The O1s peak is composed of 3 deconvoluted peaks, at 530.34 eV and 528.9 eV due to the Cr-O and Ni-O bonding, respectively and one at 530.97 eV which corresponds to the Cr-OH, Ni-OH bonds in the surface region of the sample. The overall $Cr2p_{3/2}$ peak has two contributions: The peak at 575.90 eV Cr-O bonding is consistent with the +3 oxidation state of Cr whereas the second peak at 577.04 eV which is due to hydroxide bonding of Cr. The high resolution scan of Ni $2p_{3/2}$ contains a satellite peak at 859.91 eV. Analysis of the overall Ni $2p_{3/2}$ peak shows that Ni is in the +2 oxidation state in the CSNs on account of its Ni-O bonding peak contribution being located at 854.30 eV: another contribution at 855.30 eV corresponds to the hydroxide bonding of Ni. Table S2.2 shows the atomic percentage of elements found from analysis of the $Cr2p_{3/2}$, O1s, $Ni2p_{3/2}$, C1s peaks.

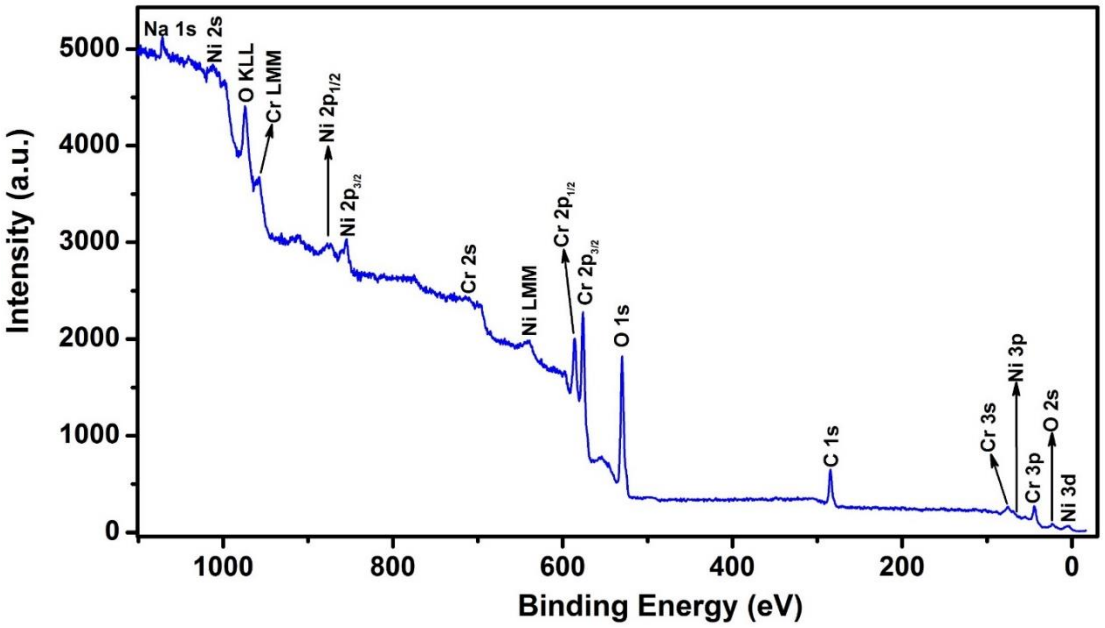

Fig. S2.4 XPS survey scan of our α-Cr_2O_3/α-$Ni_{0.58}Cr_{1.42}O_{2.88}$ nanoparticles, showing the Cr, O, Ni and C1s peaks (from carbon tape containing the sample) of the elements contained in the sample.

Table S2.2. Elemental analysis from XPS data measured from the α-Cr_2O_3/α-$Ni_{0.58}Cr_{1.42}O_{2.88}$ inverted core-shell NPs. The analysis for elemental content using the $Cr2p_{3/2}$, O1s and $Ni2p_{3/2}$ peaks was accomplished using a Shirley background.

Element	Peaks	Position	FWHM	Area	Atomic %
Cr	$Cr2p_{3/2}$	576.23	3.7	4870	26.17
O	O1s	530.23	3.5	4769.02	68.47
Ni	$Ni2p_{3/2}$	854.73	4.9	2068.9	5.35

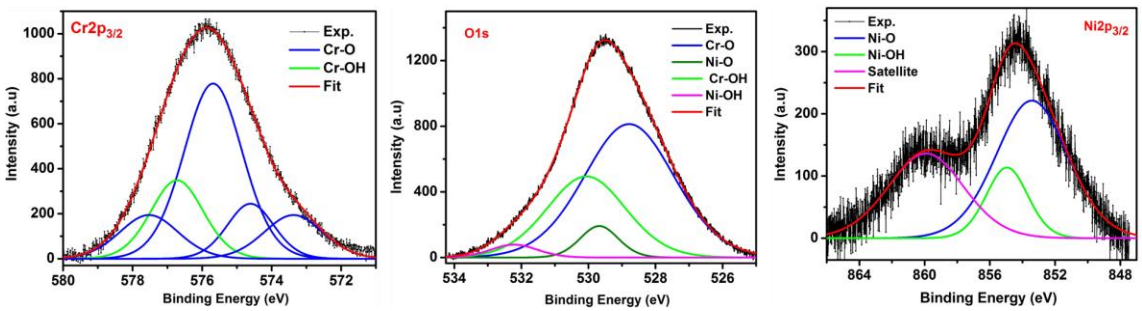

Fig. S2.5 High resolution XPS data measured from the α-Cr_2O_3/α-$Ni_{0.58}Cr_{1.42}O_{2.88}$ CSNs (black line) and fit to the data (colored lines) for Cr $2p_{3/2}$ (left panel), O 1s (middle panel), and Ni $2p_{3/2}$ (right panel).

Table S2.3. Results from fitting of the high-resolution XPS spectra measured from the CSNs. GL(30) indicates a Gaussian-Lorentzian product formula where the percentage of Lorentzian peak shape is indicated in the parenthesis.

$Cr2p_{3/2}$		Position	FWHM	Line Shape	Area	%Area
Cr-O	Peak-1	573.37	2	GL(30)	421.11	11.63
	Peak-2	574.61	1.6	GL(30)	421.11	11.63
	Peak-3	575.68	2	GL(30)	1684.42	46.51
	Peak-4	577.53	2	GL(30)	421.11	11.63
Cr-OH		576.8	1.8	GL(30)	673.77	18.68
O1s						
Cr-O		528.8	3.1	GL(30)	2800	59.92
Ni-O		529.68	1.34	GL(30)	280	5.95
Cr-OH		530.1	2.8	GL(30)	1484	31.55
Ni-OH		532.22	1.64	GL(30)	140	2.98
$Ni2p_{3/2}$						
Ni-O		853.42	5.18	GL(30)	1242.23	51.24
Ni-OH		854.95	3	GL(30)	372.67	15.37
Satellite		859.91	5.5	GL(30)	809.24	33.38

Estimate of Ni concentration in α-Cr_2O_3@α-$Ni_xCr_{2-x}O_y$ CSNs The average size of CSNs were found to be ~57 nm with a shell size of ~5 nm from the TEM and XRD measurements. Given that the CSNs have the following approximate dimensions as illustrated in Figure S2.6: R = 28.5 nm for average radius of CSNs, r_2 = 23.5 nm (subtracting 5 nm for the shell region) average radius for the core, and $r_1 \approx$ 18.5 nm (we assume ~10 nm of sampling depth for XPS). In this case, the ratio of the volume of the shell to the XPS sampling volume could be estimated as, z = (volume of shell)/(volume of the region probed by XPS) ≈ 0.6.

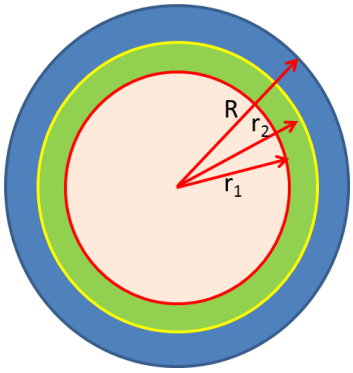

Figure S2.6. A schematic diagram of a core-shell nanoparticle: R is the radius of the entire nanoparticle, r_1 indicates the radius defining the volume of the nanoparticle excluded from XPS sampling (r_1 = R − XPS sampling depth), and r_2 is the radius defining the core region of the nanoparticle (r_2 = R – width of the shell region).

From the XPS results, the atomic percentages of the elements were found to be as follows: Ni:Cr:(O+OH) = 5.35:26.17:68.47. If we exclude the contribution from OH^-, then for the stoichiometric chromate phase, we get Ni:Cr:O = 5.35:26.17:44.62. Normalization of the contribution from the three elements gives ratios of Ni:Cr:O = 7.03:34.37:58.6.

Using the following expression to find the concentration x in the XPS sampling volume:

$(1-z)\bullet[Cr_2O_3] + z\bullet[Ni_xCr_{2-x}O_3]$, we can write,

$0.0703[Ni] + 0.3437[Cr] + 0.586[O] = (1 - 0.6)\bullet\{0.4[Ni] + 0.6[O]\} + 0.6\bullet\{p[Ni] + (0.423 - p)[Cr] + 0.577[O]\}$.

This yields, $0.0703[Ni] + 0.3437[Cr] = 0.4138[Cr] + 0.6\bullet p\bullet([Ni]-[Cr])$ or $p \approx 0.1167$. Thus, by stoichiometry, $x = 5\bullet p = 0.58$. Accounting for the slight deficiency (~1.4 at%) of oxygen in the shell, we get $Co_{0.58}Cr_{1.42}O_{2.88}$ as the approximate stoichiometric formula for the nanophase in the shell region of the CSNs. The presence of oxygen vacancies on the CSNs is confirmed from Rietveld refinement of XRD data.

UV-Vis Measurements A suspension of the CSNs was made in DI water and allowed to evaporate on a microscope glass slide. An Ocean Optics HR 4000 spectrophotometer and a fiber-optic coupled DT-Mini-2 deuterium/tungsten-halogen lamp source (Ocean Optics) were used to measure The UV-Vis transmission/absorption spectra of the CSNs. The accumulated spectra were collected by using integration time of ~200 ms and average of 10 scan. The energy band gap of the CSNs was estimated from the tauc plot of $(\alpha\cdot h\nu)^{1/2}$ vs $h\nu$, where α is the absorption coefficient. The fit of the linear part intersect the energy axis at a value of ~2.45 eV which is the band gap of the nanoparticles. Fig S2.7 shows the tauc plot.

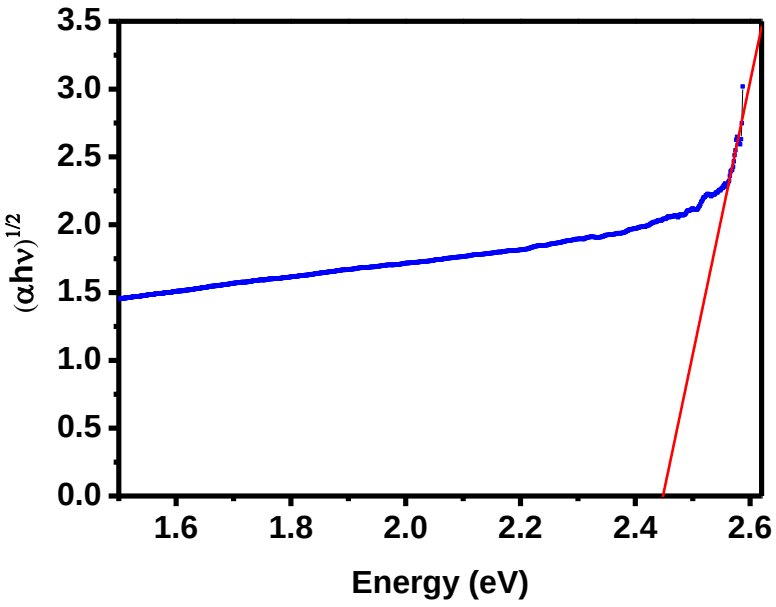

Fig. S2.7. The $(\alpha \cdot h\nu)^{1/2}$ quantitity plotted vs photon energy ($h\nu$) as determined from the UV-Vis absorption spectra measured from the CSNs. The extrapolated fitted line intersects the energy axis at 2.45 eV.

Computational Details The calculation of partial charges on Ni, Cr and O atoms was made using Bader's procedures, which provides accurate atomic charges for plane wave basis functions, and a program that employs a fast algorithm for performing the Bader analysis.[7] The Bader charge analysis of the α-Cr_2O_3, α-Ni(III)Cr_3O_6 and α-Ni(II)Cr_3O_6 structures is shown in Table S2.4. Electron localization function (ELF) analysis was performed using procedures described elsewhere;[8,9] the ELF images were generated using the visualization software Vesta.[10]

Table S2.4: Computed magnetic moments of individual atoms in α-Cr_2O_3, α-Ni(III)Cr_3O_6 , and α-Ni(II)Cr_3O_6.

Atom	α-Cr_2O_3 (in μ_B)	α-Ni(III)Cr_3O_6 (in μ_B)	α-Ni(II)Cr_3O_6 (in μ_B)
Cr1	+3.11	3.13	3.12
Cr2	-3.11	-3.17	-3.10
Cr3/Ni	-3.11	**-0.58**	**0.12**
Cr4	+3.11	3.10	3.09

Table S2.5: Bader partial charge analysis of α-Cr_2O_3, α-Ni (III)Cr_3O_6 and α-Ni(II)Cr_3O_6 in the primitive rhombohedral 1x1x1 structures; e is the fundamental charge unit of ~1.6 x 10^{-19} C.

Atom	**Charge (α-Cr_2O_3) ·e**	**Charge (α-Ni (III)Cr_3O_6) ·e**	**Charge (α-Ni (II)Cr_3O_6) ·e**
O1	-1.6761	-1.4407	-1.5665
O2	-1.676	-1.391	-1.4373
O3	-1.6925	-1.3747	-1.4264
O4	-1.6923	-1.4738	-1.6156
O5	-1.7137	-1.4259	-1.502
O6	-1.7139	-1.4205	-1.5014
Cr1	+2.5409	+2.5320	+2.5191
Cr2	+2.5409	+2.50	+2.4707
Cr3/Ni3	+2.5412	+0.9433	+0.5468
Cr4	+2.5412	+2.5506	+2.5121

First principles calculations starting with various substitutional positions and spin orientations for Ni atoms in the 20 atom 1x1x2 supercell chromia structure have been made. Table S2.5 shows the energy values relative to the lowest energy configuration in

the supercell and the overall magnetic moment of the α-$Ni_2(II)Cr_6O_{12}$ structure for the cases of substitutional positons described below. Cases 1 and 6 correspond to having two nearby ++ Ni's (Fig. S6) substituted in the buckled honeycomb of the corundum structure; cases 2 and 1 are the same 1 but having +- spin orientations for the two Ni atoms; cases 3 and 4 correspond to having two ++ Ni's and two +- Ni's, respectively, substituted in alternate buckled honeycomb planes. Case 5 is identical to case 1 except where we attempt to force one Cr (Cr3) spin in + arrangement (rather than original – spin arrangement) so as to balance the number of spin-up vs spin-down atoms in the supercell. Cases 7 and 8 correspond to Ni-Ni +- substitution in closest (Case-7) and farthest (Case-8) proximity to each other. Among all of the cases that were considered, the FM coupling configurations (Cases-1, 2, 3, 6) resulted in ground states with lowest possible energies and net overall magnetic moments. The remaining cases (4,5,7,8) results in net 0 magnetic moment higher energy values These results show that the FM configuration, which results in a net magnetic moment of the supercell, is the most stable magnetic configuration for the α-$Ni(II)_2Cr_6O_{12}$ structure.

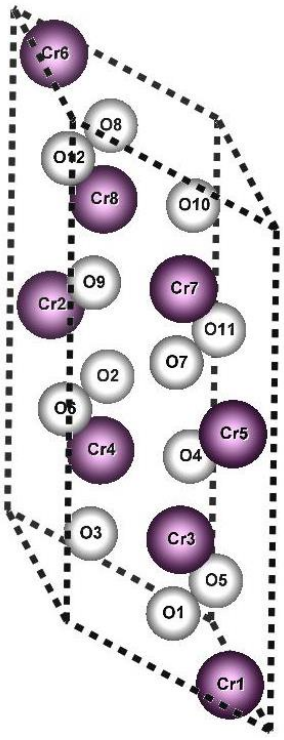

Figure S2.8: A diagram of the 20 atom 1x1x2 supercell showing the Cr and O atomic positions; in the first principles calculations, two Ni atoms are substituted.

Table S6: Calculation results for substitution of two Ni atoms for Cr atoms in various sites in a 20 atom 1x1x2 supercell.

	Substitution	Spin Configuration	Energy difference (eV)	Overall Magnetic Moment (μ_B)
Case-1	Cr4-Cr5	++	+0.31	-6.00
Case-2	Cr4-Cr5	+-	0	-6.00
Case-3	Cr4-Cr1	++	+0.54	-4
Case-4	Cr4-Cr7	+-	+0.60	0
Case-5	Cr4-Cr5	++	+1.17	0
Case-6	Cr3-Cr6	--	+0.32	+6
Case-7	Cr3-Cr4	-+	+0.94	0
Case-8	Cr3-Cr8	-+	+0.60	0

References

(1) Schneider, C. A.; Rasband, W. S.; Eliceiri, K. W. *Nat. Methods* **2012**, *9* (7), 671–675.

(2) Cheary, R. W.; Coelho, A. *J. Appl. Crystallogr.* **1992**, *25* (2), 109–121.

(3) Coelho, A. A. *J. Appl. Crystallogr.* **2003**, *36* (1), 86–95.

(4) Balzar, D.; Audebrand, N.; Daymond, M. R.; Fitch, A.; Hewat, A.; Langford, J. I.; Le Bail, A.; Louër, D.; Masson, O.; McCowan, C. N.; Popa, N. C.; Stephens, P. W.; Toby, B. H. *J. Appl. Crystallogr.* **2004**, *37* (6), 911–924.

(5) Thompson, P.; Cox, D. E.; Hastings, J. B. *J. Appl. Crystallogr.* **1987**, *20* (2), 79–83.

(6) Finger, L. W.; Cox, D. E.; Jephcoat, A. P. *J. Appl. Crystallogr.* **1994**, *27* (6), 892–900.

(7) Henkelman, G.; Arnaldsson, A.; Jónsson, H. *Comput. Mater. Sci.* **2006**, *36* (3), 354–360.

(8) Silvi, B.; Savin, A. *Nature* **1994**, *371* (6499), 683–686.

(9) A. D. Becke, K. E. J. E. *J. Chem. Phys.* **1990**, *92* (9), 5397–5403.

(10) Momma, K.; Izumi, F. *J. Appl. Crystallogr.* **2011**, *44* (6), 1272–1276.

STRUCTURAL AND MAGNETIC PROPERTIES OF WELL-ORDERED INVERTED CORE-SHELL α-Cr_2O_3/α-$M_xCr_{2-x}O_{3-y}$ (M=Co, Ni, Mn, Fe) NANOPARTICLES

Abstract

Magnetic core shell nanoparticles (NPs) have potential for applications in magnetic random access memory, spintronic devices, and drug delivery systems. my investigations is focused on the synthesis of inverted core shell nanoparticles and characterization of their structural and magnetic properties. By using my hydrothermal nanophase epitaxy technique, I am able to synthesize well-ordered α-Cr_2O_3@α-$M_xCr_{2-x}O_{3-y}$ (M = Co, Ni, Mn, Fe) inverted core-shell nanoparticles. This typically results in the formation of novel phases of $M_xCr_{2-x}O_{3-y}$ shells having ferromagnetic/ferrimagnetic (FM/FiM) spin ordering and an antiferromagnetic (AFM) Cr_2O_3 core structure. The combined results from XRD and high-resolution TEM (HRTEM) provide evidence of the presence of corundum phase both in the shell and in the core regions. HRTEM results also show a sharp interface exhibiting epitaxial atomic registry of shell atoms over highly ordered core atoms whereas TEM-EDX analyses show that the M atoms reside predominantly in the shell regions. The XPS analyses of the NPs indicate the M transition metals incorporated in the shell are in the +2 oxidation state. Magnetic measurements show well developed hysteresis loops: The field cooled hysteresis loops reveal horizontal shifts in the applied field axis and vertical shifts in the magnetization axis, relative to the zero-field cooled hysteresis loops. This provides direct evidence for the exchange bias effect between the AFM α-Cr_2O_3 core and the FM/FiM α-$M_xCr_{2-x}O_{3-y}$ shell. The XPS data

are consistent with oxygen vacancy formation in order to maintain charge neutrality upon substitution of the M^{2+} ion for the Cr^{3+} ion in the α-$M_xCr_{2-x}O_{3-y}$ shell. The FM/FiM ordering in the shell may at least partially result from the F-center exchange coupling between the oxygen-vacancy induced bound magnetic polaron and nearby cations.

Introduction

Investigations of core-shell nanoparticles (CSNs) have gained considerable interest recently due to their potential applications in magnetic random access memory, spintronic devices and biomedical application [1,2]. The nanostructural/composite aspect of CSNs provides the opportunity of tuning their physico-chemical properties by adjustment of the core-shell size, modification of the interface characteristics and by varying the chemical composition. In addition, such tunability offers an opportunity to develop multi-functionality in CSNs. Different types of synthesis process such as co-precipitation, hydrothermal, sol-gel process have been used to develop the composite materials at the nanoscale (including CSNs) [1,2]. For magnetic CSNs, this has typically been accomplished by starting with a metallic core which is oxidized to form a metal oxide shell (e.g., Ni@NiO CSN). Inverted CSNs, which have an antiferromagnetic (AFM) core and a ferromagnetic (FM) or ferrimagnetic (FiM) shell, are of particular interest because their greater ease of tunability leading to stronger core-shell interaction and potentially more enhanced magnetic properties [3]. Transition metal oxides exhibit interesting electrical, optical and magnetic properties when they are reduced down from bulk to the nanoscale in size. Chromia (Cr_2O_3) is an important transition metal oxide which has AFM magnetic moment ordering below the Néel temperature and offers

potential for inverted CSN synthesis. Transition metal doping into the structure of chromia provides the opportunity to modify the physicochemical properties and tune the material for optimal performance in various applications. The incorporation of first-row transition metal elements having partially filled d orbitals as dopants in Cr_2O_3 typically results in significant changes in the electronic structure (e.g., by introducing new inter band gap levels) and in interesting magnetic properties, due to the magnetic moments on the dopant sites [4]. Herein, we discuss my hydrothermal nanophase epitaxy (HNE) technique which is used to grow highly structured chromia (Cr_2O_3)-based inverted CSNs having well-ordered core-shell interfaces. In this paper, I discuss several of my chromia-based CSNs with an emphasis of results being presented for α-Cr_2O_3@α-$Mn_{0.30}Cr_{1.70}O_3$ nanoparticles.

Experimental

The Cr_2O_3 nanoparticles (NPs) were synthesized by using the procedure described by Farzaneh et el. [5]. A 0.2 M aqueous solution of chromium nitrate was made using commercially available $Cr(NO_3)_3 \cdot 9H_2O$ (Sigma-Aldrich) and HPLC water. The water was first deoxygenated by passing dry nitrogen gas through it at ~60 °C. Next, triethanolamine (TEOA) was added to the aqueous solution in 1:2 molar ratio. This mixture was magnetically stirred for 1 hour and subsequently cooked in a microwave oven for 5 minutes. The aqueous solution was then magnetically stirred for 10 minutes and then heated in the microwave oven for 4 minutes. This cycle was repeated four times after which the solution was left on top of a magnet until a dark green colored precipitate was formed at the bottom of the beaker. The harvested precipitate was then heated to

evaporate the water resulting in the formation of a thick slurry. The slurry was subsequently calcined at a temperature of 750 ^{o}C for 5 hours in the presence of atmosphere. Upon calcination, the sample formed into a dark-green colored nano powder. For CSN synthesis, a 0.05 M aqueous solution was prepared from different transition metal chlorides ($NiCl_2$, $CoCl_2$, $MnCl_2$, $FeCl_2$) using HPLC water; the ambient-condition solution pH was typically adjusted to be below 6.5. Then, ~0.3 g of Cr_2O_3 nanoparticles were added to the solution, sonicated for 20 minutes and subsequently loaded in a Teflon reactor and hydrothermally treated at 200 °C for 13 hours. After hydrothermal treatment, the CSN were rinsed and harvested. The harvested CSNs were subsequently calcined at 500 °C for ~2 hours.

The magnetic measurements were made using a Quantum Design (MPMS/XL) SQUID magnetometer, at a temperature range of 5K-330K and in a field varying between ± 5 kOe. A fixed quantity of (25-40 mg) of sample was placed in a gelatin capsule, which was positioned inside the low temperature vessel of the SQUID instrument for the magnetic measurements. In addition, a Quantum Design PPMS-VSM instrument was used (at CCMR; Cornell U.) for a portion of the magnetic measurements under nearly identical conditions as with the SQUID. The field cooling for the magnetic hysteresis curve measurements, which were made at 5 K, was accomplished starting from 330 K to below the Néel temperature of the sample in a field of 20,000 Oe. In the case of field cooled magnetization measurements vs temperature, the sample was cooled in a field of 500 Oe starting from 330 K. Transmission electron microscopy (TEM) samples were prepared by dispersing the NPs in hexane and depositing samples of these on lacey carbon grids. TEM analysis was performed using a Titan 80-300 with the field emission

gun operated at 300 keV. The simulated selected area electron diffraction (SAED) patterns were generated from the TEM images using the fast Fourier filtering (FFT) within imageJ [6].

X-ray diffraction (XRD) measurements ($\theta - 2\theta$ scans) were made at 25 °C on the as prepared Cr_2O_3 NPs and the CSNs using a diffractometer (Bruker D8 Discover) that utilizes Cu Kα radiation (λ = 1.54184 Å) from a sealed tube operating at 40 kV and 40 mA. A Gobel mirror and a 0.6 mm slit were used in the incident side of the x-ray beam whereas a 0.6 mm slit was mounted in front of the detector. Structural parameters were extracted from the XRD patterns using the Bruker TOPAS full-pattern refinement program [7]. The background function for the XRD pattern was modelled using a Chebychev polynomial of 9-th order. The amorphous like background of the XRD data measured from samples, which originates from the glass substrate used to hold the NPs, was modelled using a broad Voigt function. A non-linear least square fitting was performed to minimize the value of "R-weighted pattern" (R_{wp}) during Rietveld refinement. The X-Ray Photoelectron Spectroscopy (XPS) was made using a Thermo Scientific Alpha 110 hemispherical analyzer (pass energy = 25 eV) and an Al K-alpha x-ray source with a characteristic energy of 1486.6 eV. The CasaXPS 2.3.16 software package was used for analysis and peak fitting of the XPS spectra calibrated using the C 1s peak.

Results and discussion

Figure 3.1 shows the TEM images and EDX analysis of α-Cr_2O_3@α-$Mn_{0.30}Cr_{1.70}O_3$ CSNs; the compound stoichiometry of the shell was determined from XPS elemental analysis. Figure 3.1(a) shows a HRTEM image of a select CSN. For this typical nanoparticle, the core and shell are separated by an interface which is slightly more structurally disordered than in my other α-Cr_2O_3@α-$M_xCr_{2-x}O_{3-y}$ (M=Co, Ni, Fe) CSNs. As shown in Figure 3.1 for α-Cr_2O_3@α-$Mn_{0.30}Cr_{1.70}O_3$ CSNs, the growth of the shell maintains atomic registry of the core in my α-Cr_2O_3@α-$M_xCr_{2-x}O_{3-y}$ CSNs [8,9].

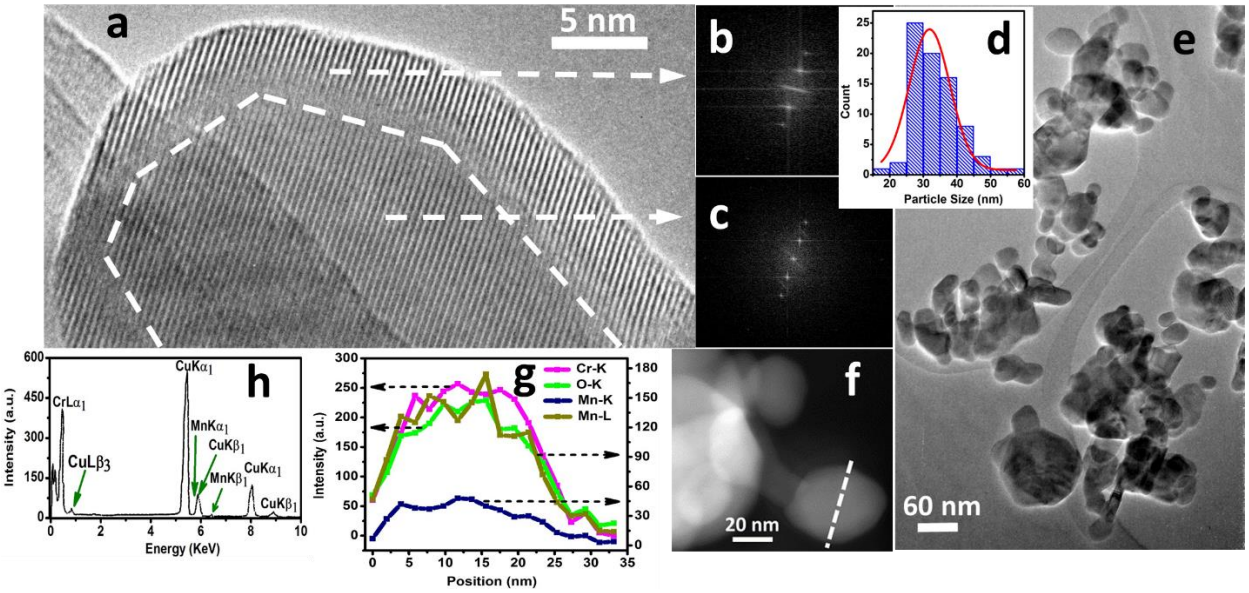

Figure 3.1. (a) A HRTEM image of a typical core shell nanoparticles; (b) FFT of core; (c) FFT of shell; (d) particle size distribution histogram plot; (e) TEM image of the nanoparticles; (f) HADF image of a single nanoparticle used for line scan analysis and (g) the line scan analysis and (h) EDX analysis of the select nanoparticle.

The shell region of the nanoparticle shown in Figure 3.1 is 4 nm in thickness. My detailed TEM analysis of α-Cr_2O_3@α-$M_xCr_{2-x}O_{3-y}$ CSNs shows that shell thickness varies between 4 to 8 nm. Figure 3.1 (b) and (c) show that the FFT's of the shell and core

regions of the CSN, respectively, have identical symmetry providing further evidence of epitaxial growth of the shell. Figures 3.1 (d) and (e) show the particle size distribution analysis of the CSNs. The predominant morphology of the α-Cr_2O_3@α-$M_xCr_{2-x}O_{3-y}$ CSNs is quasi-spherical in nature. A Gaussian fit of the histogram plot of particle size distribution gives an average particle size of 31.9(1) nm for α-Cr_2O_3@α-$Mn_{0.30}Cr_{1.70}O_3$ CSNs. Figure 3.1 (f) shows a high angle annular dark field image whereas Figures 3.1 (g) and (h) show EDX line profile and EDX analysis, respectively of a select α-Cr_2O_3@α-$Mn_{0.30}Cr_{1.70}O_3$ CSN. The TEM elemental analysis confirms the presence of Mn in the shell of the nanoparticle. Similar TEM elemental analyses and single NP elemental mapping, of α-Cr_2O_3@α-$M_xCr_{2-x}O_y$ CSNs shows dominant distribution of the incorporated transition metal (Co, Ni, Fe) in the shell regions [8,9]. XPS analyses of high-resolution M $2p_{3/2}$ peaks indicates that the substitutional transition metal M = Mn, Co, Ni, Fe, is in the divalent, i.e., M^{2+}, oxidation state [8,9]. This was accomplished by design in an attempt to engineer multifunctionality (i.e., magnetic and catalytic enhancement) of my CSNs.

Figure 3.2 shows the XRD data measured from the α-Cr_2O_3@α-$Mn_{0.3}Cr_{1.70}O_3$ CSNs. The Rietveld refinement of the XRD data was made by considering contributions from the core α-Cr_2O_3 phase and the α-$Mn_{0.30}Cr_{1.70}O_3$ shell phase. The lattice parameters obtained from the Rietveld refinement for the α-Cr_2O_3 core are a = b = 4.95838(51) Å, c = 13.5952(16) Å whereas for the α-$Mn_{0.30}Cr_{1.70}O_3$ shell the lattice parameter are a = b = 4.9579(36) Å, c = 13.573(16). This indicates a slight unit cell volume contraction in the shell compared to that of the core (see Figure 3.2 for core vs shell peak positions). All of the peaks correspond to the corundum structure phase showing that no other co-related

Mn-bearing phase is observed in the CSNs. Similar results are found from XRD data measured from my other α-Cr_2O_3@α-$M_xCr_{2-x}O_{3-y}$ (M=Co, Ni, Fe) CSNs. Rietveld refinement yields a α-Cr_2O_3@α-$Mn_{0.30}Cr_{1.70}O_3$ CSN size of 33(1) nm, which is consistent with the TEM results.

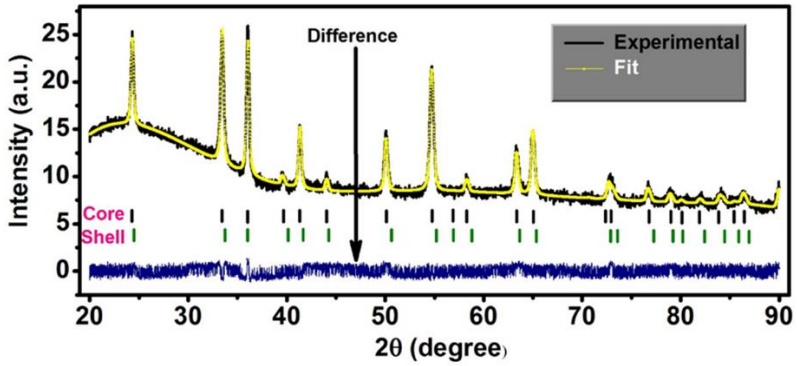

Figure 3.2. Xray Diffraction data of α-Cr_2O_3/α-$Mn_{0.30}Cr_{1.70}O_3$ core-shell nanoparticles.

Figure 3.3 (a) shows the magnetization vs applied magnetic field (H) data, under zero field cooled (ZFC) and field cooled (FC) conditions, measured from the α-Cr_2O_3@α-$Mn_{0.3}Cr_{1.70}O_3$ CSNs at 5 K. Both the FC and ZFC data exhibit predominantly antiferromagnetic characteristics; the magnetization does not reach saturation in the applied magnetic field at up to ±5 kOe. Both the ZFC and FC graph show small coercivity values: The ZFC curve shows a coercivity value of 8 Oe whereas the FC curve yields a value of 42 Oe. This indicates a small FM or FiM contribution due to the incorporation of Mn^{2+} in the shell region of the α-Cr_2O_3@α-$Mn_{0.30}Cr_{1.70}O_3$ CSNs. The FC hysteresis curve shifts to the left (i.e., lower H values) compared to the ZFC curve. This provides evidence of an exchange bias effect between the FM/FiM shell and the

AFM core of the CSNs. The measured exchange bias field (H_E) of the α-Cr_2O_3@α-$Mn_{0.30}Cr_{1.70}O_3$ CSNs is 294 Oe.

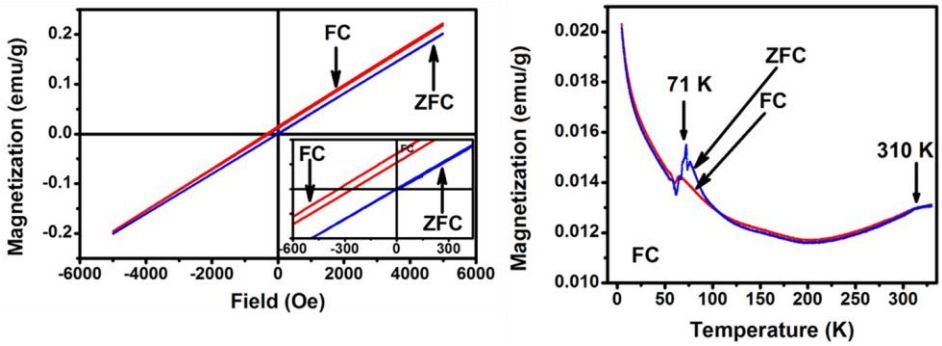

Figure 3.3. (a) Zero field cooled (ZFC) and field cooled (FC) magnetization vs applied field (M vs H) measurement data for α-Cr_2O_3@α-$Mn_{0.30}Cr_{1.70}O_3$ CSNs: The inset shows the data near the H = 0 Oe region. (b) Magnetization vs temperature data measured from the same CSNs.

Figure 3.3 (b) shows the magnetization vs temperature data measured from the α-Cr_2O_3@α-$Mn_{0.30}Cr_{1.70}O_3$ CSNs. Field cooling was made at an H field of 500 Oe from above the Néel temperature of the nanoparticles (310 K), as determined by the kink in the ZFC curve in that region of temperature. The FC curve follows the ZFC curve throughout the temperature range of 5 to 330 K except for a prominent kink observed at 71 K in the ZFC curve, which corresponds to the Curie temperature (T_C) of the α-$Mn_{0.30}Cr_{1.70}O_3$ shell of the CSNs. The synthesis of a FM/FiM shell overgrown onto an AFM core results in an inverted magnetic architecture in my α-Cr_2O_3@α-$Mn_{0.30}Cr_{1.70}O_3$ CSNs. This is consistent with the magnetic properties of my other α-Cr_2O_3@α-$M_xCr_{2-x}O_{3-y}$ (M=Co, Ni, Fe) CSNs.

The use of my HNE technique enables for synthesis of CSN typically having sharp, well-ordered core-shell interfaces which should enhance the exchange bias effects

between the AFM core and FM/FiM shell. My α-Cr_2O_3@α-$Co_{0.38}Cr_{1.42}O_{2.92}$ CSNs exhibit a smaller exchange bias effect (H_E = 5 Oe) but larger coercivities (FC coercivity = 45 Oe) whereas both the α-Cr_2O_3@α-$Ni_{0.58}Cr_{1.42}O_{2.88}$ and α-Cr_2O_3@α-$Fe_{0.40}Cr_{1.60}O_{2.92}$ CSN systems have substantially greater FC coercivities (534 and 729 Oe) but bracketing exchange bias fields (100 and 365 Oe), respectively, than the α-Cr_2O_3@α-$Mn_{0.30}Cr_{1.70}O_3$ CSNs. The trend of the exchange bias field strength (Co(II) < Ni(II) < Mn(II) < Fe(II) as substitutional M(II) ion in shell of CSNs) most likely reflects the details of the electronic band structure and magnetic properties of the α-$M_xCr_{2-x}O_{3-y}$ shell vs those of the α-Cr_2O_3 core of my CSNs. The nature of interaction between M(II)-M(II) and M(II)-Cr(III) ions leading to the FM or FiM characteristics of the α-$M_xCr_{2-x}O_{3-y}$ shell, whether it is by direct exchange, superexchange, bound magnetic polaron, etc., is not well understood. In order to better understand its magnetic characteristics, I have begun first principles density functional theory (DFT) calculations of α-$M_xCr_{2-x}O_3$ structures. My computational results show that the equilibrium α-$Ni(II)_{0.5}Cr_{1.5}O_3$ structure exhibits an overall FM ordering in the 1x1x1 primitive rhombohedral unit cell with a net magnetic moment of 2.96 Bohr magnetons. The full results from my computational study will be published elsewhere.

Conclusions

My HNE method was used to successfully synthesize novel α-Cr_2O_3@α-$M_xCr_{2-x}O_{3-y}$ (M = Co, Mn, Ni, Fe) CSNs. XPS measurements indicate that the M transition ion is in the 2+ state within the shell. HRTEM and XRD analyses show that both the core and shell of the CSNs have the corundum structure. The HRTEM analyses indicate epitaxial

growth of the shell over the core and in general a sharp, uniform core-shell interface in the CSNs. The SQUID magnetometry measurements confirm the existence of an exchange bias effect between the core and shell (i.e., inverted CSNs) whose strength varies depending upon the nature of the M transition ion that is incorporated in the nano-compound shell. My first principles DFT calculations show that the overall equilibrium spin configuration of the α-$Ni(II)_{0.5}Cr_{1.5}O_3$ structure has FM character.

Acknowledgements

S.D. and R.M. acknowledge partial support from EFree, an Energy Frontier Research Center funded by the US Department of Energy, Office of Science, Office of Basic Energy Sciences under Award Number DE-SC0001057. I thank Rishi Patel and Alexander Jankovic of the MSU-JVIC center for assistance with XPS measurements on my samples and the MSU Graduate College for providing partial support for this project.

References

1. M.B. Gawande, A. Goswami, T. Asefa, H. Guo, A.V. Biradar, D.-L. Peng, R. Zboril, R.S. Varma, *Chem. Soc. Rev.* **44,** 7540–7590 (2015).

2. N.J. Borys, M.J. Walter, J. Huang, D.V. Talapin, and J.M. Lupton, *Science* **330**, 1371–1374 (2010)

3. M. Vasilakaki, K.N. Trohidou, J. Nogués, *Sci. Rep.* **5,** 9609 (2015).

4. S. Mu, A. L. Wysocki, K. D. Belashchenko, *Phys. Rev. B* **87**, 054435 (2013)

5. F. Farzaneh, *J. Sci. Islam. Repub. Iran* **22**, 329–333 (2011).

6. C.A. Schneider, Rasband, W.S., Eliceiri, K.W. *Nature Methods* **9**, 671-675 (2012).

7. R.W. Cheary, A. Coelho, *J. Appl. Crystallogr.* **25**, 109–121 (1992).

8. S. Dey, M.D. Hossain, R.A. Mayanovic, R. Wirth, R.A. Gordon (submitted).

9. M.D. Hossain, S. Dey, R. A. Mayanovic, R. Sakidja, M. Benamara (in preparation).

CONCLUSION

In conclusion I have successfully synthesized the novel core shell NPs. In chapter one I presents my analysis results for α-Cr_2O_3/α-$Co_{0.43}Cr_{1.57}O_{2.9}$ core shell NPs. Chapter two shows my experimental and theoretical results for α-Cr_2O_3@α-$Ni_{0.58}Cr_{1.42}O_{2.88}$ core shell NPs. Chapter three is an overview of all the NPs system of α-Cr_2O_3/α-$M_xCr_{2-x}O_y$ (M=Ni,Co,Mn,Fe). TEM result give us the information about particle size and shape. Almost all the particles shows spherical morphology with certain degree of faceting. HRTEM results provide the evidence of the core shell structure formation with an existence of sharp interface, the shell region of the nanoparticles maintains the epitaxial atomic registry of the core which results highly ordered shell in the NPs and this shell structure maintains the original corundum structure of the core. Combined results from HRTEM and TEM-EDX shows that the presence of transition metal elements (Ni, Co, Fe, Mn) in higher concentration in the shell region. My XRD data analysis shows that the all the sample are pure and except Ni sample I did not observe any other oxide phase formation. Also XRD provides evidence of the corundum structure maintains both in the core and shell of the NPs. My XPS results shows that the incorporated transition metal elements are in +2 oxidation state where as the Cr is in +3 oxidation state. This results explain that there are vacant sites formation (anion or cation vacncy) in the shell of the NPs. Magnetic measurements shows the FM characteristics of the NPs with substantial exchange biasing effect between the AFM core and FM/FiM shell. My first principle calculation shows that the Ni substitution in the α-Cr_2O_3 results localized FM characteristics of the materials.

REFERENCES

(1) DiVincenzo, D. P.; Loss, D. Quantum Computers and Quantum Coherence. *J. Magn. Magn. Mater.* **1999**, *200* (1–3), 202–218.

(2) Tartaj, P.; Morales, M. P.; González-Carreño, T.; Veintemillas-Verdaguer, S.; Serna, C. J. Advances in Magnetic Nanoparticles for Biotechnology Applications. *J. Magn. Magn. Mater.* **2005**, *290–291, Part 1*, 28–34.

(3) Pankhurst, Q. A.; Connolly, J.; Jones, S. K.; Dobson, J. Applications of Magnetic Nanoparticles in Biomedicine. *J. Phys. Appl. Phys.* **2003**, *36* (13), R167.

(4) Meiklejohn, W. H.; Bean, C. P. New Magnetic Anisotropy. *Phys. Rev.* **1956**, *102* (5), 1413–1414.

(5) Meiklejohn, W. H.; Bean, C. P. New Magnetic Anisotropy. *Phys. Rev.* **1957**, *105* (3), 904–913.

(6) Nogués, J.; Sort, J.; Langlais, V.; Skumryev, V.; Suriñach, S.; Muñoz, J. S.; Baró, M. D. Exchange Bias in Nanostructures. *Phys. Rep.* **2005**, *422* (3), 65–117.

(7) Gangopadhyay, S.; Hadjipanayis, G. C.; Sorensen, C. M.; Klabunde, K. J. Exchange Anisotropy in Oxide Passivated Co Fine Particles. *J. Appl. Phys.* **1993**, *73* (10), 6964–6966.

(8) Gangopadhyay, S.; Hadjipanayis, G. C.; Sorensen, C. M.; Klabunde, K. J. Effect of Exchange Anisotropy on the Hysteresis Behavior of Co Particles. *Nanostructured Mater.* **1992**, *1* (6), 449–456.

(9) Del Bianco, L.; Fiorani, D.; Testa, A. M.; Bonetti, E.; Savini, L.; Signoretti, S. Magnetic Properties of the Fe/Fe Oxide Granular System. *J. Magn. Magn. Mater.* **2003**, *262* (1), 128–131.

(10) Del Bianco, L.; Fiorani, D.; Testa, A. M.; Bonetti, E.; Savini, L.; Signoretti, S. Magnetothermal Behavior of a Nanoscale Fe/Fe Oxide Granular System. *Phys. Rev. B* **2002**, *66* (17), 174418.

(11) Martín, J. I.; Nogués, J.; Liu, K.; Vicent, J. L.; Schuller, I. K. Ordered Magnetic Nanostructures: Fabrication and Properties. *J. Magn. Magn. Mater.* **2003**, *256* (1–3), 449–501.

(12) Himpsel, F. J.; Ortega, J. E.; Mankey, G. J.; Willis, R. F. Magnetic Nanostructures. *Adv. Phys.* **1998**, *47* (4), 511–597.

(13) Khurshid, H.; Chandra, S.; Li, W.; Phan, M. H.; Hadjipanayis, G. C.; Mukherjee, P.; Srikanth, H. Synthesis and Magnetic Properties of Core/shell FeO/Fe3O4 Nano-Octopods. *J. Appl. Phys.* **2013**, *113* (17), 17B508.

(14) Sun, X.; Frey Huls, N.; Sigdel, A.; Sun, S. Tuning Exchange Bias in Core/Shell FeO/Fe3O4 Nanoparticles. *Nano Lett.* **2012**, *12* (1), 246–251.

(15) Wu, C.; Zhang, H.; Wu, Y.-X.; Zhuang, Q.-C.; Tian, L.-L.; Zhang, X.-X. Synthesis and Characterization of Fe@Fe2O3 Core-Shell Nanoparticles/graphene Anode Material for Lithium-Ion Batteries. *Electrochimica Acta* **2014**, *134*, 18–27.

(16) D'Addato, S.; Spadaro, M. C.; Luches, P.; Grillo, V.; Frabboni, S.; Valeri, S.; Ferretti, A. M.; Capetti, E.; Ponti, A. Controlled Growth of Ni/NiO Core–shell Nanoparticles: Structure, Morphology and Tuning of Magnetic Properties. *Appl. Surf. Sci.* **2014**, *306*, 2–6.

(17) Lee, I. S.; Lee, N.; Park, J.; Kim, B. H.; Yi, Y.-W.; Kim, T.; Kim, T. K.; Lee, I. H.; Paik, S. R.; Hyeon, T. Ni/NiO Core/Shell Nanoparticles for Selective Binding and Magnetic Separation of Histidine-Tagged Proteins. *J. Am. Chem. Soc.* **2006**, *128* (33), 10658–10659.

(18) Yu, M. H.; Devi, P. S.; Lewis, L. H.; Oouma, P.; Parise, J. B.; Gambino, R. J. Towards a Magnetic Core–shell Nanostructure: A Novel Composite Made by a Citrate–nitrate Auto-Ignition Process. *Mater. Sci. Eng. B* **2003**, *103* (3), 262–270.

(19) Sol-gel synthesis and photoluminescence of p-type semiconductor Cr2O3 nanowires http://scitation.aip.org/content/aip/journal/apl/88/24/10.1063/1.2213204 (accessed Apr 10, 2016).

(20) Cao, H.; Qiu, X.; Liang, Y.; Zhao, M.; Zhu, Q. Sol-Gel Synthesis and Photoluminescence of P-Type Semiconductor Cr2O3 Nanowires. *Appl. Phys. Lett.* **2006**, *88* (24), 241112.

(21) Abdullah, M. M.; Rajab, F. M.; Al-Abbas, S. M. Structural and Optical Characterization of Cr2O3 Nanostructures: Evaluation of Its Dielectric Properties. *AIP Adv.* **2014**, *4* (2), 27121.

(22) M Julkarnain, J. H. Optical Properties of Thermally Evaporated Cr2O3 Thin Films. *Can. J. Chem. Eng. Amp Technol.* **2012**, *3* (4), 81–85.

(23) Oxidative dehydrogenation of propane over Cr2O3/Al2O3 and Cr2O3 catalysts: effects of loading, precursor and surface area http://www.sciencedirect.com/science/article/pii/S0926860X02001321 (accessed Jan 3, 2016).

(24) Fleischer, K.; Caffrey, D.; Farrell, L.; Norton, E.; Mullarkey, D.; Arca, E.; Shvets, I. V. Raman Spectra of P-Type Transparent Semiconducting Cr2O3:Mg. *Thin Solid Films* **2015**, *594, Part B*, 245–249.

(25) Jin, H.; Huang, Y.; Jian, J. Plate-like Cr2O3 for Highly Selective Sensing of Nitric Oxide. *Sens. Actuators B Chem.* **2015**, *206*, 107–110.

(26) Lin, J.; Sproul, W. D. Structure and Properties of Cr2O3 Coatings Deposited Using DCMS, PDCMS, and DOMS. *Surf. Coat. Technol.* **2015**, *276*, 70–76.

(27) Shi, C.-M.; Wang, T.-G.; Pei, Z.-L.; Gong, J.; Sun, C. Microstructure, Interface, and Properties of Multilayered CrN/Cr2O3 Coatings Prepared by Arc Ion Plating. *J. Mater. Sci. Technol.* **2014**, *30* (12), 1193–1201.

(28) Subramanyam, K.; Sreelekha, N.; Murali, G.; Reddy, D. A.; Vijayalakshmi, R. P. Structural, Optical and Magnetic Properties of Cr Doped SnO2 Nanoparticles Stabilized with Polyethylene Glycol. *Phys. B Condens. Matter* **2014**, *454*, 86–92.

(29) Mustafa, L.; Anjum, S.; Waseem, S.; Khurshid, H.; Choudhary, R.; Bashir, F. Effect of Co and Cd Doping on Structural, Magnetic, Electrical and Optical Properties of ZnO Based Dilute Magnetic Oxide Semiconductor. *Mater. Today Proc.* **2015**, *2* (10, Part B), 5256–5261.

(30) Poornaprakash, B.; Ramu, S.; Park, S.-H.; Vijayalakshmi, R. P.; Reddy, B. K. Room Temperature Ferromagnetism in Nd Doped ZnS Diluted Magnetic Semiconductor Nanoparticles. *Mater. Lett.* **2016**, *164*, 104–107.

(31) Li, C.; Zhao, Y. F.; Gong, Y. Y.; Wang, T.; Sun, C. Q. Band Gap Engineering of Early Transition-Metal-Doped Anatase TiO2: First Principles Calculations. *Phys. Chem. Chem. Phys.* **2014**, *16* (39), 21446–21451.

(32) Chuang, C.-C.; Lin, C.-K.; Wang, T. T.; Srinivasadesikan, V.; Raghunath, P.; Lin, M. C. Computational and Experimental Studies on the Effect of Hydrogenation of Ni-Doped TiO2 Anatase Nanoparticles for the Application of Water Splitting. *RSC Adv.* **2015**, *5* (99), 81371–81377.

(33) Wang, Y.; Zhang, R.; Li, J.; Li, L.; Lin, S. First-Principles Study on Transition Metal-Doped Anatase TiO2. *Nanoscale Res. Lett.* **2014**, *9* (1), 1–8.

(34) Frank Maldonado, R. R. Structure, Electronic and Magnetic Properties of Ca-Doped Chromium Oxide Studied by the DFT Method. *Phys. B Condens. Matter* **2012**, *407* (8), 1262–1267.

(35) Navas, J.; Sánchez-Coronilla, A.; Aguilar, T.; Hernández, N. C.; de los Santos, D. M.; Sánchez-Márquez, J.; Zorrilla, D.; Fernández-Lorenzo, C.; Alcántara, R.; Martín-Calleja, J. Experimental and Theoretical Study of the Electronic Properties

of Cu-Doped Anatase TiO2. *Phys. Chem. Chem. Phys. PCCP* **2014**, *16* (8), 3835–3845.

(36) Sun Young Yun, G.-B. C. First-Principles Calculations on Magnetism of Transition Metal Doped Zinc Oxide. *J. Magn. Magn. Mater.* **2004**, *272*, 1563-E1564.

(37) Pan, J.; Waghmare, U. V.; Kumar, N.; Ehi-Eromosele, C. O.; Rao, C. N. R. Effect of Nitrogen and Fluorine Co-Substitution on the Structure and Magnetic Properties of Cr2O3. *ChemPhysChem* **2015**, *16* (7), 1502–1508.